

國立交通大學

電控工程研究所

碩士論文

SOI 基板上利用簡單下壓方式組裝之微光學讀取頭

**A MEMS-Based Optical Pickup Unit Assembled by
Simple Push Operation on SOI Wafers**

研究生：林健安

指導教授：邱一 博士

中華民國九十九年七月

SOI 基板上利用簡單下壓方式組裝之微光學讀取頭

**A MEMS-Based Optical Pickup Unit Assembled by
Simple Push Operation on SOI Wafers**

研 究 生:林健安

Student: Chen An Lin

指 導 教 授:邱一

Advisor: Yi Chiu

國立交通大學 電機學院

電控工程研究所

碩士論文

A Thesis

Submitted to Department of Electrical Control Engineering

College of Electrical Engineering

National Chiao Tung University

In Partial Fulfillment of the Requirement

For the Degree of

Master

In

Electrical and Control Engineering

July 2010

Hsinchu, Taiwan, R.O.C.

中華民國九十九年七月

中文摘要

近年來在半導體產業的發展之下，微機電製程技術有許多重大的發展。對於光學資料儲存系統而言，微光機電技術(Micro Optical Electro Mechanical System)正是提供製造更小更輕的光學資料儲存系統的一個好方法。

我們的目標是要製作一微光學資訊平台，此微光學平台是以數個三維斜面結構以及其他組裝於此平台上的光學元件所組成，因此採用應力幾乎為零且結構較厚的 SOI (Silicon On Insulator)基板製作微鏡面，避免一般利用多晶矽製作時可能發生的翹曲現象。

本實驗室之前已提出利用下壓動作即可成功組裝 45° 微鏡面的設計，本論文將利用此下壓組裝方法，組裝 4 種不同角度的斜面鏡以證實此方法可用於任意角度的斜面鏡組裝，符合未來在光學平台應用中不同角度三維微結構的需求。本論文亦對於原始 45° 結構的誤差問題加以探討並提出改善方式，使得角度從 $45.9 \pm 0.2^\circ$ 改善為 $45.4 \pm 0.2^\circ$ 。最後，本論文並且提出且成功製造出 135° 三維微結構，平均角度為 $135.6 \pm 0.2^\circ$ ，可應用在本論文中提出的光學讀取頭架構。此光學讀取頭的模擬結果以及設計原理在論文中詳細的說明，是利用全像光學元件(HOE)來達到像散以及分光的功用，取代傳統光學讀取頭中利用體積較大的柱面鏡以及分光鏡，進而達到微型化的目的。此全像光學元件(HOE)以微機電製程的方法製造於光學平台的斜面結構上，它的表面輪廓以及光學特性在論文中都已經過實驗量測並驗證。完整的光學平台架構正處於製程的最後階段。

Abstract

Recently, the Micro Electro Mechanical Systems (MEMS) technology has many important developments with the rapid progress in the semiconductor industry. The requirement of miniaturization and lightness pushes the development of smaller and lighter optical data storage systems. Micro optical pickup head fabricated by Micro-Opto-Electro-Mechanical System (MOEMS) technology is one of the methods to realize portable high-capacity optical storage systems.

In this thesis, micro optical pickup head on an micro optical bench is composed of nonvertical micro mirrors and other optical components bonded on the optical bench. Silicon on insulator (SOI) wafers with almost zero stress are used to avoid stress-induced curvature for optical applications.

In our previous study, 45° structures were assembled using a novel simple push operation. Micromirrors with four different angles were pushed up by probes to demonstrate the assembly method for arbitrary angles in this thesis. The angular deviation of the 45° structures was studied with different width of the support arms. The angles of 45° structures were improved from $45.9^\circ \pm 0.2^\circ$ to $45.4^\circ \pm 0.2^\circ$. The design and assembly of 135° mirrors were verified and used in the proposed optical pickup head of this thesis. The devices were fabricated with an average angle of $135.6^\circ \pm 0.2^\circ$. The simulation results and the design principle of the MEMS-based optical pickup head are present. A holographic optical element is used in the optical bench and fabricated on the nonvertical mirror. The surface profile and optical properties of the fabricated holographic were measured. The fabrication of the optical bench is in progress.

致謝

結束了碩士班的研究生活，懷著感激的心謝謝所有幫助過我的人，我要感謝我的父母，讓我能無憂無慮的完成碩士學業。再來要感謝的是我的指導教授邱一老師，在實驗上給予我許多專業的建議及指導，也教導了我發現問題及解決問題的方法，學習到了許多研究與處事應有的態度，使得我的實驗能夠順利進行。

非常感謝我的口試委員方維倫老師和施錫富老師，能再繁忙之餘對我的論文提供指導建議和鼓勵。

還有感謝實驗室學長昌修、弘諳、子麟、昇儒對我的指導，讓我能傳承你們的經驗前進，以及電控所的學長振鈞、冠州和動機所的學長信瑜，感謝你們總是在繁忙中還能夠給予我許多實驗上的建議。感謝奈米中心徐小姐、范小姐、國華、范先生的幫忙，讓我能迅速完成許多的製程實驗。

要感謝的當然還少不了實驗室的夥伴，感謝經富、哲明、俊宏、鴻智、姿穎、政安、彥傑、彥霆陪我度過在實驗室的日子，你們總是能互相打氣維持實驗室的良好氣氛讓我把做實驗所帶來的煩悶一掃而空。

最後我要再次感謝我的老爸老媽以及我的家人朋友們，感謝你們的支持和鼓勵，不論是學術或是待人處世都讓我在碩士班的生涯學到了很多。最後也謝謝這段時間培育我成長的交通大學，珍重再見。

Table of Content

中文摘要	iv
Abstract	ii
誌謝	iii
Table of Content	iv
List of Figures	vi
List of Tables	xii
Chapter 1 Introduction	1
1-1 Motivation	1
1-1-1 Waveguide type	3
1-1-2 Planar type	4
1-1-3 Free-space staked type	4
1-1-4 Optical pickup for small form factor drives	5
1-2 Review of Micro Assembly	7
1-2-1 Microfabricated hinges	7
1-2-2 Three dimensional MEMS by active assembly	8
1-2-3 Three dimensional MEMS by self-assembly	11
1-2-4 Manual or robot-assisted assembly	17
1-3 Objective and organization of the thesis	24
Chapter 2 Principle and Design	26
2-1 Introduction	26
2-2 Mirror with arbitrary angles	26
2-2-1 30°, 45°, and 60° mirrors	26
2-2-2 135° mirrors	32
2-3 Optical bench and MEMS-based optical pickup head	34
2-3-1 Simulation of the MEMS-based optical pickup head	35
2-3-2 Diffractive efficiency of HOE	39
2-3-3 Layout design	45
2-3-4 Summary	48
Chapter 3 Fabrication Process	49
3-1 Fabrication process	49
3-2 Fabrication issues and solutions	61
3-2-1 Photolithography of Si ₃ N ₄	61

3-2-2	Backside ICP etching	62
3-3	Summary	67
Chapter 4	Measurement and Results	68
4-1	30°, 45°, and 60° structures	68
4-2	135° structures	77
4-3	Holographic optical element (HOE)	81
4-3-1	Surface profile.....	81
4-3-2	Optical measurement	83
4-3-3	Discussion	85
4-4	Summary	87
Chapter 5	Conclusion and Future work	88
5-1	Conclusion	88
5-2	Future work.....	88
5-2-1	Nonvertical devices.....	88
5-2-2	Optical bench	89
Reference	94



List of Figures

Figure 1-1 Conventional optical pickup head.....	2
Figure 1-2 On-chip optical pickup head system [1].....	2
Figure 1-3 Waveguide type optical pickup head, (a) fabrication process, (b) schematic [2].....	3
Figure 1-4 Planer type optical pickup head, (a) side view, (b) top view [3].....	4
Figure 1-5(a) Schematic of stacked optical pickup head, (b) cross section of the silicon-base suspended optical element [4].....	5
Figure 1-6(a) Schematic of integrated optical pickup, (b) picture of silicon bench [5].	6
Figure 1-7 Optical path of integrated optical pickup [5]	6
Figure 1-8(a) Fabrication process of micro hinges, (b) SEM micrograph of a hinged structure [7].....	8
Figure 1-9(a) Crossed sectional view of SDA, (b) working principle of SDA [8].....	9
Figure 1-10 SEM of a free-rotating hinged micromirror lifted by an array of SDA [9]..	9
Figure 1-11(a) SEM of the automated assembly system connected to a scanning mirror, (b) basic assembly process [10].....	10
Figure 1-12(a) Schematic of the lateral thermal actuator, (b) SEM of the vertical thermal actuator [10].....	11
Figure 1-13 SEM of (a) the self-engaging locking mechanism, (b) an assembled corner cube reflector [10].....	11
Figure 1-14 Magnetic force assembly.....	12
Figure 1-15(a) Side view of a hinged microstructure in an external magnetic field, (b) hinge with different dimensions and sensitivity factors [12].....	13
Figure 1-16 Step-by-step photographs of the four-step sequential assembly [12]	13
Figure 1-17 Schematic of the concept for centrifugal force assembly	14

Figure 1-18 Batch assembly by centrifugal force: (a) an array of bridge structures, (b) an array of micromirrors [13]	14
Figure 1-19 Schematic of thermokinetic force assembly	15
Figure 1-20 Assembly by thermokinetic force: (a) an array of micromirrors, (b) corner cube reflectors [14]	16
Figure 1-21(a) Assembled structures by combining bimorph beams with locking mechanism, (b) locking mechanism [15].....	16
Figure 1-22 Surface tension powered assembly by (a) photoresist [16], (b) solder [17].	17
Figure 1-23(a) MEMS electrothermal gripper, (b) MEMS end-effector [19]	18
Figure 1-24(a) Overview of whole chip where assembly is taking place, (b) close up of the de-tether process, (c) a micropart is picked off the substrate, (d) schematic of microconnector, (e) the connector being inserted into the socket [19].....	19
Figure 1-25(a) SEM image, (b) optical micrograph of assembled device [19]	20
Figure 1-26 Hingeless device concept [20]	21
Figure 1-27 Schematic assembly sequence [20].....	21
Figure 1-28(a) Optical micrographs of the assembly process (b) SEM image of 90° out-of-plane structures [20].....	21
Figure 1-29 Assembly process with one-push operation [21]	23
Figure 1-30(a) Schematic view of the V-shaped hinge after assembly, (b) top view..	23
Figure 1-31 SEM images and optical micrograph of assembled devices, (a) Mirror is flipped by one-push operation, (b) a corner cube reflector. [21].....	23
Figure 1-32 Schematic of the MEMS-based optical pickup head in this thesis	25
Figure 2-1(a) Layout design of the 45° device, (b) 3-D model.....	27

Figure 2-2 Assembly process of the 45° device	28
Figure 2-3 Layout design of (a) 60° device, (b) 30° device	28
Figure 2-4 Form and dimensions of cross sections.....	29
Figure 2-5 Schematic of static equilibrium after assembly	31
Figure 2-6 Schematic of assembled 45° mirror with bent support	31
Figure 2-7(a) Layout design of 135° device, (b) 3-D model.....	32
Figure 2-8 Assembly process of the 135° device	33
Figure 2-9 Schematic of the MEMS-based optical pickup head	34
Figure 2-10 Zemax simulation of the MEMS-based optical pickup head.....	35
Figure 2-11 Zemax simulated optical spot on the disk	35
Figure 2-12 Simulated optical spot on the photodetector with various amount of defocus	37
Figure 2-13 Schematic of the astigmatic method	39
Figure 2-14 Simulation of the S-curve.....	39
Figure 2-15 Schematic of diffraction theory.....	41
Figure 2-16 (a) Schematic and (b) phase distribution of the reflective linear phase grating	42
Figure 2-17 Schematic of the reflective type linear phase grating on 135° mirror...	43
Figure 2-18 Calculation of diffraction efficiency	44
Figure 2-19 Layout of the holographic optical element.....	46
Figure 2-20 Schematic of the optical bench after assembly	46
Figure 2-21 Optical simulation of the system, (a) side-view, (b) top-view	47
Figure 2-22 Layout of optical bench.....	48
Figure 3-1 Fabrication process.....	50
Figure 3-2 Schematic of the vapor HF release setup [28]	60

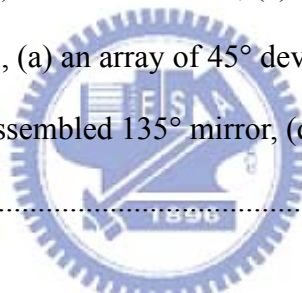
Figure 3-3 Problems in Si ₃ N ₄ photolithography	61
Figure 3-4 After the silicon nitride RIE, (a) silicon nitride remained on the release holes, (b) silicon nitride was etched completely	62
Figure 3-5(a) Bending of the mirror plate, (b) break of the mirror plate after the backside ICP etching.....	63
Figure 3-6 Bending measurement by WYKO before release process.	63
Figure 3-7 Bending measurement by WYKO after release process	64
Figure 3-8 Broken silicon oxide at the big through-wafer hole.....	65
Figure 3-9 Device layer is etched in the backside ICP process	65
Figure 3-10 Schematic of original and redesigned backside etching under the mirror plate, (a) big hole, (b) meshed structure, (c) entire substrate is unetched....	66
Figure 3-11 Fabricated devices, (a) an array of 45° device, (b) an array of 135° device, (c) side view of an assembled 135° mirror, (d) holographic optical element (HOE).....	67
	
Figure 4-1 Assembly process of a 45° mirror without hinges, (a) two probes were aligned with the push pads before assembly, (b) the support was pushed by Probe 1, (c) the mirror was pushed by Probe 2, (d) remove Probe 1 so that the support lie on the mirror, (e) Probe 2 was removed, (f) Probe 1 was removed.....	69
Figure 4-2 An assembled 30° device, (a) top view, (b) side view, (c) interlock, (d) torsional beam connected to the mirror plate.....	70
Figure 4-3 An assembled 45° device, (a) top view, (b) side view	70
Figure 4-4 An assembled 60° device, (a) top view, (b) side view, (c) interlock, (d) torsional beam of the mirror plate with mechanical stop.....	71

Figure 4-5 An assembled mirror at 30.6°	72
Figure 4-6 An assembled mirror at 45.4°	73
Figure 4-7 An assembled mirror at 60.7°	73
Figure 4-8 Bent supports, (a) side view, (b) perspective view [22].....	75
Figure 4-9 Bending of supports in prior design after assembly, (a) 3-D profile, (b) 2-D analysis.....	75
Figure 4-10 Bending of improved supports in this work after assembly, (a) 3-D profile, (b) 2-D analysis.....	76
Figure 4-11 Assembly process of a 135° mirror without hinge, (a) two probes aligned before assembly, (b) mirror plate pushed by Probe 1 and held by Probe 2 from the other side	77
Figure 4-12 An assembled 135° device, (a) top view, (b) side view, (c) push pad of mirror plate, (d) interlock, (e) torsional beams of mirror plate, (f) torsional beams and mechanical stops	79
Figure 4-13 An assembled mirror at 135.4°	80
Figure 4-14 Optical micrographs of the fabricated HOE	82
Figure 4-15 SEM micrographs of the HOE, (a) fabricated HOE, (b) period of HOE, (c) linewidth of the etching area, (d) linewidth of the unetching area	82
Figure 4-16 AFM measurement results.....	83
Figure 4-17 Illustration of the optical measurement.....	84
Figure 4-18(a) Experimental setup, (b) highlight of the HOE.....	84
Figure 4-19 Diffraction optical spot projected on the screen	85
Figure 4-20 Comparison of diffraction efficiency between the measurement and theoretical curve.....	86
Figure 4-21 Fabricated optical bench	87
Figure 5-1 Assembly process of optical pickup unit.....	89

Figure 5-2 Fabricated (a) PCB, (b) holder.91

Figure 5-3 (a) Schematic of assembled optical pickup unit, (b) test experiment
 showing PCB, holder and objective lens91

Figure 5-4 Bonding process of laser diode, (a) a release sample and a mirror plate
 before assembly, (b) overlaid image of the laser diode, (c) apply thermal
 cure adhesive on the laser diode position, (d) bond the laser diode by
 controlling the arm of flip-chip bonder.92



List of Tables

Table 2-1 Calculation of angular deviation.....	31
Table 3-1 Comparison of bending mirror plate.....	64
Table 4-1 Angle measurement of the 30° device (resolution: 0.2°).....	72
Table 4-2 Angle measurement of the 45° device (resolution: 0.2°).....	723
Table 4-3 Angle measurement of the 60° device (resolution: 0.2°).....	74
Table 4-4 Comparison of bending support with different design, (a) <i>x</i> -axis, (b) <i>y</i> -axis.	76
Table 4-5 Angle measurement of the 135° device (resolution: 0.2°).....	80
Table 4-6 Comparison of design values and AFM measurement results of the HOE .	83
Table 4-7 Measurement results of diffraction optical intensity and etching depth.....	85



Chapter 1 Introduction

1-1 Motivation

The progress of information technology has increased the demand for data storage day by day. Portable digital devices such as cellular phones, MP3 players and personal digital assistants (PDA) have also found a rapidly increasing market in recent years. Increasing the data storage density and reducing the device size is important for these mobile storage devices. In addition, it is also very crucial to obtain fast access speed of information. Optical data storage systems can achieve these requests.

Optical pickup heads are the most important part in the optical data storage systems. Conventional optical pickup heads are usually composed of laser diodes, grating plates, beam splitters, collimators, reflective mirrors and objective lenses, as shown in Figure 1-1. A beam of light emitted from the laser diode passes through a diffraction grating and diffracted beams are produced. The zeroth-order beam and first-order beams can be used to read data and track the spot respectively. Then, the light passes through the beam splitter and is converted into a parallel beam by the collimator lens. The beam becomes circularly polarized after passes through the quarter wave plate. The beam is then focused on the surface of the disc by the objective lens. The reflected beam becomes linear polarized in the orthogonal direction with respect to the incident beam and is reflected into the photodetector by the polarizing beam splitter. Finally, the photocurrent can be measured by the current detection circuits.

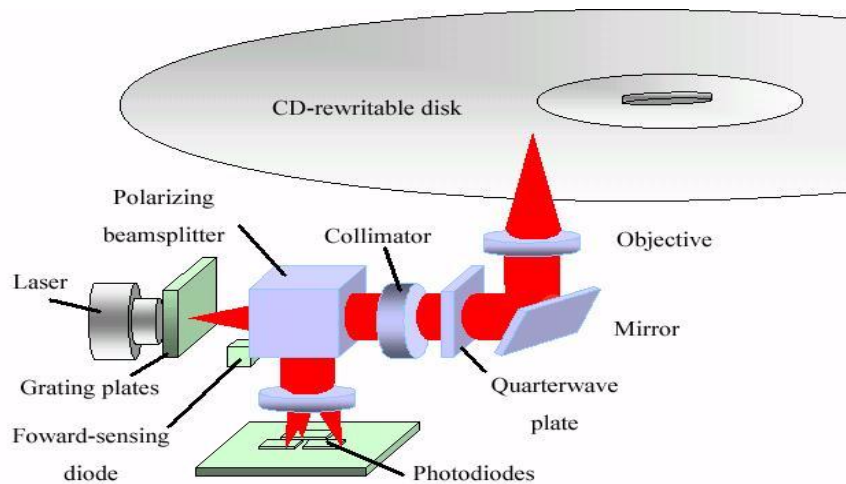


Figure 1-1 Conventional optical pickup head.

In the past years, miniature optical pickup heads have been fabricated by Micro Electro-Mechanical Systems (MEMS) technology. The free-space micro-optical bench is an example of this technology, as shown in Figure 1-2 [1]. The pickup head is composed of a semiconductor laser, a collimator lens, two focusing lens, a beam splitter and two 45° reflectors. The optical bench is fabricated with two polysilicon structure layers and micromachined hinge technology. Compared with the conventional bulk optical pickup heads, the miniaturized optical bench has the advantaged such as reduced size, weight, cost and enhancement of flexibility.

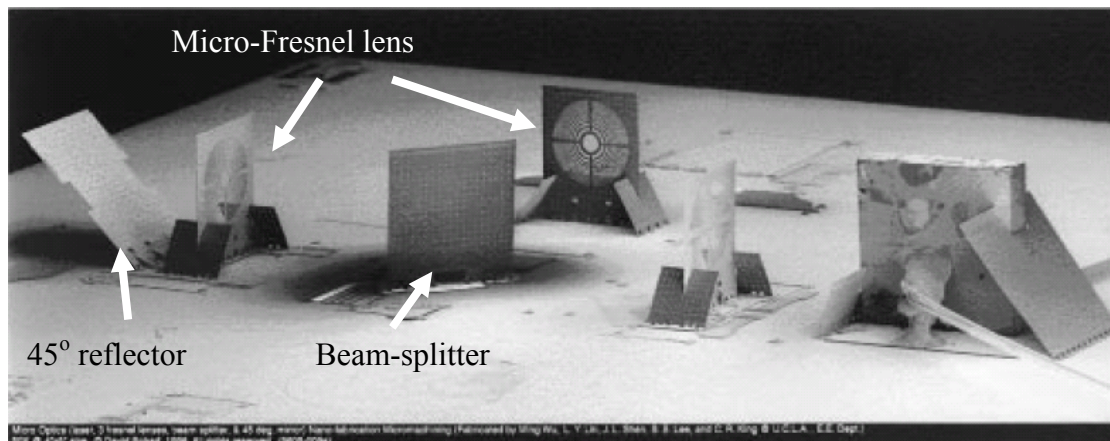


Figure 1-2 On-chip optical pickup head system [1].

In addition to the free-space optical pickup head system, there are other types of miniature optical pickup head such as the waveguide type, planar type and free-space stacked type. These miniature optical systems are reviewed in the following sections.

1-1-1 Waveguide type

The waveguide-type optical pickup head is a two dimensional device where light propagates in the planar waveguides in a substrate. All the components can be defined by photolithography simultaneously, as shown in Figure 1-3. Figure 1-3 (a) shows the fabrication process of the waveguide device. Figure 1-3 (b) shows the schematic of a waveguide optical pickup head [2]. The waveguide is formed with a silicon nitride guiding layer and a silicon oxide buffer layer on a silicon substrate. The guided wave diverging from the laser diode (LD) is focused by the focusing grating coupler into a point on the disk. Then the twin grating focusing beam splitter divides the reflected wavefront into halves, deflects, and focuses into photodiodes. The current signals from the photodiode can be used for readout, focus and tracking signals.

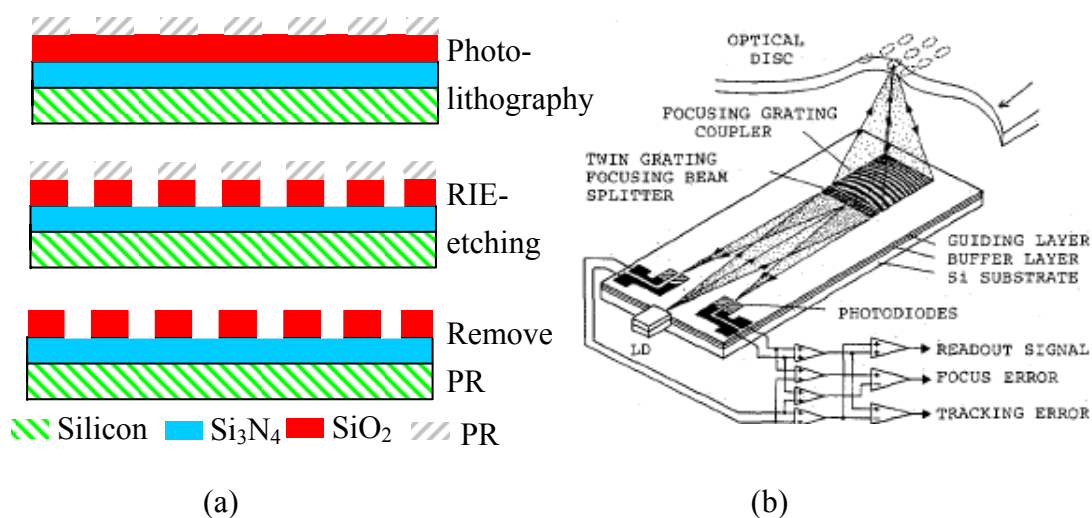


Figure 1-3 Waveguide type optical pickup head, (a) fabrication process, (b) schematic [2].

1-1-2 Planar type

The construction of the planer optical pickup head is shown in Figure 1-4 [3]. The system is composed of four diffractive optical elements integrated on the glass substrate. The light propagates in the glass substrate and then is focused on the disk. The top and bottom of the glass substrate is coated with metal as the reflective surface. The laser diode and the photodetector are mounted on the bottom surface of the substrate. First, a laser beam emitted from the laser diode is couple into the substrate and follows a zigzag optical path. The zeroth-order beam in the forward optical path is focused on the disk by the transmission off-axis objective lens. On the returning path, the first-order diffracted beam is generated by the reflection-focusing beam splitter and projected onto the photodetector. Then the focusing error signal and tracking error signal can be obtained from the photodetector.

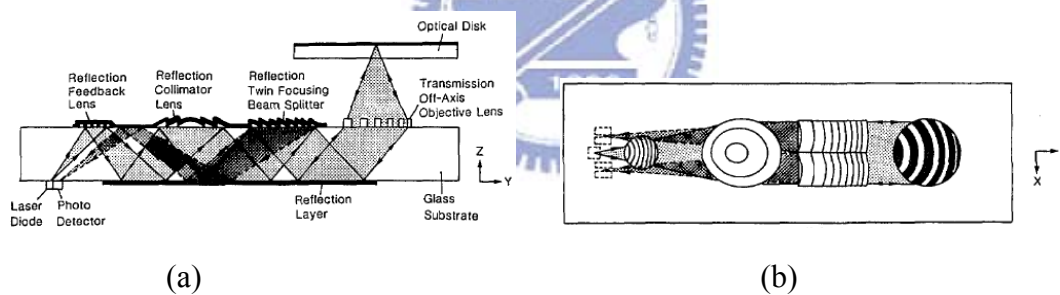


Figure 1-4 Planer type optical pickup head, (a) side view, (b) top view [3].

1-1-3 Free-space stacked type

The free-space stacked optical pickup head is shown in Figure 1-5 [4]. The system is composed of a semiconductor edge-emitting laser source, a 45° bulk silicon reflector, a grating, an holographic optical element (HOE) and aspherical Fresnel lenses. A laser beam is emitted from the laser diode and reflected by the 45° silicon bulk-micronachining mirror. Then the laser is split into three separate beams after

pass through the grating, the two first-order diffracted beams are used for tracking servo control. After being collimated by a Fresnel lens, the beams are eventually focused on the disk by another set of Fresnel lenses. The three beams reflected back from the disk are deflected by the HOE and projected on the photodetector. The 45° bulk silicon reflector is formed from a $\langle 100 \rangle$ silicon wafer by anisotropic etching with KOH/IPA etchant. The other optical components such as gratings, HOEs, and Fresnel lenses are formed in silicon nitride film suspended on a silicon substrate and then stacked by chip bonding, as shown in Figure 1-5 (b).

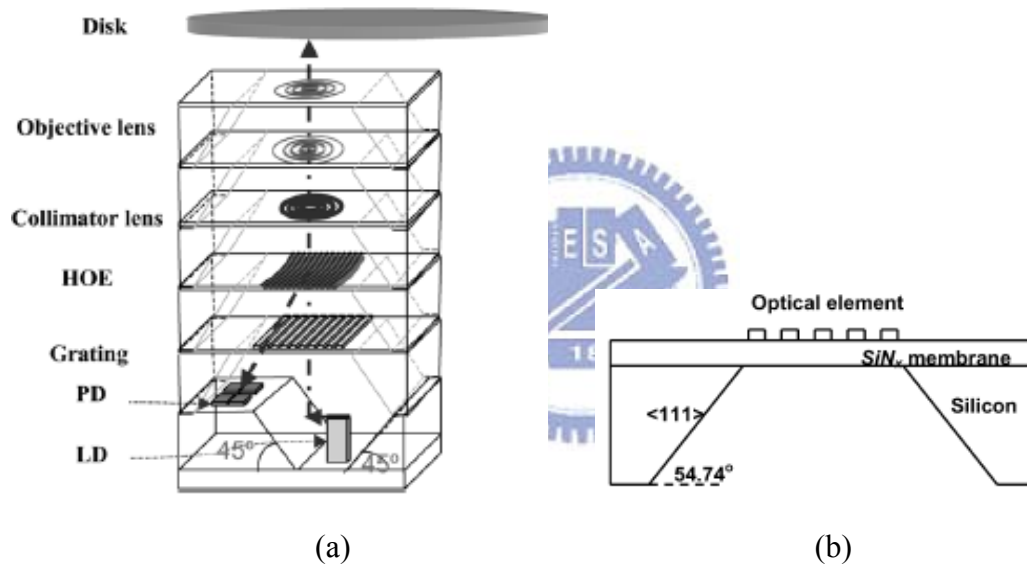
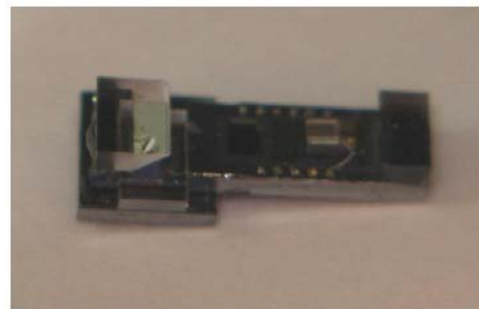
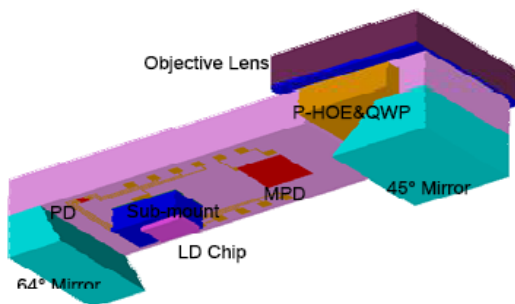


Figure 1-5 (a) Schematic of stacked optical pickup head, (b) cross section of the silicon-base suspended optical element [4].

1-1-4 Optical pickup for small form factor drives

Samsung and Yon sei university proposed an optical pickup for small form factor drives [5]. The optical pickup is composed of a blue laser diode, a photodetector, and a silicon optical bench. Figure 1-6 (a) and Figure 1-6 (b) show the schematic and photograph of the optical pickup. Figure 1-7 shows the optical path of this optical pickup. After the light emitted from the laser diode is reflected by a 45° mirror, it

passes through a polarized holographic optical element with a quarter wave plate and is focused onto the disc. The light returned from the disc is sent to the photodetector by the polarized holographic optical element and the 64° mirror. Focus and tracking error signals are obtained by astigmatic and push-pull methods. The dimensions of the complete optical pickup are height = 1.9 mm, width = 2.2 mm, and length = 6.6 mm.



(a)

(b)

Figure 1-6 (a) Schematic of integrated optical pickup, (b) picture of silicon bench [5].

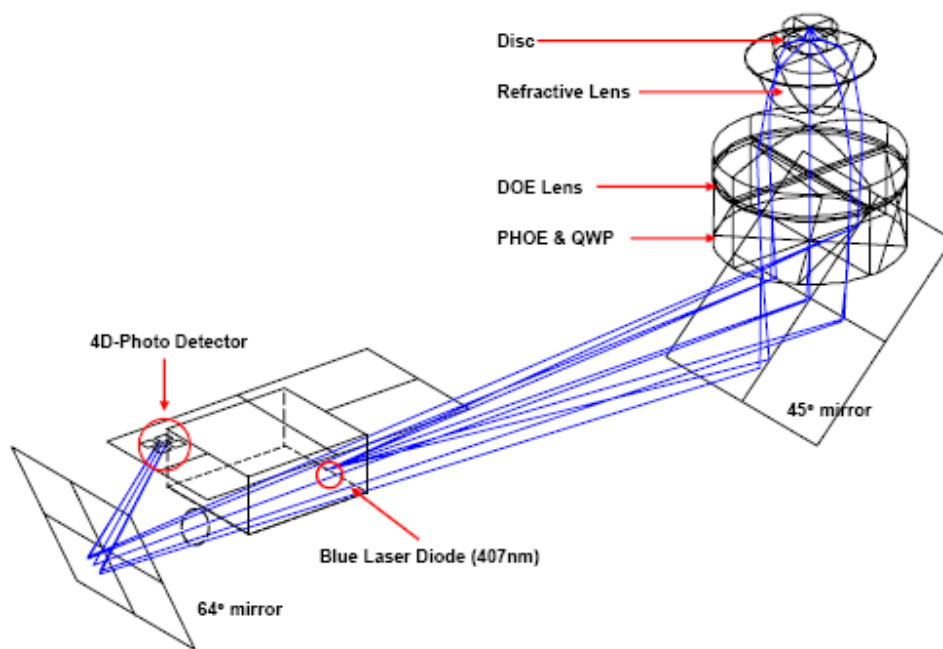


Figure 1-7 Optical path of integrated optical pickup [5].

1-2 Review of Micro Assembly

Ever since the microfabricated hinge made the out-of-plane structures possible, many researchers have been working on 3-D assembly techniques. In addition to manual assembly, “active-assembly” and “self-assembly” are two main techniques. The active assembly method uses actuators such as scratch drive actuators or thermal actuators for assembly. The self-assembly method uses the forces derived from an energy field such as thermal, centrifugal force, or a magnetic field. Furthermore, residual stress and surface tension are also used for self-assembly. Recently, high precision robotics is used for automatic assembly process by standard or specially designed equipments. Some techniques for microassembly are reviewed in this section.

1-2-1 Microfabricated hinges

Surface micromachining [6] is the most common technique for fabricating MEMS devices. The standard surface micromachining has high planar resolution, but low vertical resolution and limited vertical range (usually less than 5 μm). These disadvantages have limited the development of three-dimensional designs until Pister et al. proposed the micro hinge structures [7]. A two-layer polysilicon process with oxide sacrificial layers was used to fabricate the hinge. This component enables surface micromachined structures to rotate out-of-plane by using the hinge structures. The schematic view of the hinge process and the SEM photo of a hinged structure are shown in Figure 1-8. This microhinge technique is a great breakthrough of surface micromachining for three-dimensional designs.



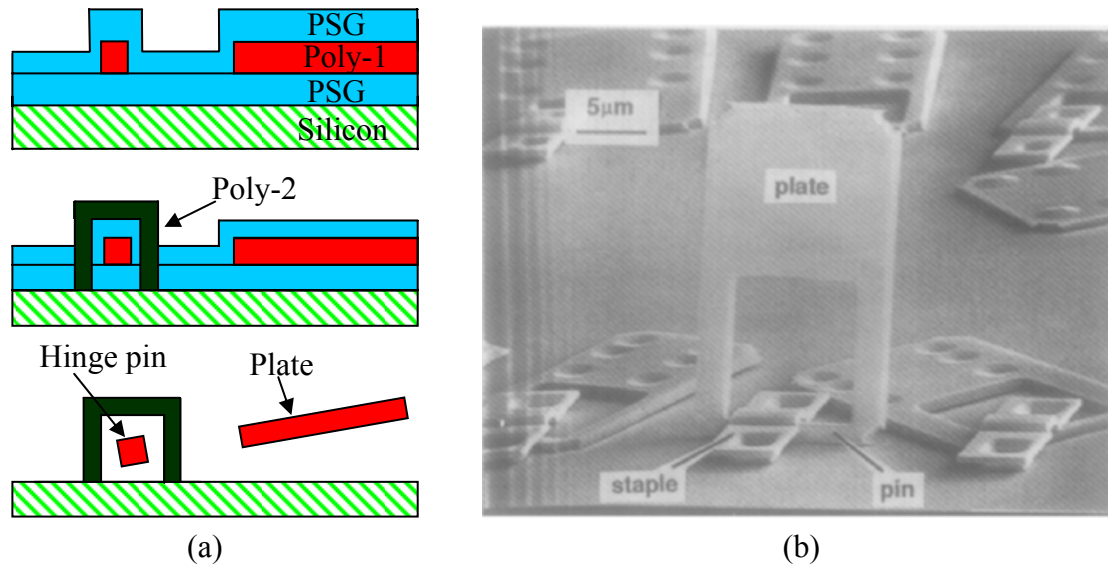
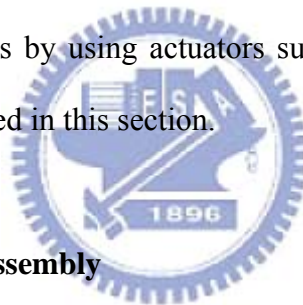


Figure 1-8 (a) Fabrication process of micro hinges, (b) SEM micrograph of a hinged structure [7].

1-2-2 Three dimensional MEMS by active assembly

The active assembly methods by using actuators such as scratch drive actuators and thermal actuators are reviewed in this section.



Scratch drive actuator active assembly

The scratch drive actuator (SDA), as shown in Figure 1-9, consists of a plate, a bushing, an insulator layer and a substrate electrode [8]. When a voltage is applied, the plate is pulled down toward the substrate by the electrostatic force. A part of the plate is pulled down to contact with the surface of insulator. The warp of plate causes the bushing to tilt and shifts a small distance. When the voltage is removed, the plate and the bushing return to their original positions, but translate forwards by a small distance. By driving the device with a periodic voltage, the SDA can go forward to a position decided by the frequency and amplitude of the driving signal. Figure 1-9 illustrates the structure and the working principle of the SDA [8]. Figure 1-10 shows a micromirror assembled by using an array of SDA [9].

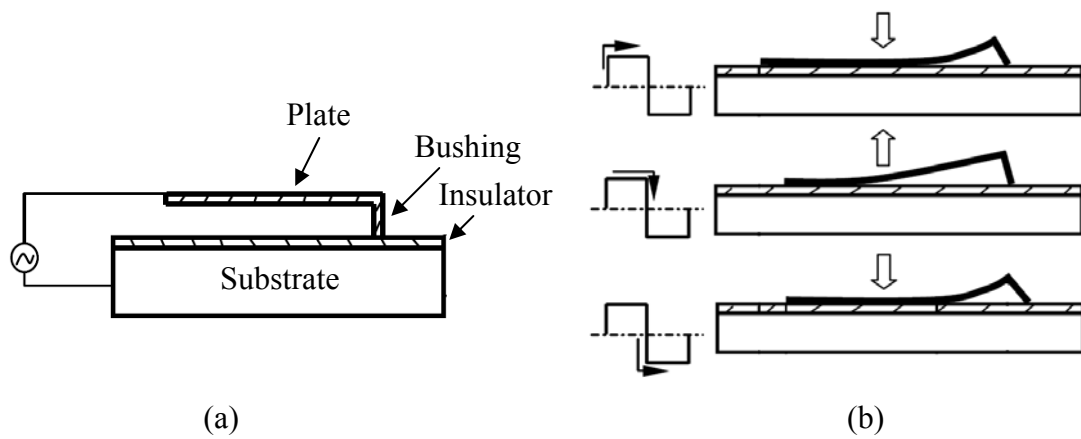


Figure 1-9 (a) Crossed sectional view of SDA, (b) working principle of SDA [8].

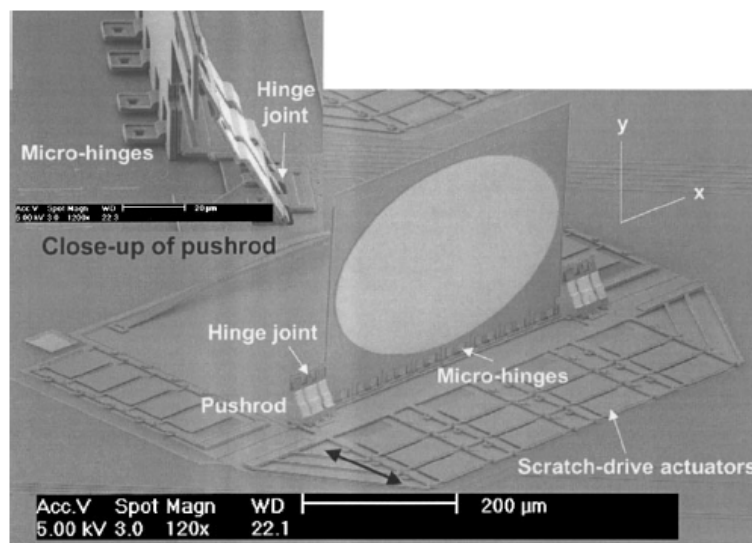


Figure 1-10 SEM of a free-rotating hinged micromirror lifted by an array of SDA [9].

Thermal actuator active assembly

Thermal actuators are also used in active assembly [10]. Figure 1-11 (a) shows the micro assembly system connected to a scanning mirror. The system consists of three parts: a linear assembly motor parts (a-c in Figure 1-11 (a)), a vertical actuator parts (d in Figure 1-11 (a)), and a self-locking mechanism part (e in Figure 1-11 (a)). The basic operation of the system is shown in Figure 1-11 (b). Initially, all components are on the surface of the substrate. The vertical thermal actuator is then used to lift the free end of the flip-up plate to form a triangle. The lateral thermal actuator then drives the base of the lift arm toward to the base of the flip-up plate, thus rotating the flip-up

plate around its hinge. Finally, the microstructure is positioned by self-engaging locking mechanism. Figure 1-12 (a) and (b) show the schematic of lateral thermal actuator and the SEM photograph of vertical thermal actuator, respectively. The lateral thermal actuators function by ohmic heating. The resulting displacement is shown in Figure 1-12 (a). The vertical thermal actuator consists of two parallel polysilicon beams separated by an air gap. At one end, the beams are connected together with a via, whereas at the other end, each arm is separately anchored to the substrate. Again, the hot arm has both higher electrical and thermal resistance than the cold arm due to the smaller width. As the hot arm expands, it drives the tip of the actuator downward towards the substrate. This results in the bowing in Figure 1-12 (b). When the current is removed from the system, the tip of the actuator deflects back away from the substrate and passes its original position. The back bending of the thermal actuator can apply an out-of-plan force to lift the structures. Figure 1-13 shows the SEM photos of the self-engaging locking mechanism and the assembled corner cube reflector.

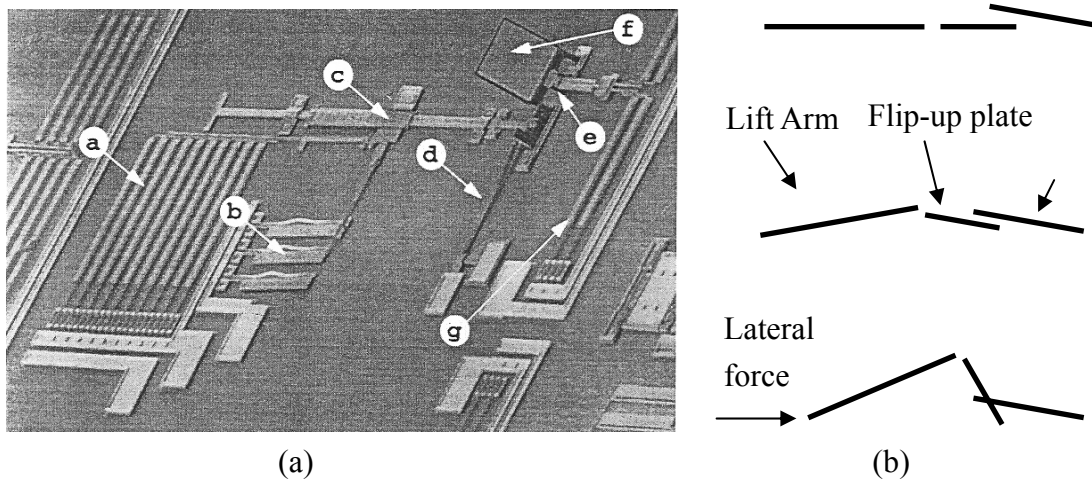
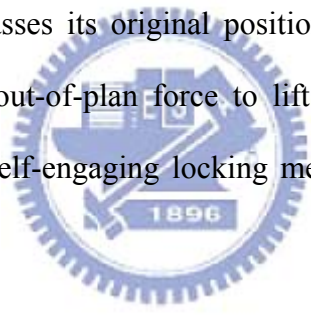


Figure 1-11 (a) SEM of the automated assembly system connected to a scanning mirror, (b) basic assembly process [10].

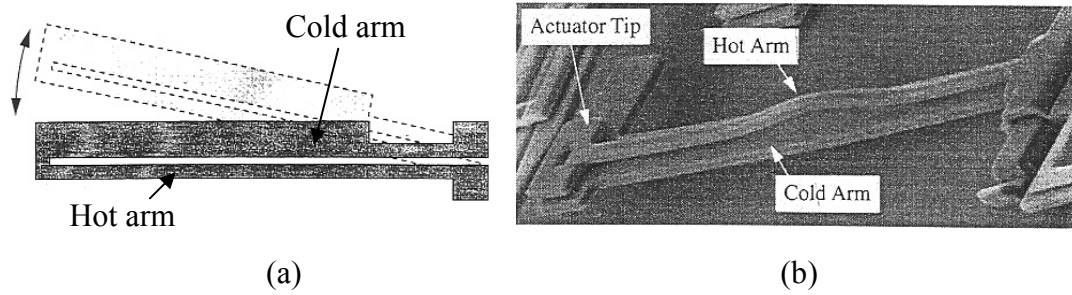


Figure 1-12 (a) Schematic of the lateral thermal actuator, (b) SEM of the vertical thermal actuator [10].

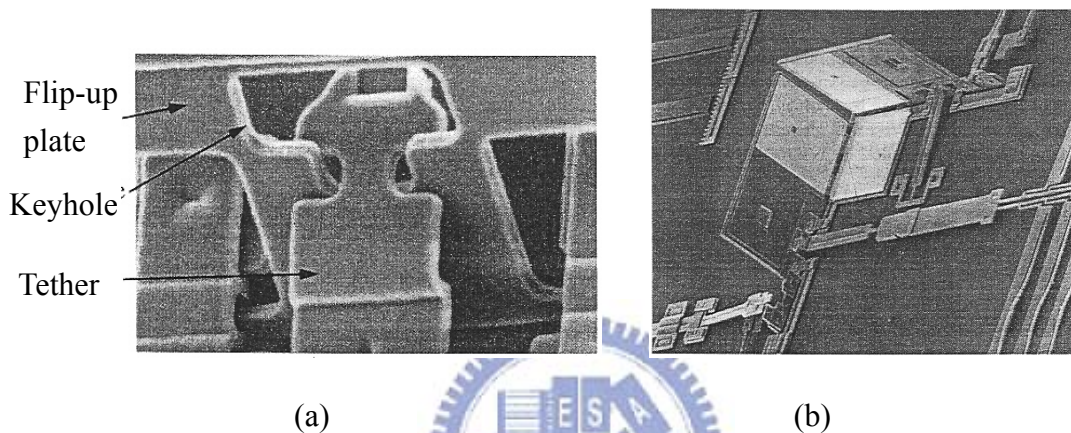


Figure 1-13 SEM of (a) the self-engaging locking mechanism, (b) an assembled corner cube reflector [10].

1-2-3 Three dimensional MEMS by self-assembly

In addition to the active assembly by actuators, self-assembly uses the force derived from an external energy field or the intrinsic force of the fabricated structures to flip the microstructures out of plane. Self-assembly by the magnetic force, centrifugal force, thermokinetic force, residual stress, and surface tension are reviewed in this section.

Magnetic force assembly

Figure 1-14 shows the principle of employing the magnetic force to lift hinged structures out of plane. Magnetic material such as Permalloy is electroplated on the

hinged flap. When an external magnetic field is applied, the hinged flap rotates around the pin axis. The rotation angle is determined by the volume of the magnetic material and strength of the applied magnetic field. Sequential assembly can be achieved by changing the magnetic field strength with different volumes of the magnetic material on the flaps [11]. Recently, Iwase et al. proposed another method of multi-step sequential assembly by changing the geometry of the elastic hinges, as shown in Figure 1-15 [12]. Permalloy was electroplated on the plate which was connected by elastic hinges on one side to the substrate, as Figure 1-15 (a) shows. It was found that a dimensionless factor that depended on its shape determined the sensitivity of rotation of the hinged structures to the magnetic field. The volume of the magnetic material and the dimension of the elastic hinges defined the sensitivity factor, as Figure 1-15 (b) shows. When the hinged structure is placed in a magnetic field, the rotation angle of the plate is proportional to the sensitivity factor. Therefore, sequential assembly can be achieved by designing elastic hinges with different sensitivity factors. An example is shown in Figure 1-16. As the applied magnetic field H_{ext} is increased gradually, the plate with the largest sensitivity factor will rise to 90° first. With increased H_{ext} , the other plates with smaller sensitivity reach 90° and each plate is interlocked by the friction force.

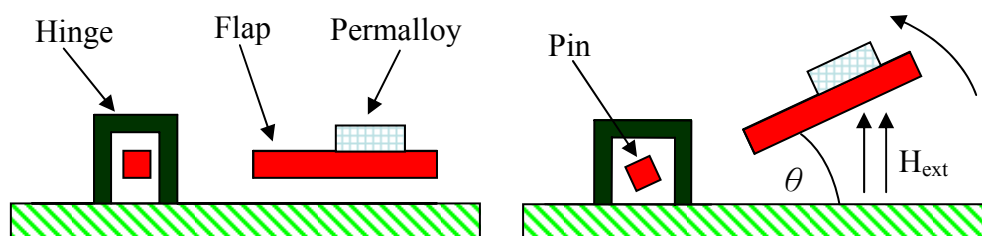


Figure 1-14 Magnetic force assembly.

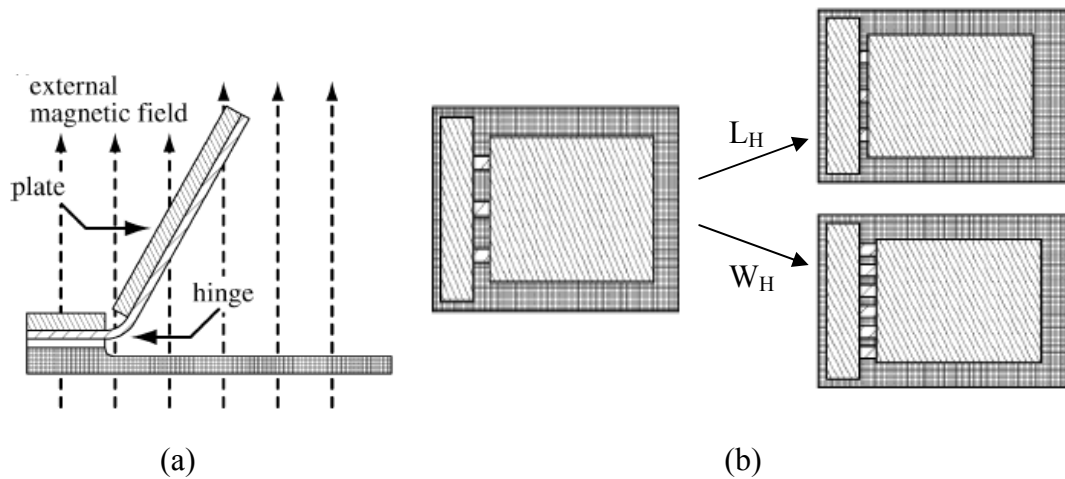


Figure 1-15 (a) Side view of a hinged microstructure in an external magnetic field, (b) hinge with different dimensions and sensitivity factors [12].

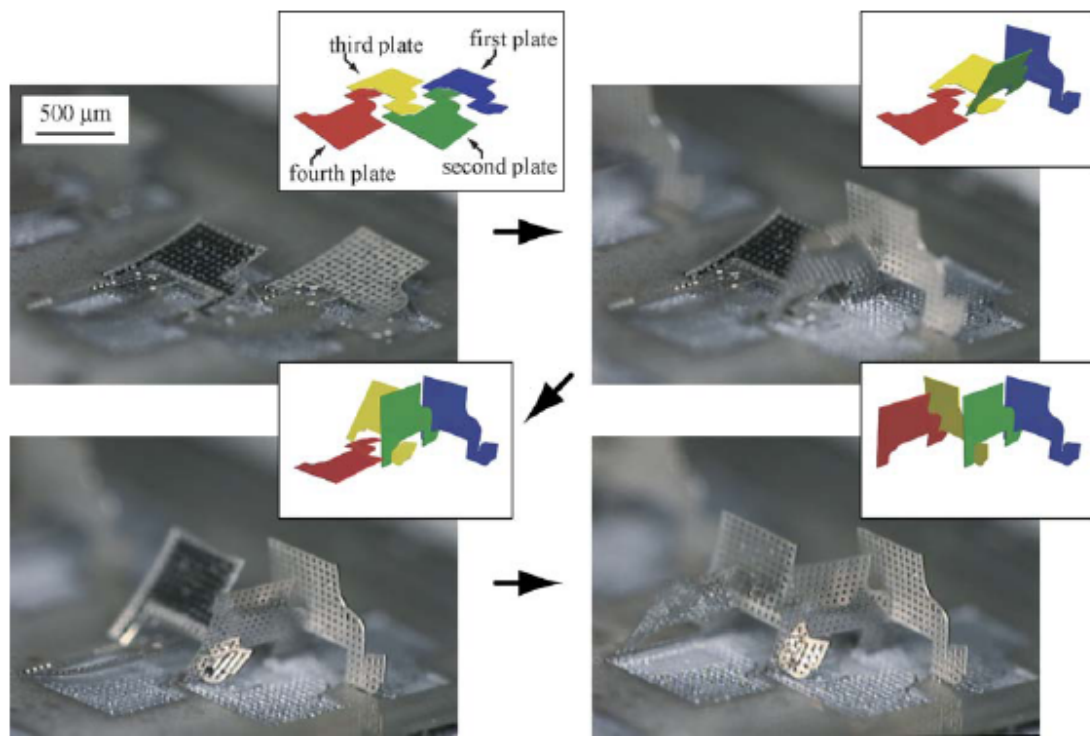


Figure 1-16 Step-by-step photographs of the four-step sequential assembly [12].

Centrifugal force assembly

For microscale components, inertial forces such as gravity are usually neglected when compared with surface forces or friction forces. As an inertial force, the centrifugal force can overcome surface forces and friction forces since it is proportional to the square of the rotating speed. Therefore, the centrifugal force can

be used to raise the hinged surface micromachined structures [13]. The concept of this method is illustrated in Figure 1-17. The chip is attached on the surface of rotational disk and is perpendicular to the rotational axis. The hinged structure will be raised out of plane when the rotation starts, as shown in Figure 1-17. Then the microstructure is locked by the latch mechanism. Figure 1-18 shows the batch assembly by using the centrifugal force.

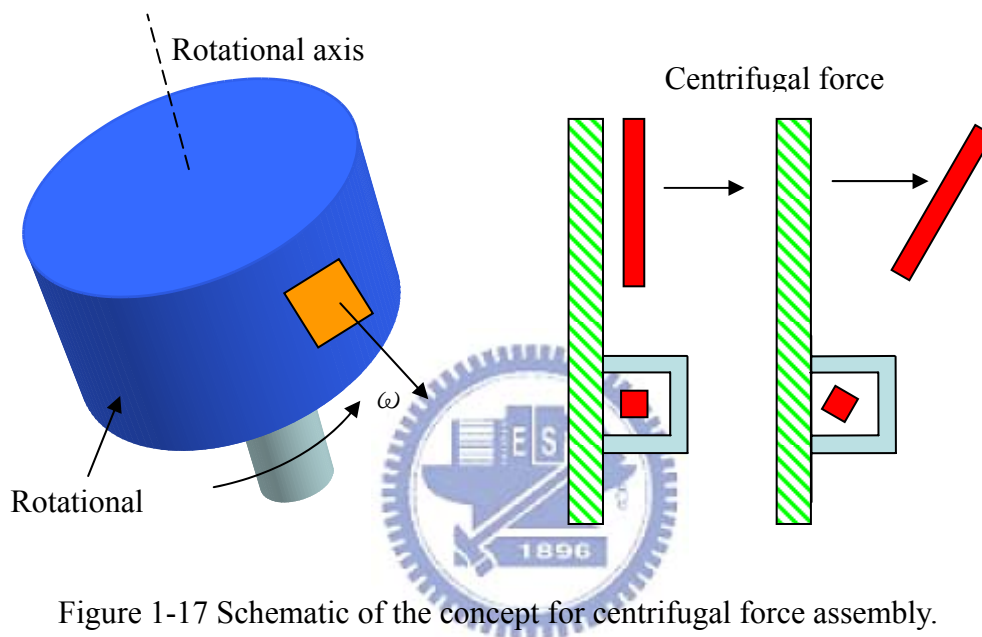


Figure 1-17 Schematic of the concept for centrifugal force assembly.

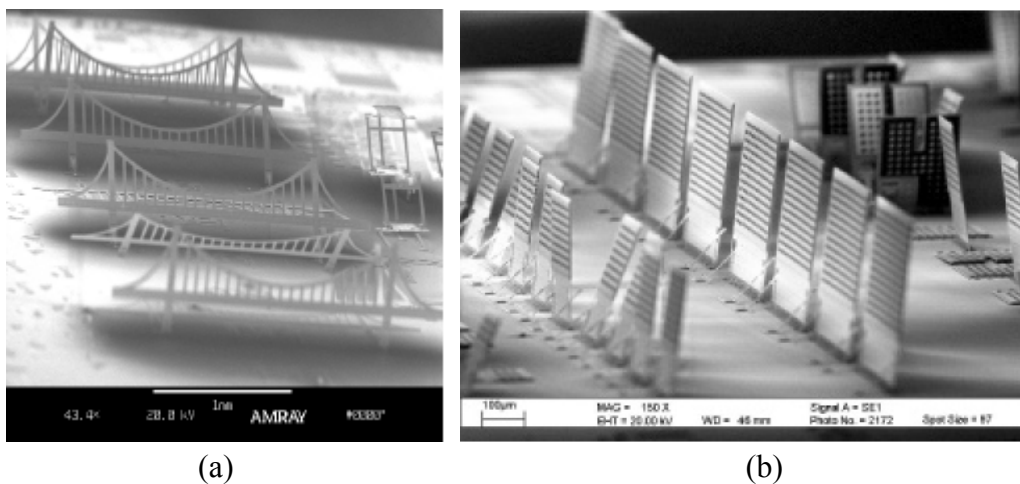


Figure 1-18 Batch assembly by centrifugal force: (a) an array of bridge structures, (b) an array of micromirrors [13].

Thermokinetic force assembly

Thermokinetic force can be used to assemble 3-D structures by heating the surface of devices [14]. Figure 1-19 shows the principle and experimental apparatus for raising structures by thermokinetic force. The assembly mount was placed in a vacuum chamber with low pressure in molecular flow regime. The chip was held on the PZT plate by high vacuum suction. The PZT plate was soldered to a hot plate with temperature control to adjust the substrate temperature. The PZT plate was used to overcome the hinge friction by apply a small vibration with high frequency. Since the average velocity of gas molecules bombarding the die surface and flaps are proportional to the temperature, a differential pressure causes the out-of-plane force. Since the temperature of the die surface is larger than that of the vacuum ambience, the flaps can be lifted out of the substrate and assembled in the upright position, as shown in Figure 1-20.

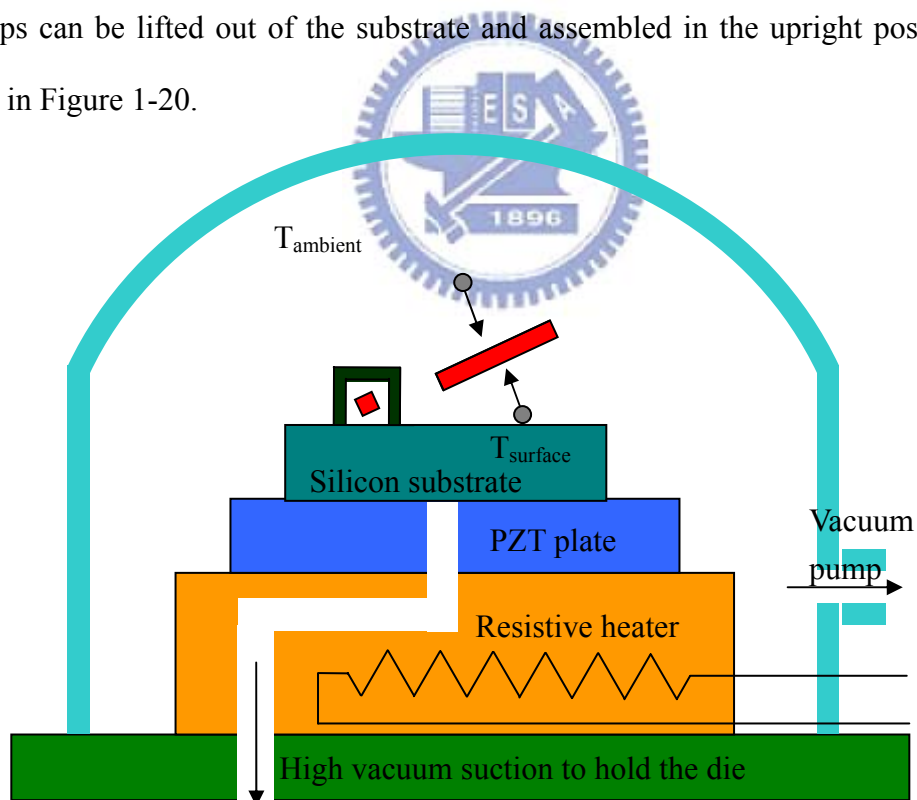
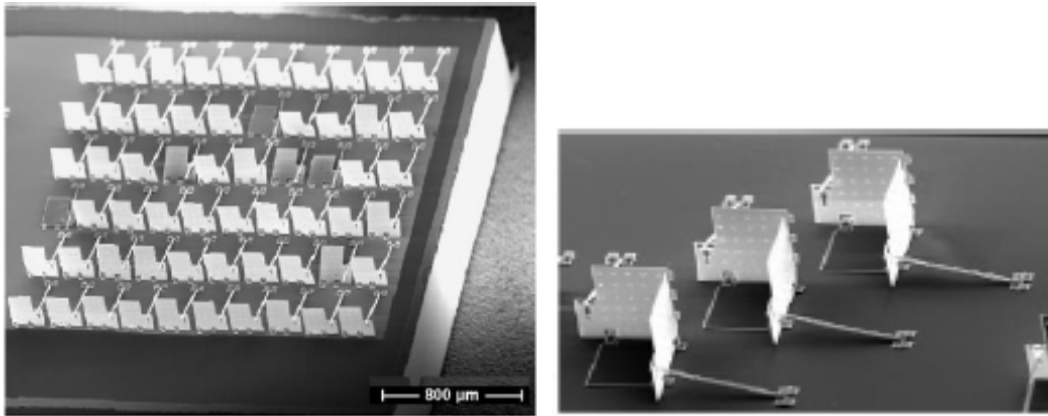


Figure 1-19 Schematic of thermokinetic force assembly.



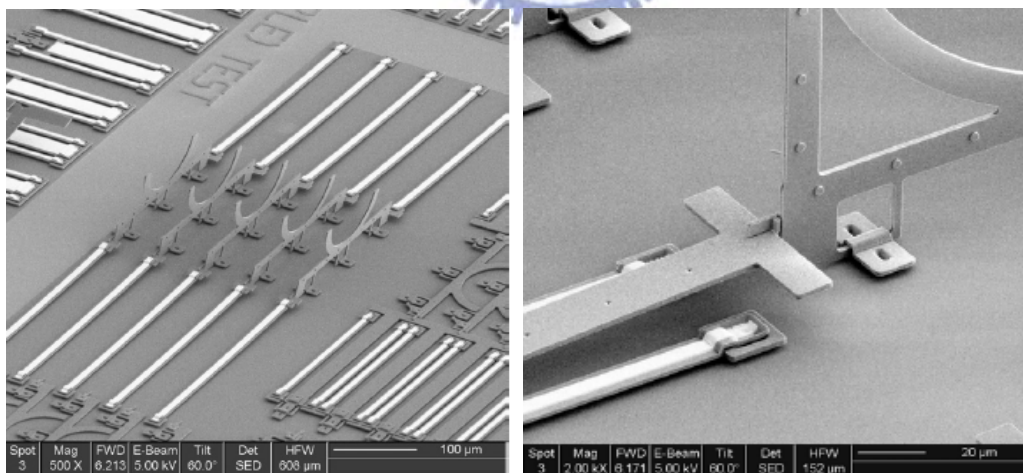
(a)

(b)

Figure 1-20 Assembly by thermokinetic force: (a) an array of micromirrors, (b) corner cube reflectors [14].

Stress-induced assembly

Residual stress can lead to curvature of released surface-micromachined structural layers. The bending of released microstructures can be used as motive force to assemble 3-D micro structures. In Figure 1-21, a typical assembly mechanism is composed of stress-induced bimorph beams and locking components [15].



(a)

(b)

Figure 1-21 (a) Assembled structures by combining bimorph beams with locking mechanism, (b) locking mechanism [15].

Surface tension powered assembly

Surface tension can be used for self-assembly [16]. Meltable materials such as photoresist or solder are first patterned on the rotational joint. When the photoresist or solder is heated and reflowed, it changes into a spherical shape to minimize surface energies, and thus the plate is flipped up. The final rotational angle is determined by the geometry of the meltable material. Some complex 3D microstructures can be constructed with appropriate locking latches. Figure 1-22 shows the assembled micromirror by reflow of photoresist and solder [16, 17].

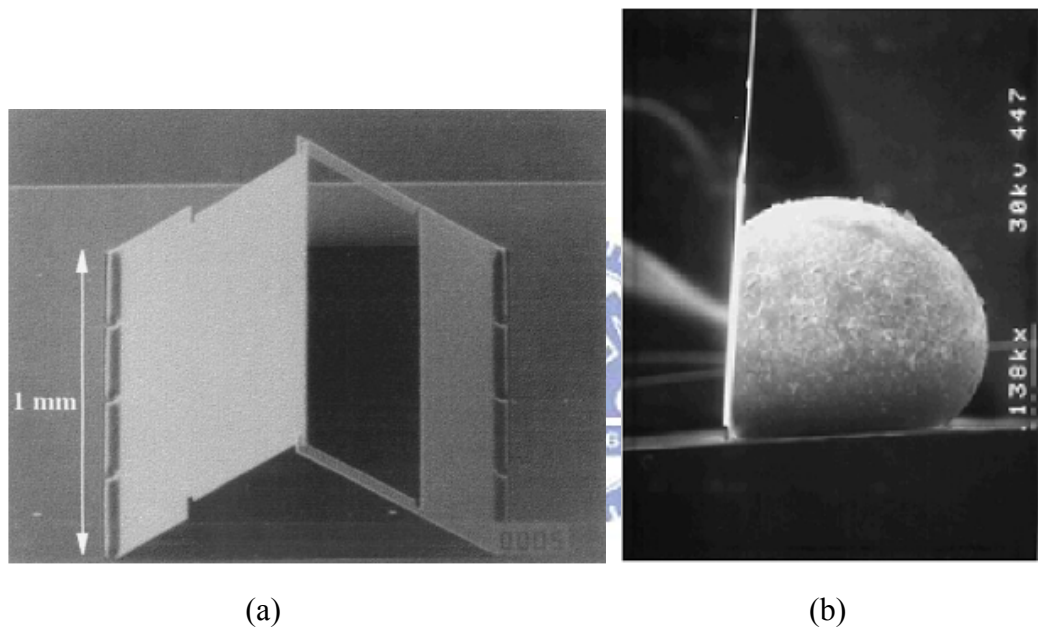


Figure 1-22 Surface tension powered assembly by (a) photoresist [16], (b) solder [17].

1-2-4 Manual or robot-assisted assembly

Manual assembly by using microprobes is the first method for raising 3-D microstructures; but it is time consuming and has low yield. In recent years, automatic robotic systems are used to pick and place microstructures for automatic assembly. These assembly techniques are reviewed in this section.

Robot-assisted assembly

High precision robots can be used to assemble 3-D microstructures by integrating microgrippers [18] or non-actuated end-effectors [19] on the robotic arms, as shown in Figure 1-23. The gripper consists of two arms that either open or close upon actuation. The microparts are picked by actuating the microgrippers or inserting the non-actuated end-effectors into the appropriate locking mechanism. Figure 1-24 shows the assembly flow by using non-actuated end-effectors. After the end-effector is attached to the robotic arm by melting solder on the solder pad, the de-tether process of microparts is accomplished by breaking the tether (Figures 1-24 (a) and (b)). Next, the end-effector is aligned to the microparts and inserted into it. A micropart can be picked up off the substrate by inserting the end-effector into an appropriate compliant handle, which applies a clamping force on the end-effector (Figure 1-24 (c)). The picked microparts can be assembled on the substrate by designing appropriate locking mechanism between microparts and connectors on the substrate (Figure 1-24 (d)). After inserting the microparts into the connector on the substrate, the end-effector can be released by overcoming the friction of the compliant handle (Figure 1-24 (e)). Figure 1-25 shows the SEM image and optical micrograph of assembled device.

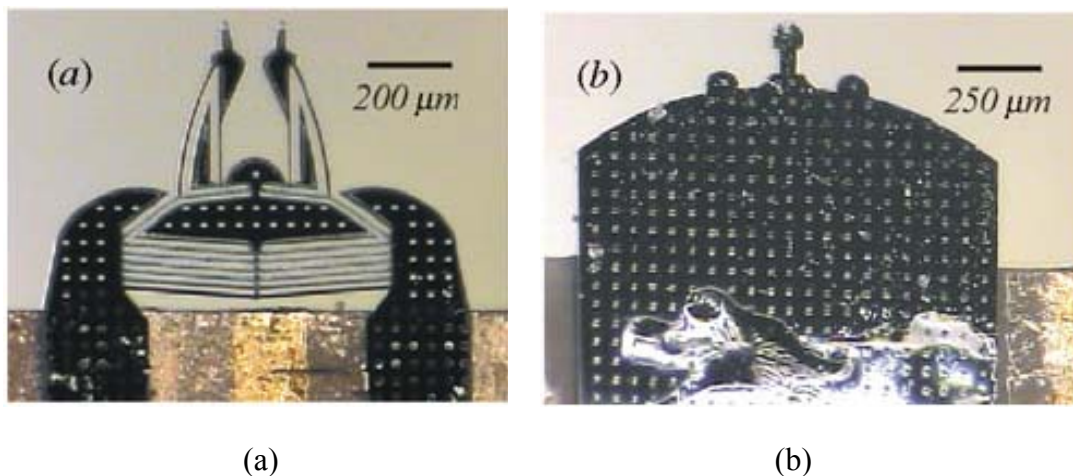


Figure 1-23 (a) MEMS electrothermal gripper, (b) MEMS end-effector [19].

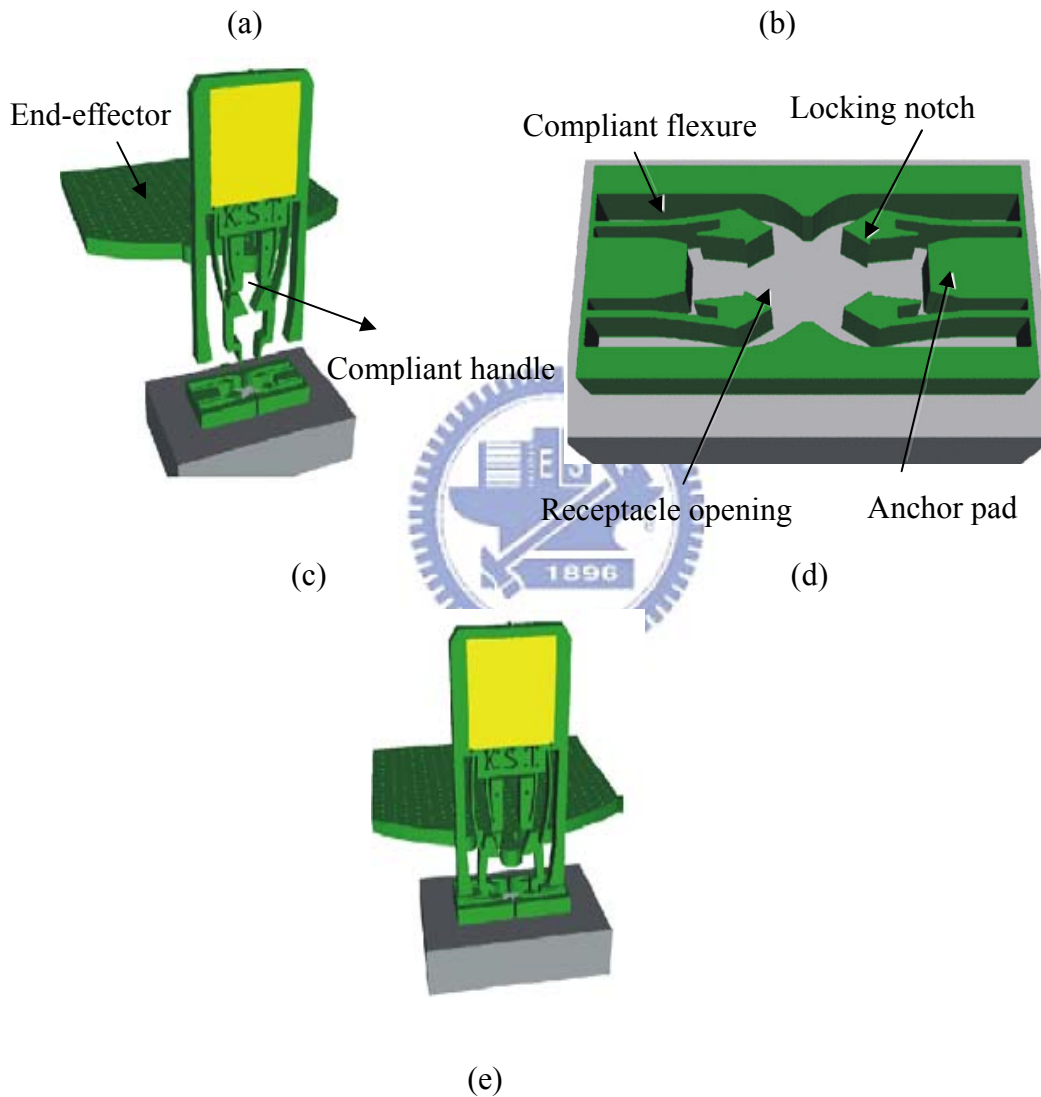
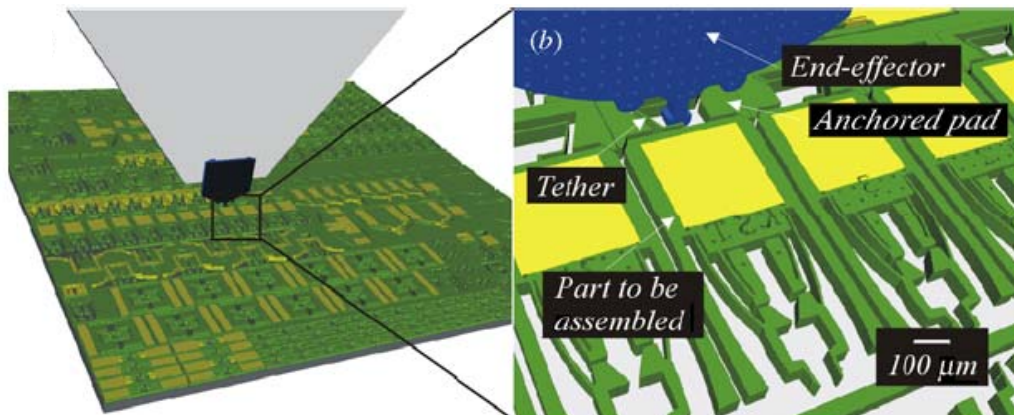
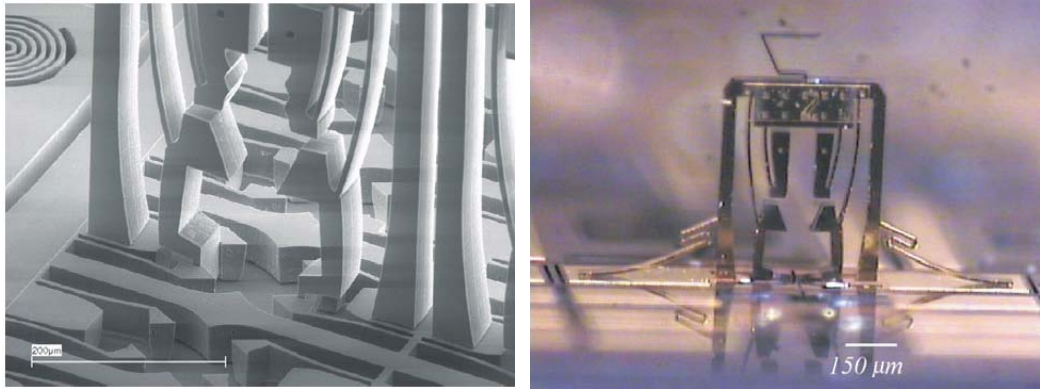


Figure 1-24 (a) Overview of whole chip where assembly is taking place, (b) close up of the de-tether process, (c) a micropart is picked off the substrate, (d) schematic of microconnector, (e) the connector being inserted into the socket [19].



(a)

(b)

Figure 1-25 (a) SEM image, (b) optical micrograph of assembled device [19].

Hingeless 90° out-of-plane microstructures

Another technique for microassembly by using automated probing systems and hingeless microstructures was developed in [20]. Microstructures can be assembled to 90° using a single lateral push provided by a wirebonder tip or a microprober tip. The concept is based on compliant hinges which can have out-of-plane motion by redirecting lateral displacement in rotation. As shown in Figure 1-26, the serpentine springs are designed to be relatively stiff in the in-plane direction and compliant in the out-of-plane direction. When a lateral force is applied to the actuation point, the resulting moment twists the spring and cause out-of-plane motion. The assembly sequence is illustrated in Figure 1-27. The lateral actuation force (F_a) and the restoring force of the springs (F_s) produces an out-of-plane torque after the bottom of device contacts the substrate (Figure 1-27 (b)). As the probe slides in the lateral direction, the rotational torque increases when the spring is stretched (Figures 1-27 (c) and (d)). When the plate reaches a particular angle, the spring begins to pull on the center plate (Figure 1-27 (e)) until the structure finally reaches the upright position (Figure 1-27 (f)). Figure 1-28 shows the optical micrographs of manual assembly procedures and the SEM images of assembled devices.

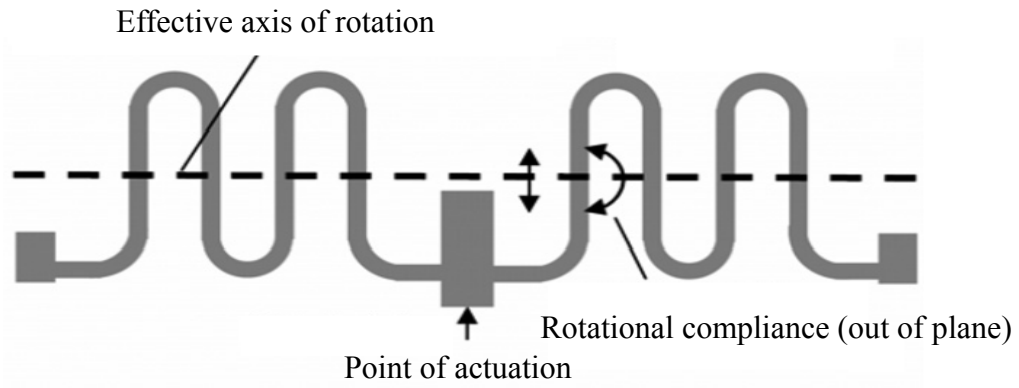


Figure 1-26 Hingeless device concept [20].

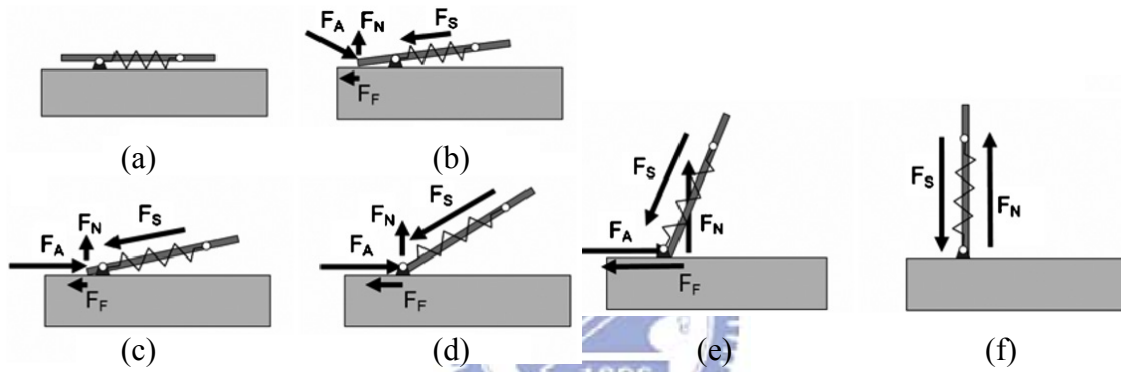


Figure 1-27 Schematic assembly sequence [20].

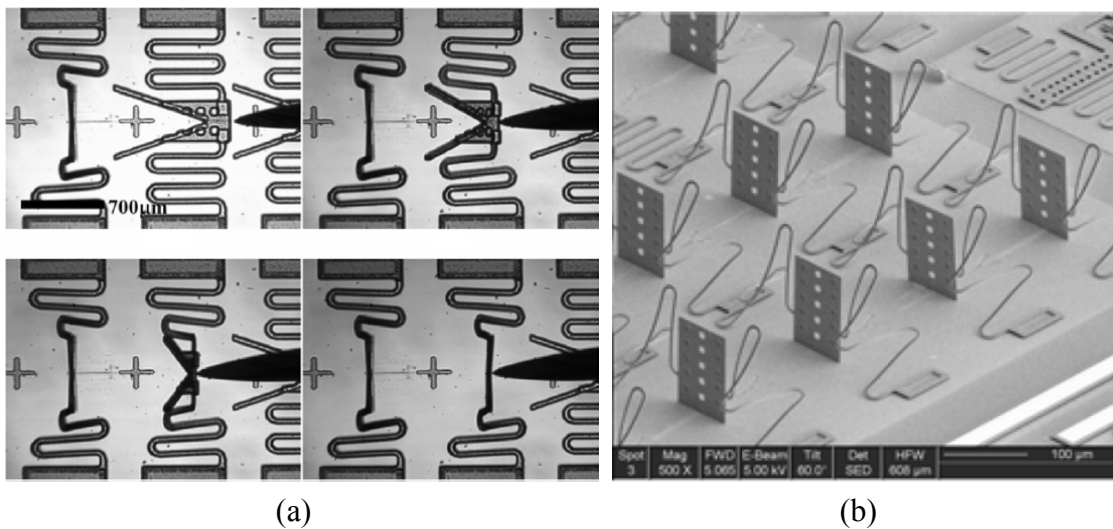


Figure 1-28 (a) Optical micrographs of the assembly process (b) SEM image of 90° out-of-plane structures [20].

Assembly of 3D microstructures using one-push operation

One of the major difficulties in manual or automated assembly of 3D MEMS structures is the control and positioning of probe or pickup tips. Since the gap spacing between the released components and the substrates is very small, inserting probes into the gap involves precise motion control in multiple degrees of freedom. A novel automated assembly with simple one-push operations in the vertical direction and large probe positioning tolerance in both vertical and lateral directions are proposed in our previous work [21]. Figure 1-29 shows the assembly process of a 90° micromirror with the one-push operation. A through-wafer hole is etched under the push pad. When a micro probe pushes the pad down, the mirror is flipped up (Figure 1-29 (a)). Once the mirror moves out of the plane, the wing of the mirror plate contacts the bottom of the side latch. This upward force simultaneously drives the flexible side latches to rotate out of the plane (Figure 1-29 (b)). When the mirror plate rotates to the upright position, it slides into the V-shaped slot of the flexible side latches (Figure 1-29 (c)). The V-shaped slot and the downward restoring force of the spring will firmly lock the mirror plate in place even after the probe moves away (Figure 1-29 (d)). The flip-up mirrors are fixed to the substrate by the novel V-shaped hinge instead of a staple hinge, as shown in Figure 1-30. The downward force of the bent beams can eliminate the vertical play space of hinge and fix the hinge pin on the substrate. Furthermore, the hinge pin is locked between the two sides of the V-shaped structure when the mirror is in the upright position. Hence the transverse play can also be eliminated. The other advantage of the one-push method is that multiple 3D microstructures can be assembled in batch by using a probe array. It can reduce the assembly time and cost. Figure 1-31 shows the SEM images and optical micrograph of assembled devices.

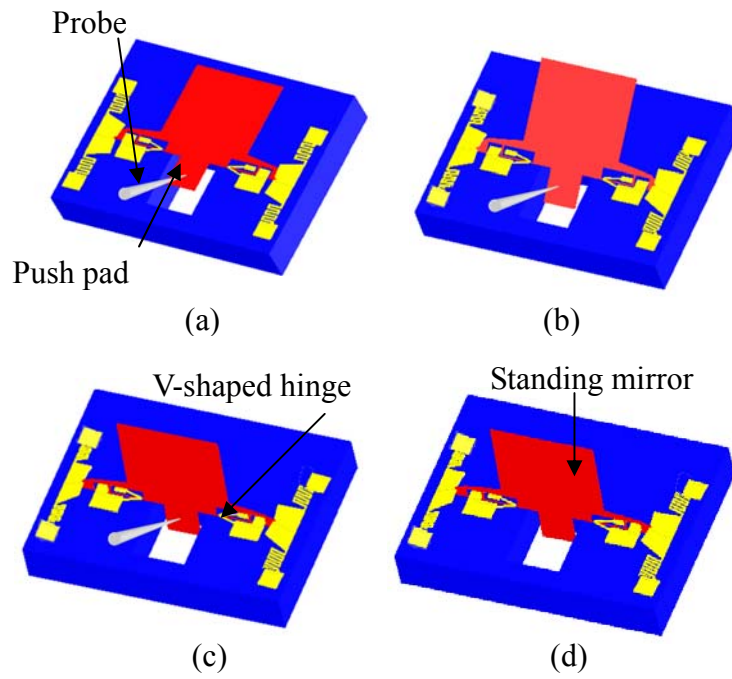


Figure 1-29 Assembly process with one-push operation [21].

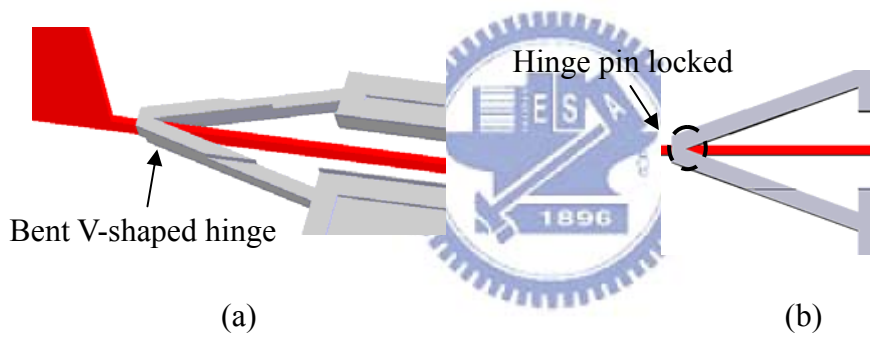


Figure 1-30 (a) Schematic view of the V-shaped hinge after assembly, (b) top view.

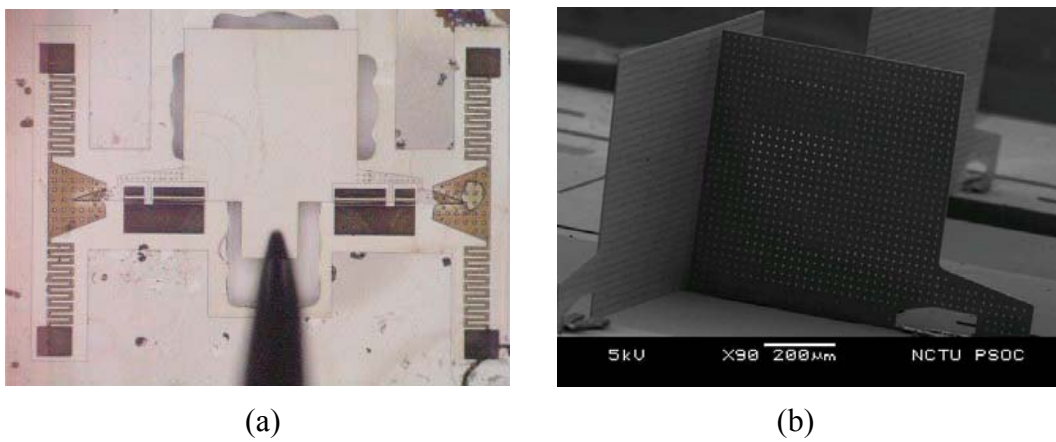
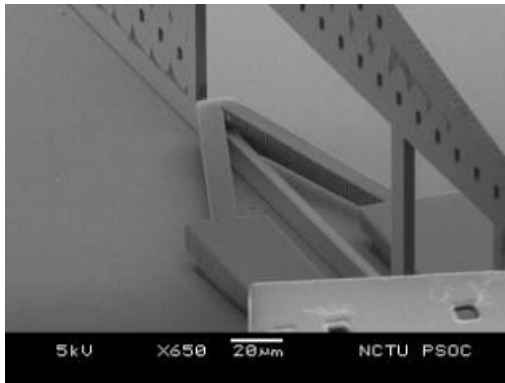
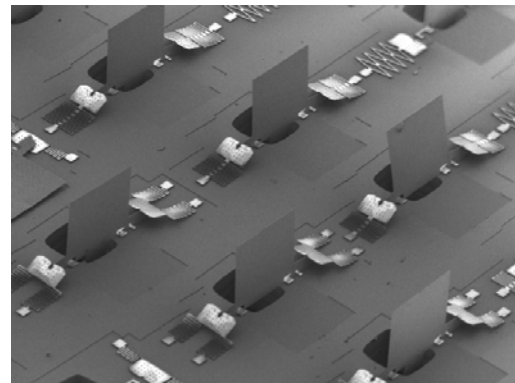


Figure 1-31 SEM images and optical micrograph of assembled devices, (a) Mirror is flipped by one-push operation, (b) a corner cube reflector. [21].



(c)



(d)

Figure 1-31 SEM images and optical micrograph of assembled devices (continued), (c) close up view of the V-shaped hinge, (d) an array of micromirrors [21].

1-3 Objective and organization of the thesis

The objective of this research is to fabricate a MEMS-based optical pickup head for blue wavelength. The proposed optical pickup head is composed of a laser diode, a 135° MEMS mirror, a 135° MEMS mirror with holographic optical element (HOE), an objective lens, and a photodetector, as shown in Figure 1-32. Detailed design and principle of the optical system is discussed in Chapter 2. The main components of the optical bench are the two 135° MEMS mirrors. The one-push method in our previous work [22] is used to assemble the 90° and 45° out-of-plane microstructures.

Therefore, the objectives of this thesis include:

1. improving angular accuracy of 45° devices;
2. developing assembling technique for 135° mirrors;
3. assembly of laser diode, photodetector, and objective lens on the fabricated optical bench;
4. optical and electrical testing of assembled optical pickup head.

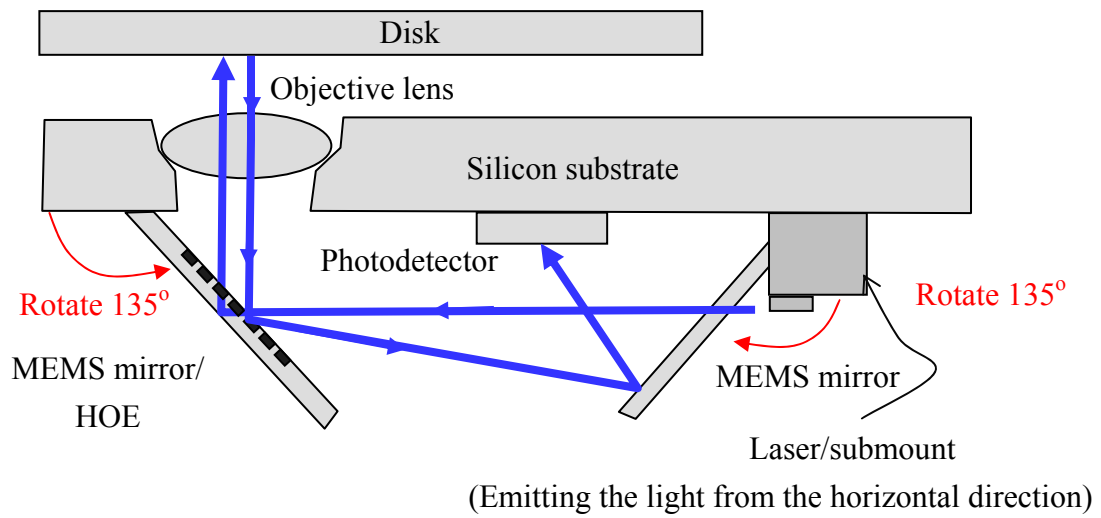
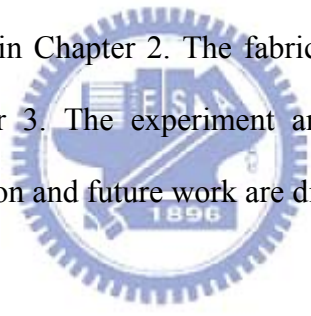


Figure 1-32 Schematic of the MEMS-based optical pickup head in this thesis.

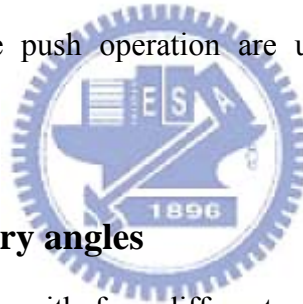
The basic principles and simulation of the proposed optical pickup head and assembly method are presented in Chapter 2. The fabrication processes and process issues are discussed in Chapter 3. The experiment and measurement results are presented in Chapter 4. Conclusion and future work are discussed in Chapter 5.



Chapter 2 Principle and Design

2-1 Introduction

A novel MOEMS platform employing SOI wafers and simple push operation as the assembly method is proposed to fabricate the optical bench. The simple push operation was demonstrated in our previous study [22]. It has large probe positioning tolerance in both vertical and lateral directions. In this platform, torsional beams are used to replace micro hinges in assembled structures. Nonvertical micromirrors are developed since the optical system has two 135° mirrors. The optical bench is an optical pickup head for blue-wavelength. The principles of the assembly method and the optical system are discussed in this chapter. Micromirrors with arbitrary angles assembled by using the simple push operation are used to verify the proposed assembly technique.



2-2 Mirror with arbitrary angles

In this section, micromirrors with four different angles are used to verify the methods of assembling of mirrors with arbitrary angles. The 30° , 45° , and 60° micromirrors are assembled by two push operations. 135° mirrors are assembled with a different assembly process. In our previous demonstration [22], the average angle of the assembled 45° micromirrors was $45.89^\circ \pm 0.2^\circ$. The cause and solution of this problem are investigated in this thesis.

2-2-1 30° , 45° , and 60° mirrors

The assembly method and design principle of these three mirrors are the same. Therefore, 45° devices are used to illustrate the design principle and assembly process. The layout view and 3-D model of the proposed 45° mirrors are shown in Figure 2-1.

The mirror and support are built by using only the device layer of the SOI wafer, whereas the substrate provides the space for pushing. The sizes of the mirror plate and the push pad are $(760 \mu\text{m})^2$ and $(250 \mu\text{m})^2$, respectively.

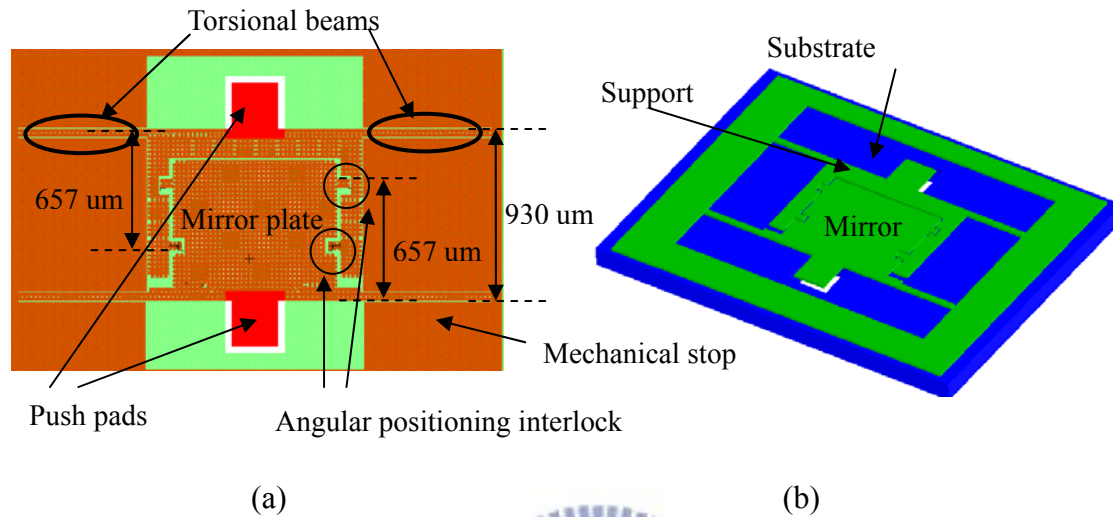


Figure 2-1 (a) Layout design of the 45° device, (b) 3-D model.

The assembly process of the 45° device is shown in Figure 2-2. Two push operations are needed in the assembly process. First, Probe 1 pushes the support to over 60° and hold in this position (Figure 2-2 (a)). Then Probe 2 pushes the mirror plate to 40° to 50° (Figure 2-2 (b)). Subsequently Probe 1 is removed and the torque from the torsional beams drives the support to lie on the mirror plate (Figure 2-2 (c)). After Probe 2 is removed, the torque of the torsional beams connected to the mirror plate also drives the mirror plate to lie on the support. Finally, the support and the mirror plate are interlocked (Figure 2-2 (d)).

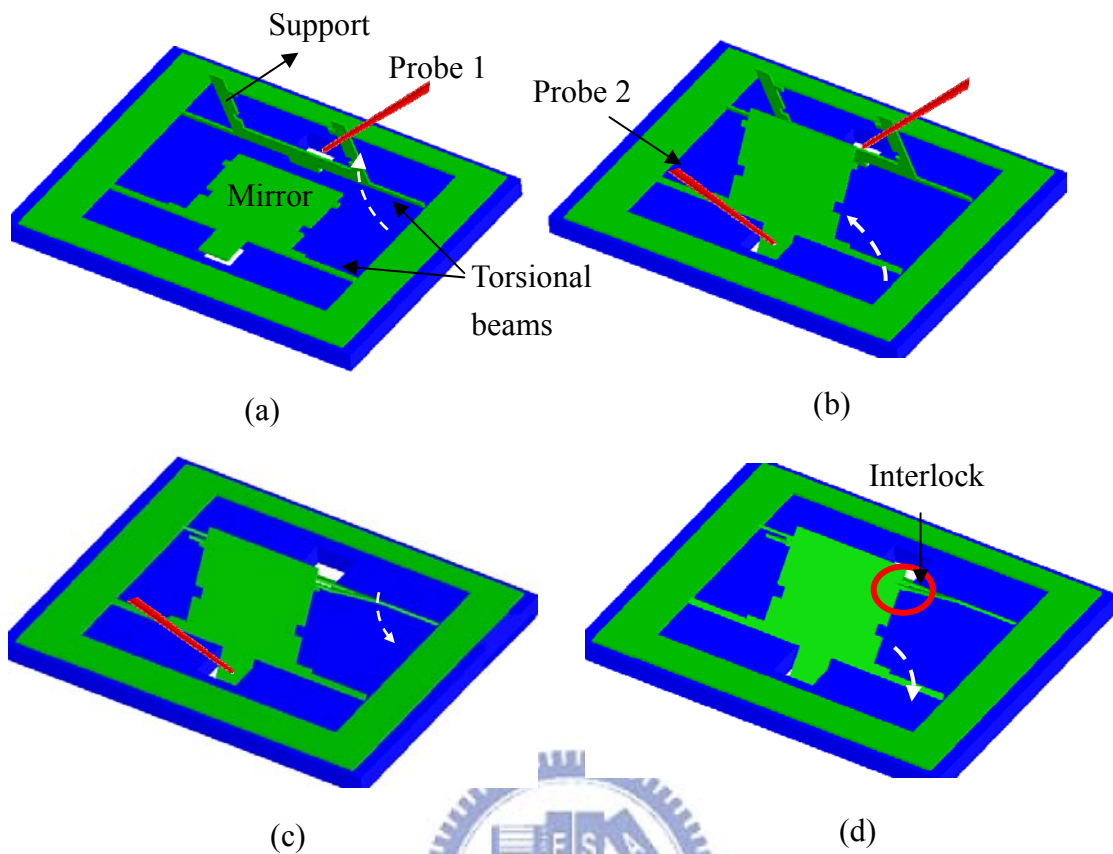


Figure 2-2 Assembly process of the 45° device.

The layout views of the 30° and 60° mirrors are shown in Figure 2-3. The design principle and assembly process is the same as the 45° mirrors. The sizes of mirror plates are $(760 \mu\text{m})^2$ and $(250 \mu\text{m})^2$, respectively.

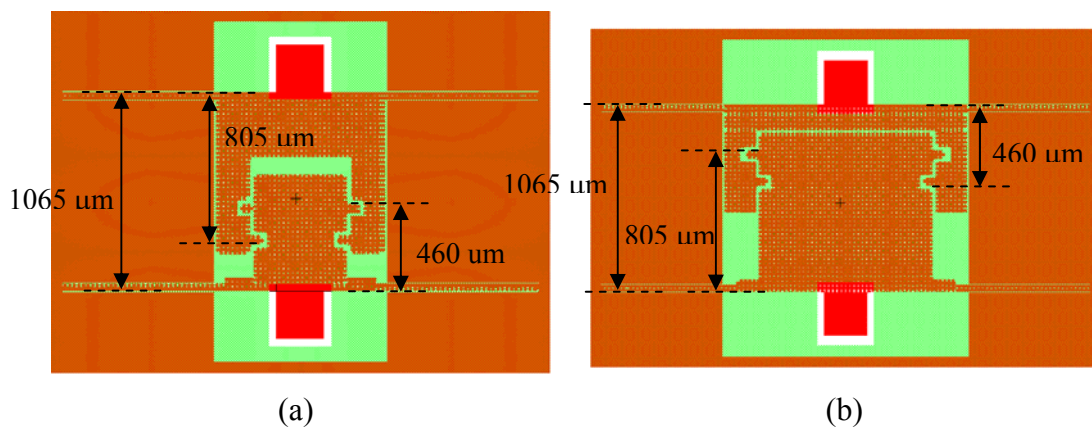


Figure 2-3 Layout design of (a) 60° device, (b) 30° device.

Torsional beams

For a 45° mirror, the twist angle of the torsional beams is 45°. However, during the assembly process the support is pushed by more than 80°. Thus a twist angle of 80° is assembled in this design. Torsional beams are provide the restoring force and the design is based on the torsional formula of a beam with a rectangular cross section [23],

$$\theta = \frac{TL}{KG}, \quad (2-1)$$

$$K = ab^3 \left[\frac{16}{3} - 3.36 \frac{b}{a} \left(1 - \frac{b^4}{12a^4} \right) \right], \text{ for } a > b, \quad (2-2)$$

$$\tau_{\max} = \frac{3T}{8ab^2} \left[1 + 0.6095 \frac{b}{a} + 0.8865 \left(\frac{b}{a} \right)^2 - 1.8023 \left(\frac{b}{a} \right)^3 + 0.9100 \left(\frac{b}{a} \right)^4 \right], \text{ for } a \geq b, \quad (2-3)$$

where θ is the angle of twist, T is the applied torque, L is the beam length, K is a constant depending on the geometry of beam, G is the shear modulus, τ_{\max} is the maximum shear stress at the midpoint of the longer side between a and b , a and b are the half of the longer and shorter sides of the cross section of the beam, respectively (Figure 2-4).

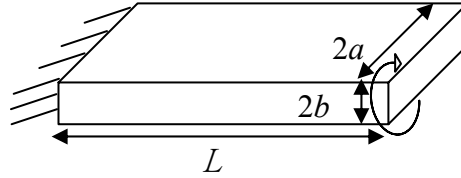


Figure 2-4 Form and dimensions of cross sections.

The device layer of the SOI wafer is 5 μm thick and therefore b is 2.5 μm . The width of the beam is 20 μm and therefore a is 10 μm . The shear modulus of single-crystal silicon is 79.9 GPa [24] and the yield stress of single-crystal silicon is 7 GPa [25]. The maximum shear stress in these structures at $\theta = 80^\circ$ must be smaller than the yield strength, therefore $\tau_{\max} = 2$ GPa is used in this design for a safety factor of 3.5. By substituting these values into Equations 2-1, 2-2, and 2-3, K and T are

$702.13 \times 10^{-24} \text{ m}^4$ and $281.73 \times 10^{-9} \text{ N} \cdot \text{m}$, respectively. From Equation 2-1, L can be found to be $398 \text{ } \mu\text{m}$.

Support rigidity

Support arms are used to lock the mirror plate and apply an opposite torque to lock the mirror plate. The structural strength of the support arms is related to the bending of support arms after the assembly process. When the device is in static equilibrium after assembly, the restoring moment M_0 from the torsional beam is applied on the support arm, as shown in Figure 2-5. Therefore, the bending of the support arms is related to the moment from the torsional beams and the rigidity of the support arms. The curvature of the bending support arm can be calculated from

$$\rho = -\frac{EI}{M_0} \quad (2-4)$$

$$I = \frac{1}{12}WH^3 \quad (2-5)$$

where E is the Young's modulus, I is the moment of inertia depending on the geometry of the support arms, M_0 is the moment acting on the support after the mirror is assembled. Young's modulus of silicon is 169 GPa . M_0 is equal to T in Equation 2-1. The geometry of torsional beams is $700 \text{ } \mu\text{m}$ (L) \times $20 \text{ } \mu\text{m}$ (W) \times $5 \text{ } \mu\text{m}$ (H) in our design. By substituting these values into Equation 2-1 and 2-2, M_0 is $62.94 \times 10^{-9} \text{ N} \cdot \text{m}$. The angle deviation from the bent support can be calculated, as shown in Figure 2-6. The radius of curvature can be calculated from Equations 2-4 and 2-5. Three different width of support arm with same length l is $657 \text{ } \mu\text{m}$ are designed in this thesis. The angular deviation can be calculated from Figure 2-6. Table 2-1 show the calculation results of radius of curvature and the angle deviation with the same geometry of torsional beams ($700 \text{ } \mu\text{m}$ (L) \times $20 \text{ } \mu\text{m}$ (W) \times $5 \text{ } \mu\text{m}$ (H)) in the reality design.

Table 2-1 Calculation of angular deviation.

Support arm width	120 μm	250 μm	350 μm
Radius of curvature of bent support	6.71 mm	13.99 mm	19.58 mm
Angular deviation	0.23°	0.11°	0.08°

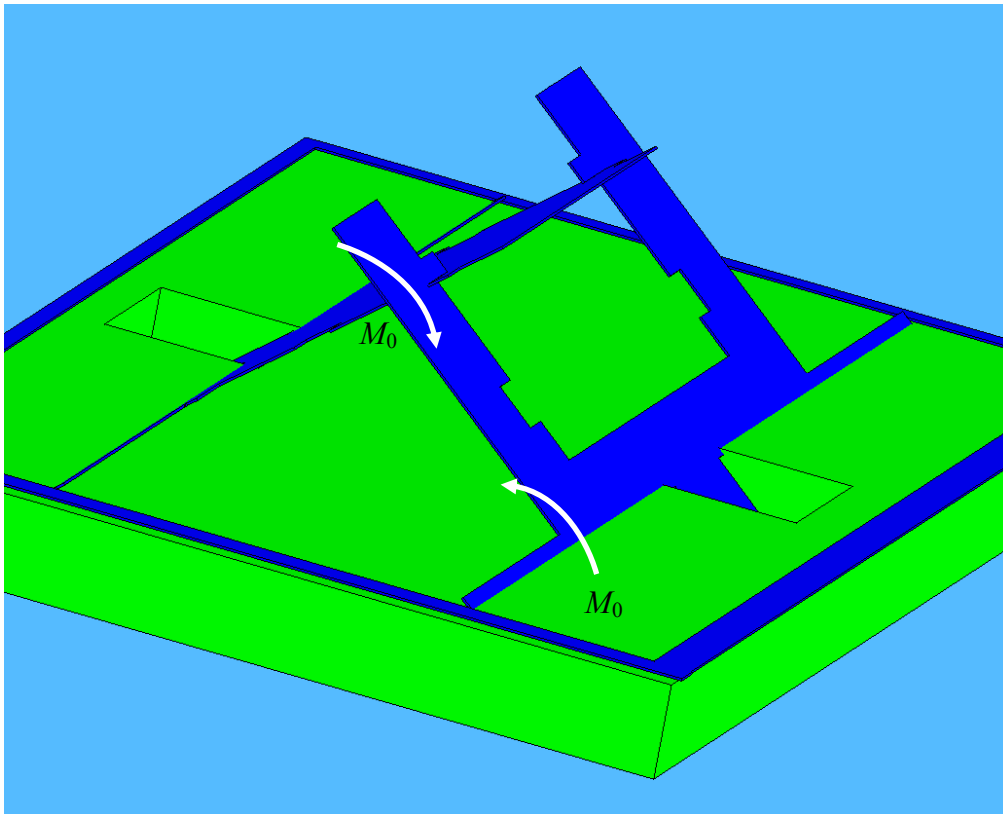


Figure 2-5 Schematic of static equilibrium after assembly.

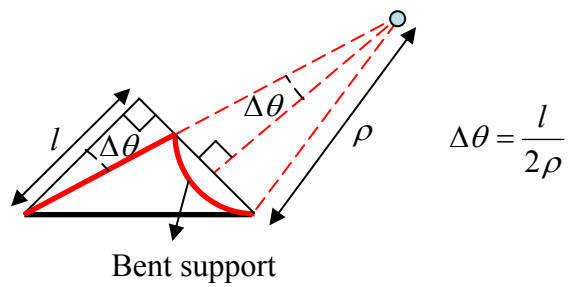


Figure 2-6 Schematic of assembled 45° mirror with bent support.

2-2-2 135° mirror

The 135° mirror is composed of a mirror plate and support arms with torsional beams, as shown in Figure 2-7. The geometry of the torsional beam is 1200 μm (L) \times 20 μm (W) \times 5 μm (H) in our design. The design principle of the torsional beam is the same as that of the 45° mirror. The maximum shear stress in the 135° structures at angle of twist $\theta = 150^\circ$ must be smaller than 2 GPa. According to the calculation, the length must be larger than 846 μm when the width and height are 20 μm and 5 μm , respectively. The reflective surface is the front side of the device layer, so it can be used to fabricate other reflective optical devices by patterning the device layer of SOI wafer. The fabrication process of the 135° structure is the same as the 30°, 45°, and 60° devices but the assembly process is different.

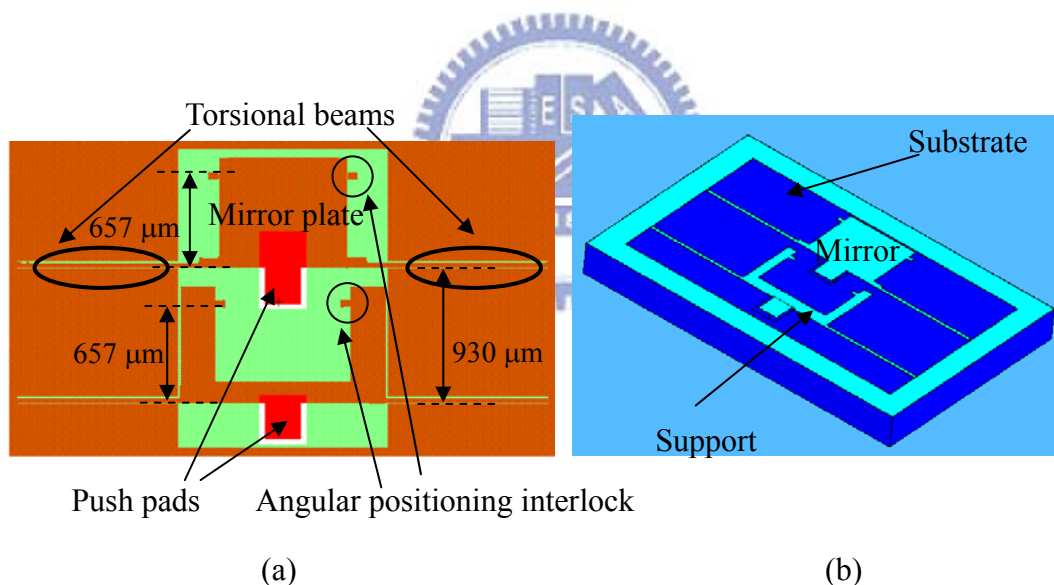


Figure 2-7 (a) Layout design of 135° device, (b) 3-D model.

The assembly process of the 135° device is shown in Figure 2-8. Two probes are needed in the assembly process. First Probe 1 pushes the mirror plate to about 70° to 90° (Figure 2-8 (a)). Then Probe 2 holds the mirror plate from the back. After the mirror plate is held by Probe 2, Probe 1 is moved from the mirror plate to the push pad of the support (Figure 2-8 (b)). Then Probe 1 pushes the support to over 70°

(Figure 2-8 (c)) and Probe 2 pushes the mirror plate forward to 140° to 150° (Figure 2-8 (d)). Subsequently Probe 1 is removed and the torque from the torsional beams drives the support to lie on the mirror plate (Figure 2-8 (e)). Finally, Probe 2 is removed and the mirror is interlocked by the restoring torque from the mirror plate (Figure 2-8 (f)).

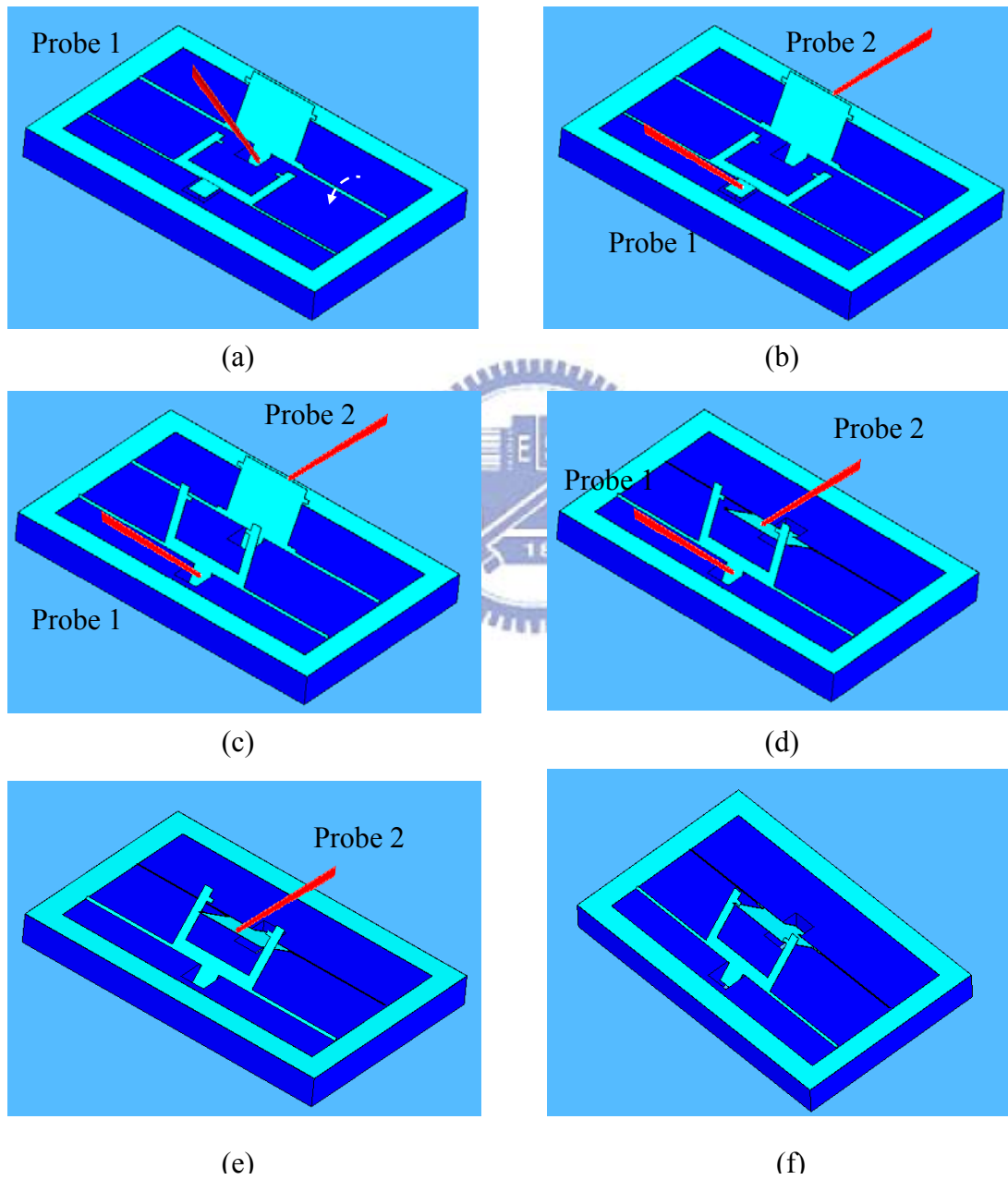


Figure 2-8 Assembly process of the 135° device.

2-3 Optical bench and MEMS-based optical pickup head

The 135° mirror discussed in the previous section is used in an optical bench for a MEMS-based optical pickup head, as shown in Figure 2-9. The optical pickup head is composed of a laser diode, a 135° MEMS mirror, a 135° MEMS mirror with a holographic optical element (HOE) on the reflective surface, an objective lens, and a photodetector. The light emitted from the laser diode is reflected from the parallel to the vertical direction with respect to the disk surface by the 135° MEMS mirror with holographic optical element (HOE) on the surface. The zeroth-order light reflected by the 135° MEMS mirror with HOE is focused on the disk. On the returning path, the first-order light diffracted by the HOE is reflected by another 135° MEMS mirror, and finally projected onto the photodetector. The focusing error signal (FES) can be generated from the HOE diffraction. The simulation of the optical system is discussed below.

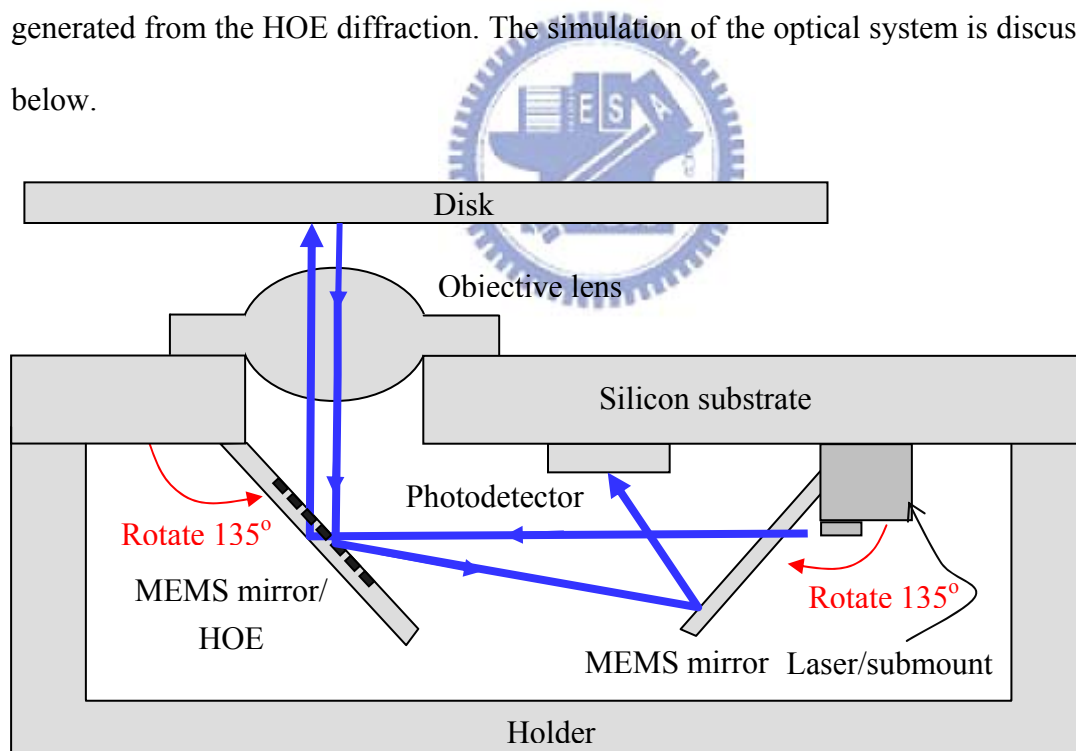


Figure 2-9 Schematic of the MEMS-based optical pickup head.

2-3-1 Simulation of the MEMS-based optical pickup head

Figure 2-10 shows the simulation of the optical pickup head system by Zemax. The wavelength of laser source is 405 nm. The numerical aperture (NA) of the objective lens is 0.65, the focal length is 0.67 mm, and the working distance of is 0.47 mm. The optical spot in forward optical path on the disk can be optimized by ZEMAX so that its size is smaller than the diffraction limit, as shown in Figure 2-11.

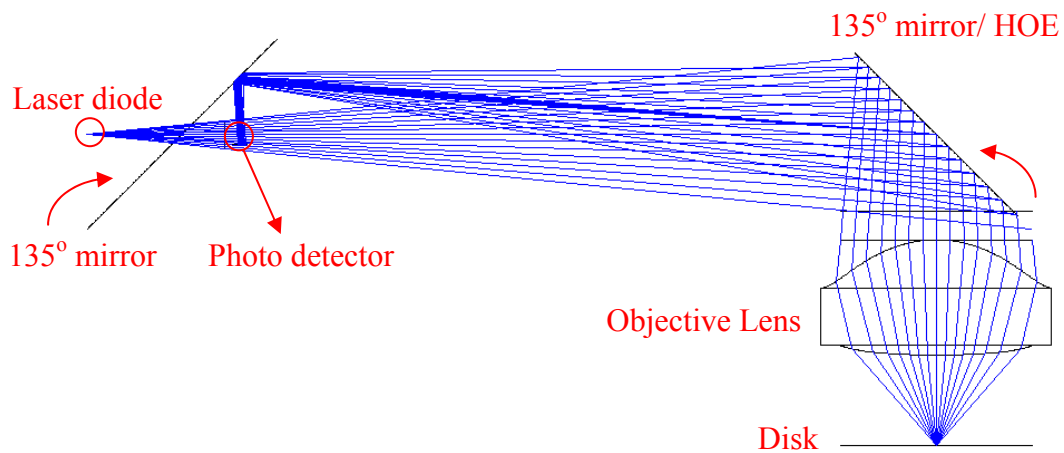


Figure 2-10 Zemax simulation of the MEMS-based optical pickup head.

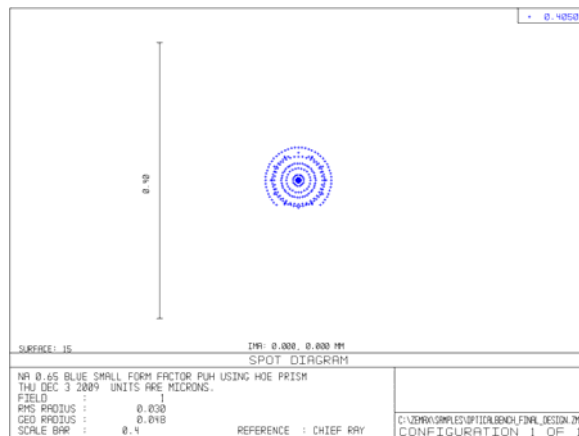


Figure 2-11 Zemax simulated optical spot on the disk.

Holographic optical element [26]

On the returning optical path, the first-order light is diffracted by the astigmatic focusing holographic optical element (HOE) and the light is reflected onto the photodetector by another 135° MEMS mirror. The HOE pattern can be designed as a phase-type binary optical element with the phase polynomial represented by

$$\phi(x, y) = \sum_{m=0}^M \sum_{n=0}^N C_{mn} x^m y^n \quad (2-6)$$

The design of the HOE phase polynomial is similar to [26]. In the current optical pickup head system,

$$\begin{aligned} \phi(x, y) = & -2197x + 705y + 96.64989x^2 + 524.26125xy - 27.601696y^2 \\ & + 64.301924x^3 - 24.624489x^2y - 45.460183xy^2 + 0.324068y^3 \end{aligned} \quad (2-7)$$

where the x term and y term represent the diffraction angle in the x -direction and y -direction, respectively. The x^2 term, xy term, and y^2 term are related to the focus and astigmatism of the beam; the x^2 term and y^2 term represent the focusing capability in the x -direction and y -direction, respectively. The other higher order terms are used for correcting the spherical aberration, coma, and high-order aberrations. By designing these terms of the phase polynomial properly, the optical spot projected on the photodetector will change sharp depending on whether the optical path is in focus or out of focus. Figure 2-12 shows the optical spot on the photodetector when the optical path has a defocus from -10 μm to +10 μm . Astigmatic aberration can be observed in the diffracted out-of-focus spots.

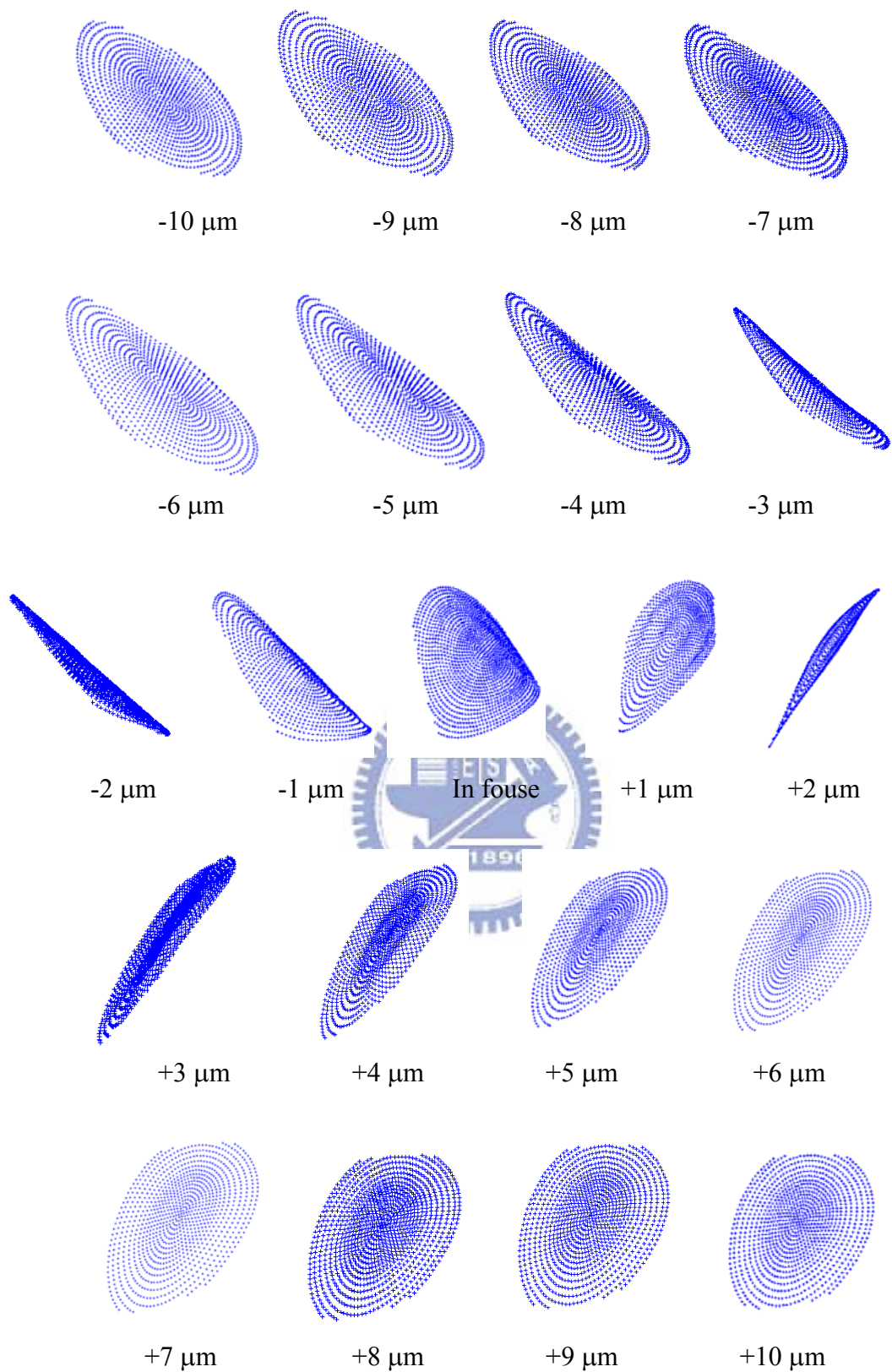


Figure 2-12 Simulated optical spot on the photodetector with various amount of defocus.

S-curve

In order to read the information on the disk, the optical spot must be focused on the disk accurately. Therefore, focusing servo control is necessary in optical pickup head system. The focusing error signals can be generated from photodetector and used as feedback signals to the actuator. The actuator can keep the system in focus by changing the position of the objective lens. Figure 2-13 shows the schematic of the astigmatic method for generating the focus error signal. Figure 2-12 (a) shows optical spot projected onto the quad photodetector when the system is in focus. The size of a photodetector element is $(47.5 \mu\text{m})^2$. Figures 2-13 (b) and (c) show the optical spot projected onto the quad photodetector when the system is defocused in opposite directions. The focusing error signal can be calculated from the light intensity on the photodetectors by using Equation 2-8.

$$\text{FES} = (A+C) - (B+D) \quad (2-8)$$

When the optical spot is in focus on the disk, the light intensity on each photodetector is equal ($A=B=C=D$) and the FES is zero (Figure 2-13 (a)). But when the optical spot is not in focus, the light intensity on the photodetector is not equal and the FES is either positive or negative (Figure 2-13 (b), (c)). The relation between the FES and the defocus distance is the S-curve of this optical pickup head system. Figure 2-14 shows the simulation result of the S-curve in this system. The linear region of the FES is about $5 \mu\text{m}$.

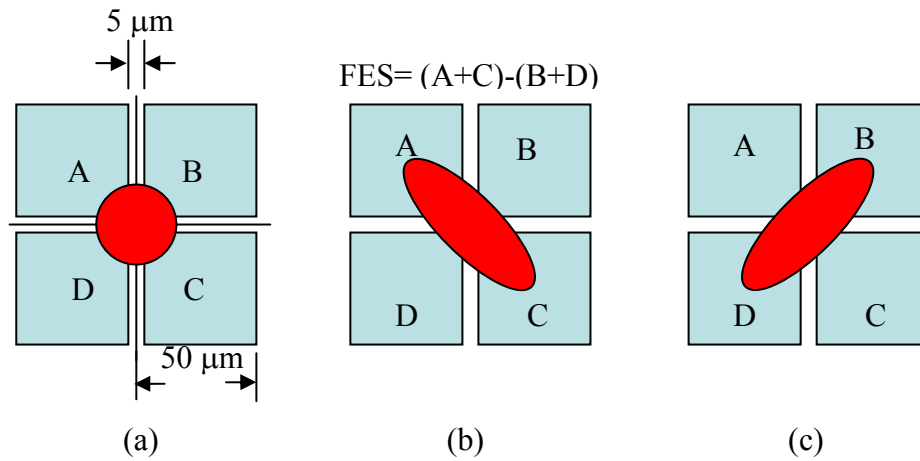


Figure 2-13 Schematic of the astigmatic method.

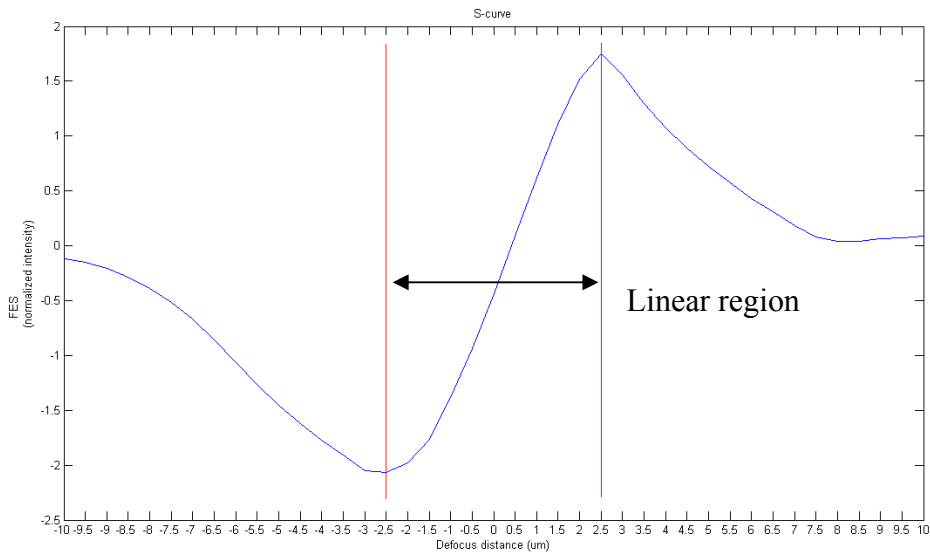


Figure 2-14 Simulation of the S-curve.

2-3-2 Diffractive efficiency of HOE

On the forward path, the zeroth-order light reflected from the HOE is focused on the disk. On the returning path, the first-order light diffracted by the HOE is reflected by another 135° MEMS mirror and finally projected on the photodetector. The light intensity is reduced due to the reflection and diffraction. Since the power loss due to reflection is much smaller than that due to diffraction, only the diffraction efficiency of the HOE is discussed in this section.

Figure 2-15 shows the schematic of the light wave passing through a diffractive optical element. In the scalar diffraction theory, the incident distribution of optical field on the diffractive optical element can be expressed as

$$g_0(u, v) = A(u, v)e^{i\phi(u, v)} \quad (2-9)$$

where u and v represent the position on the diffractive optical element, A and ϕ represent the amplitude and phase functions, respectively. After the light wave passes through the diffractive optical element, the distribution of the optical field is modified as

$$g(u, v) = A(u, v)e^{i\phi(u, v)}t(u, v) \quad (2-10)$$

where t represents the transmission function and can be expressed as

$$t(u, v) = A'(u, v)e^{i\phi'(u, v)} \quad (2-11)$$

The distribution of the optical field on the image plane can be expressed as Equation 2-12 from the Huygens-Fresnel principle [27]

$$U(\zeta, \eta) = \frac{z}{i\lambda} \iint_{\Sigma} U(u, v) \frac{e^{ikr}}{r^2} dudv \quad (2-12)$$

where z is the distance between the diffractive optical element and the image plane. Equation 2-12 can be reduced to Equation 2-13 by the Fraunhofer approximation when z is larger than the area of diffractive optical element. It is also called the far-field diffraction.

$$U(\zeta, \eta) = \frac{e^{ik(z + \frac{u^2 + v^2}{2z})}}{i\lambda z} \int \int_{-\infty}^{\infty} U(u, v) e^{-i\frac{2\pi}{\lambda z}(\zeta u + \eta v)} dudv \quad (2-13)$$

From Equation 2-13, the distribution of the optical field on the (ζ, η) plane is the Fourier transform of the distribution of optical field on the (u, v) plane.

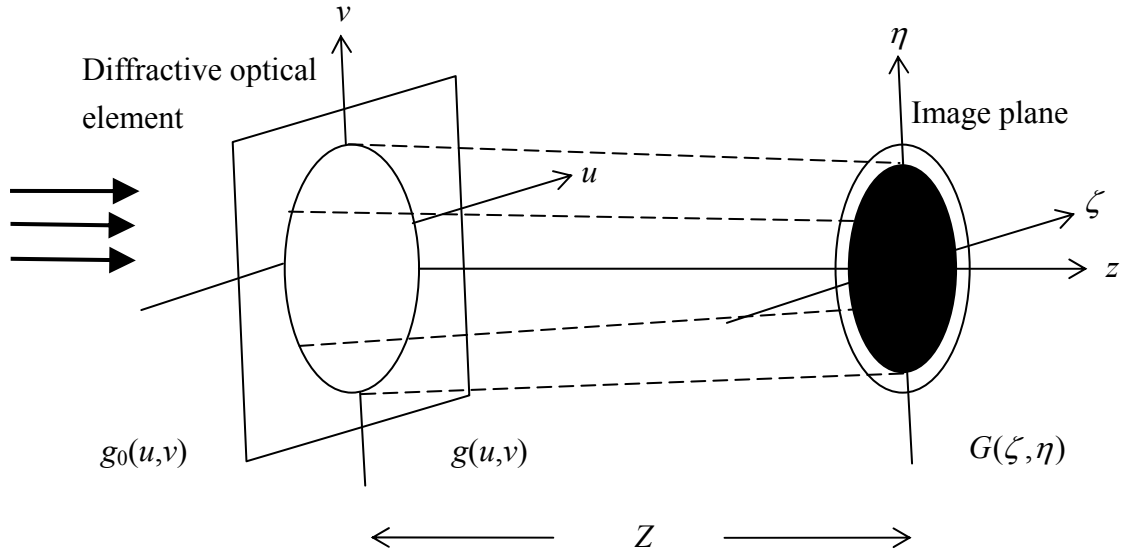


Figure 2-15 Schematic of diffraction theory.

Figure 2-16 shows the schematic and phase distribution of the reflective linear phase grating. The depth and the period of the grating are d and T , respectively. The light wave is perpendicularly incident on the grating and then reflected to the image plane. The optical path difference of this grating is equal to $2d$ (Figure 2-16 (a)). Therefore, the transmission function of the grating can be expressed as Equation 2-14 (Figure 2-16 (b)), where ϕ represent the phase difference and can be expressed as a function of the optical path difference, as shown in Equation 2-15.

$$f(x) = \begin{cases} 1 & -\frac{T}{2} < x < \frac{S}{2} \\ e^{i\phi} & -\frac{S}{2} < x < \frac{S}{2} \\ 1 & \frac{S}{2} < x < \frac{T}{2} \end{cases} \quad (2-14)$$

$$\phi = \frac{2\pi}{\lambda} \cdot (\text{optical path difference}) \quad (2-15)$$

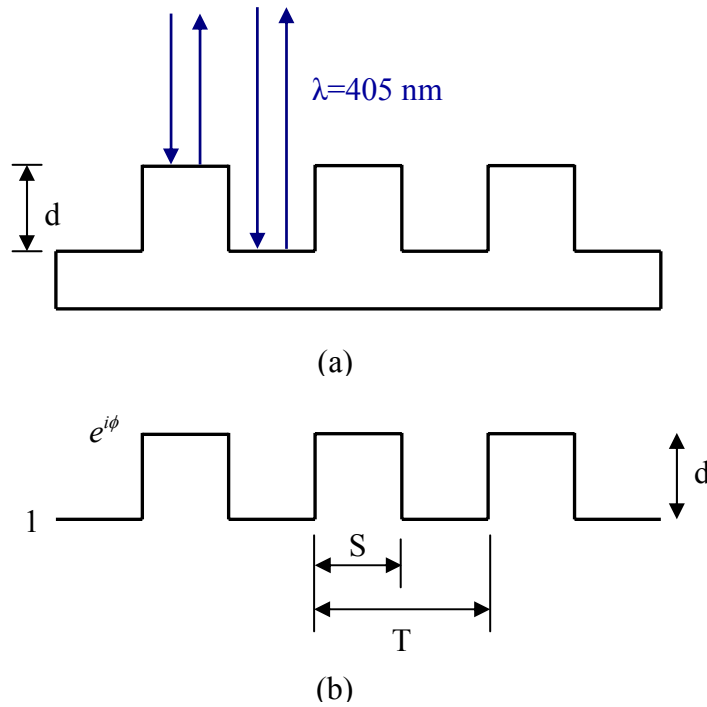


Figure 2-16 (a) Schematic and (b) phase distribution of the reflective linear phase grating.

As in the scalar diffraction theory discussed above, the diffraction efficiency of the linear grating can be calculated by Fourier transform. In our design, the efficiency of the HOE can be calculated as a reflective phase grating. Since the HOE is patterned on the 135° mirror, the optical path difference is $2\sqrt{2}d$ in our design, as shown in Figure 2-17. When the optical path difference $2\sqrt{2}d$ is substituted in Equation 2-15, the diffraction efficiency of this system can be calculated by the Fourier transform of $f(x)$ in Equation 2-14. Because of the periodicity, the transmission function can be expanded as a Fourier series. The Fourier coefficients a_m and b_m give the values of the amplitudes in each diffraction orders. First-order and zeroth-order beams are used in our design, so only a_0, a_1, b_1 are calculated below.

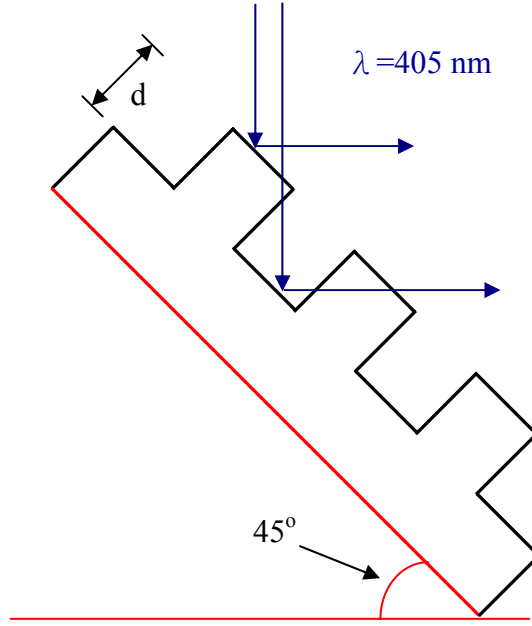


Figure 2-17 Schematic of the reflective type linear phase grating on 135° mirror.

$$f(x) = \frac{a_0}{2} + \sum_{m=1}^{\infty} a_m \cos\left(\frac{2\pi mx}{T}\right) + \sum_{m=1}^{\infty} b_m \cos\left(\frac{2\pi mx}{T}\right)$$

$$a_0 = \frac{1}{T} \int_{-T/2}^{T/2} f(x) dx = \frac{1}{T} \left[\int_{-T/2}^{-S/2} 1 dx + \int_{-S/2}^{S/2} e^{j\phi} dx + \int_{S/2}^{T/2} 1 dx \right]$$

$$= 1 - \frac{S}{T} + \frac{S}{T} \cdot e^{j\phi}$$

$$a_m = \frac{1}{T} \int_{-T/2}^{T/2} f(x) \cos\left(\frac{2m\pi x}{T}\right) dx = \frac{1}{T} \left[\int_{-T/2}^{-S/2} \cos\left(\frac{2m\pi x}{T}\right) dx + \int_{-S/2}^{S/2} e^{j\phi} \cos\left(\frac{2m\pi x}{T}\right) dx + \int_{S/2}^{T/2} \cos\left(\frac{2m\pi x}{T}\right) dx \right]$$

$$= \frac{T}{2m\pi} \left[2 \sin m\pi - 2 \sin \frac{m\pi S}{T} + 2e^{j\phi} \cdot \sin \frac{m\pi S}{T} \right]$$

$$b_m = \frac{1}{T} \int_{-T/2}^{T/2} f(x) \sin\left(\frac{2m\pi x}{T}\right) dx = \frac{1}{T} \left[\int_{-T/2}^{-S/2} \sin\left(\frac{2m\pi x}{T}\right) dx + \int_{-S/2}^{S/2} e^{j\phi} \sin\left(\frac{2m\pi x}{T}\right) dx + \int_{S/2}^{T/2} \sin\left(\frac{2m\pi x}{T}\right) dx \right]$$

$$= 0$$

Because the duty cycle of the HOE is 0.5 in our design, $S/T=0.5$ and

$$\begin{cases} a_0 = 0.5(e^{j\phi} + 1) \\ a_1 = \frac{1}{\pi}(e^{j\phi} - 1) & a_0 = 0.5(e^{j\phi} + 1) \\ b_1 = 0 \end{cases} \quad (2-16)$$

The coefficients a_0 , a_1 , b_1 represent the amplitude of the zeroth-order and first-order beams, respectively. The intensity of light is equal to the square of the amplitude, so the diffraction efficiency of the zeroth-order and first-order light can be calculated as

$$\eta_0 = |a_0|^2 = \left| \frac{1}{2} \left(1 + e^{\frac{j4\sqrt{2}\pi d}{\lambda}} \right) \right|^2$$

$$\eta_1 = |a_1|^2 = \left| \frac{1}{\pi} (e^{j\phi} - 1) \right|^2 = \left| \frac{1}{\pi} \left(e^{\frac{j4\sqrt{2}\pi d}{\lambda}} - 1 \right) \right|^2 \quad (2-17)$$

Figure 2-18 shows the calculated diffraction efficiency. Because the optical pickup head uses zeroth-order diffraction on the forward path and first-order diffraction on the return path, the total efficiency is equal to the product of the two efficiencies, as shown in Figure 2-18. Therefore, to get the maximum power on the photodetector, the optimum etching depth of the HOE is odd multiples of 36.2 nm.

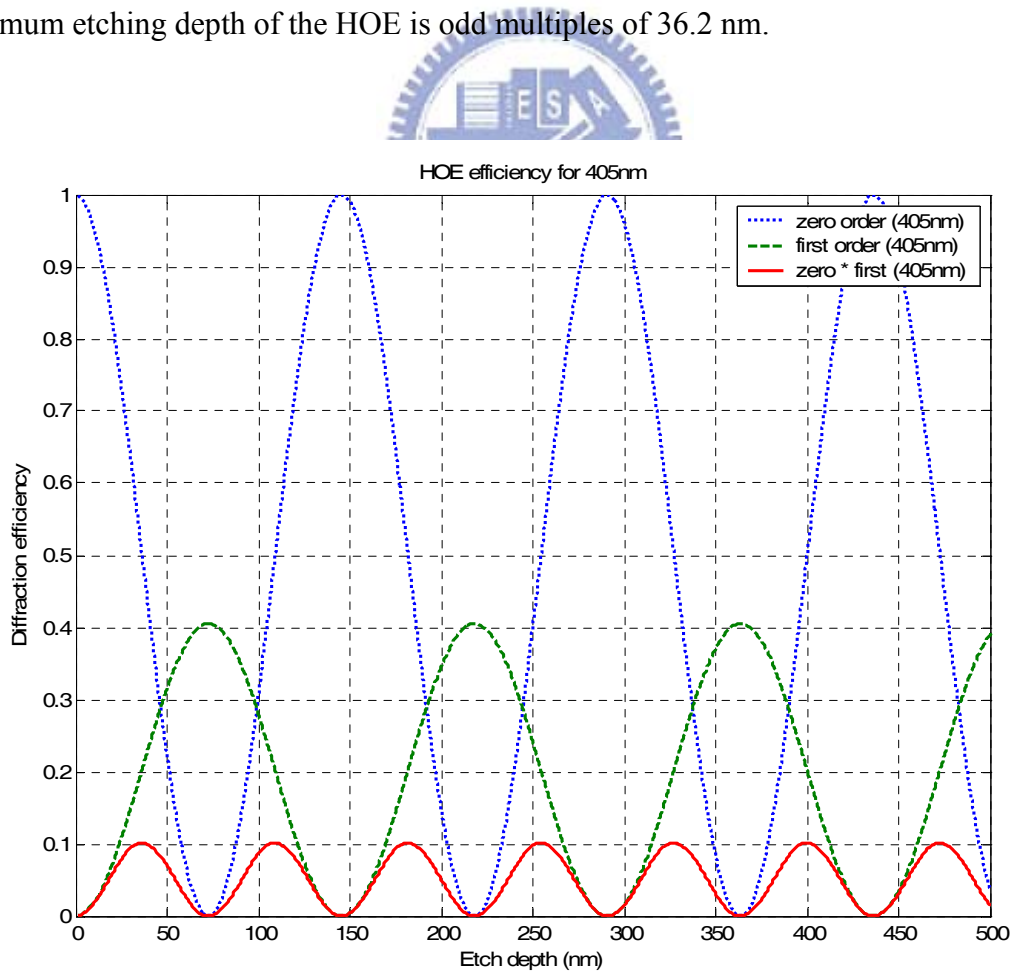


Figure 2-18 Calculation of diffraction efficiency.

2-3-3 Layout design

In the layout of the optical bench, the positions of the components, including the photodetector, the objective lens, the laser source, the distance between two 135° MEMS mirror, and the reflective area on the 135° MEMS mirror without HOE, must match the optical system in the simulation. The HOE pattern is generated by the phase polynomial. The layout design of the optical bench is discussed in this section.

HOE pattern

The pattern of the HOE is shown in Figure 2-19. The pattern is generated by the phase polynomial in Equation 2-6. The duty cycle and width of the HOE are 0.5 and 1.3 μm ($1.36 \mu\text{m} \times \cos 17.8^\circ$), respectively. The pattern of the HOE has an angle of 72.2°, as can be calculated from the phase polynomial shown in Equation 2-7. The x term and y term represent the diffraction direction in the x -direction and y -direction, respectively. So the diffraction direction of the HOE is

$$\theta = \tan^{-1}\left(\frac{\text{coefficient of the } y \text{ term}}{\text{coefficient of the } x \text{ term}}\right) = \tan^{-1}\left(\frac{705}{2197}\right) = 17.8^\circ \quad (2-18)$$

where the 705 and 2197 are the coefficients of the x term and y term from Equation 2-7. In order to realize the astigmatic method for focusing error signals, the diffracted optical spot must be projected to the center of the quad photodetector elements. The diffraction direction of 17.8° is designed to match this condition. Therefore, the HOE is patterned at the complement angle of the diffraction direction of 72.2°.

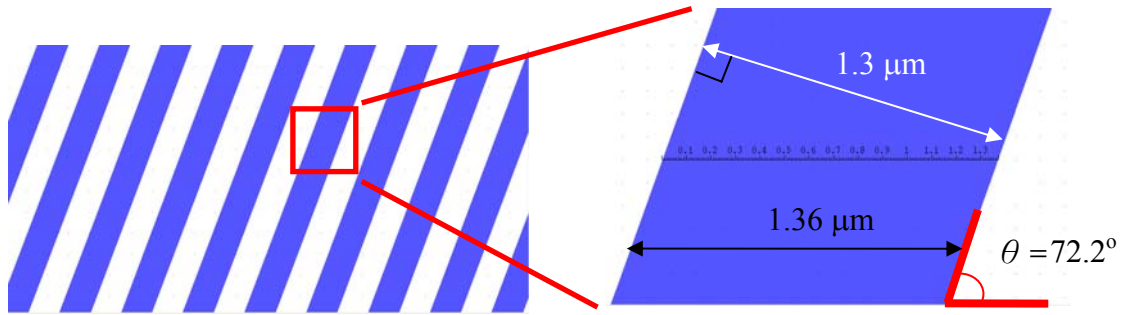


Figure 2-19 Layout of the holographic optical element.

Optical path

Figure 2-20 shows the schematic of the optical bench after assembly. Figure 2-21 shows the side-view and top-view of the optical path. The distance between the rotation axes of the two 135° MEMS mirror is $4934 \mu\text{m}$. The center of the quad photodetector has a distance of $711 \mu\text{m}$ from the rotational axis of M1 in the x -direction and a distance of $571 \mu\text{m}$ from the optical axis of the forward path in the y -direction. The reflective region of M1 in Figure 2-21 (a) has a distance of $991 \mu\text{m}$ from the rotational axis in the x -direction before the 135° mirror is assembled. Finally, the completed layout of optical bench is shown in Figure 2-22. The tolerance of the 135° devices are simulated as 1° [28].

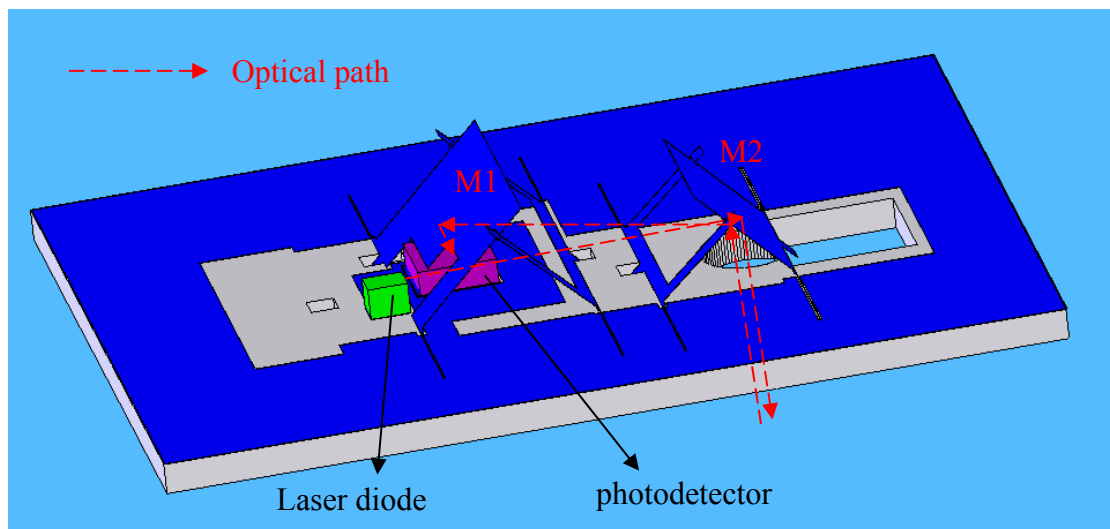
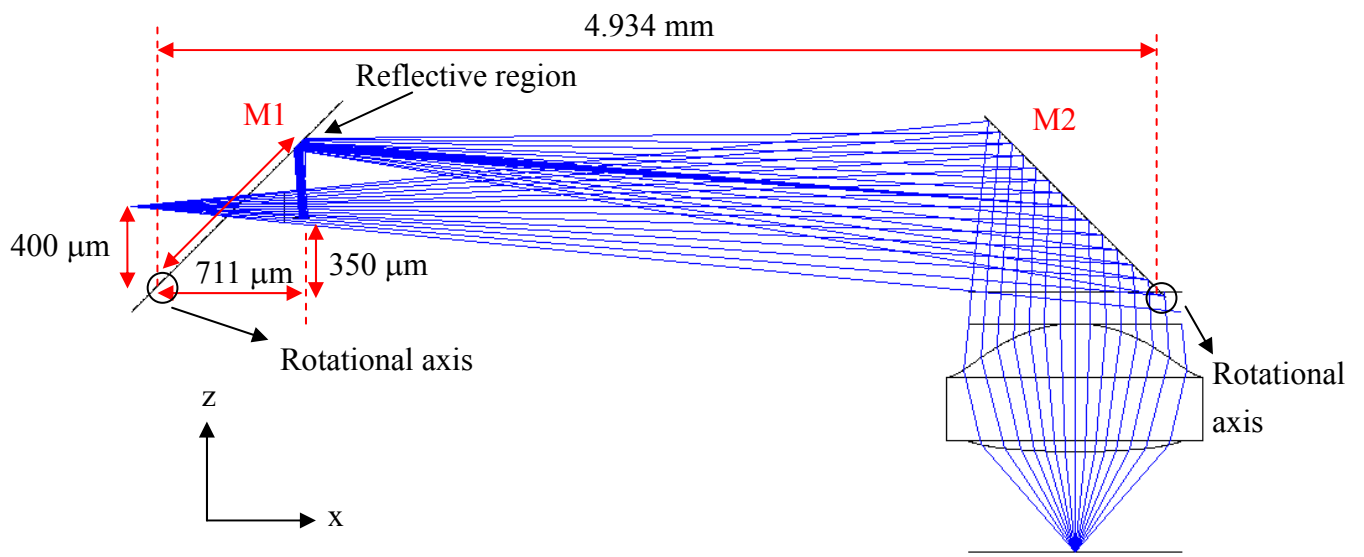
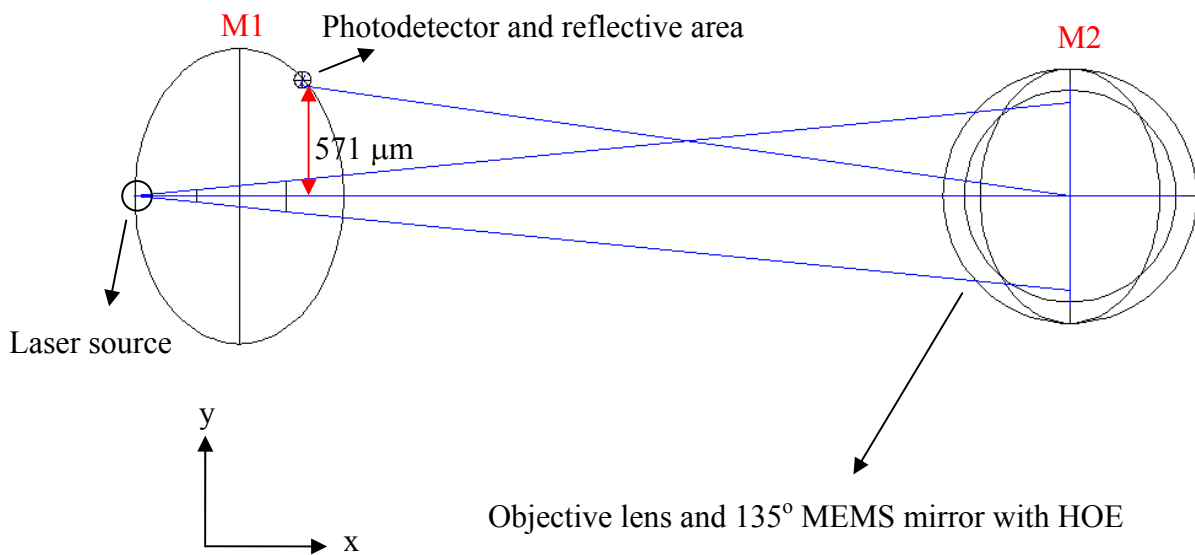


Figure 2-20 Schematic of the optical bench after assembly.



(a)



(b)

Figure 2-21 Optical simulation of the system, (a) side-view, (b) top-view.

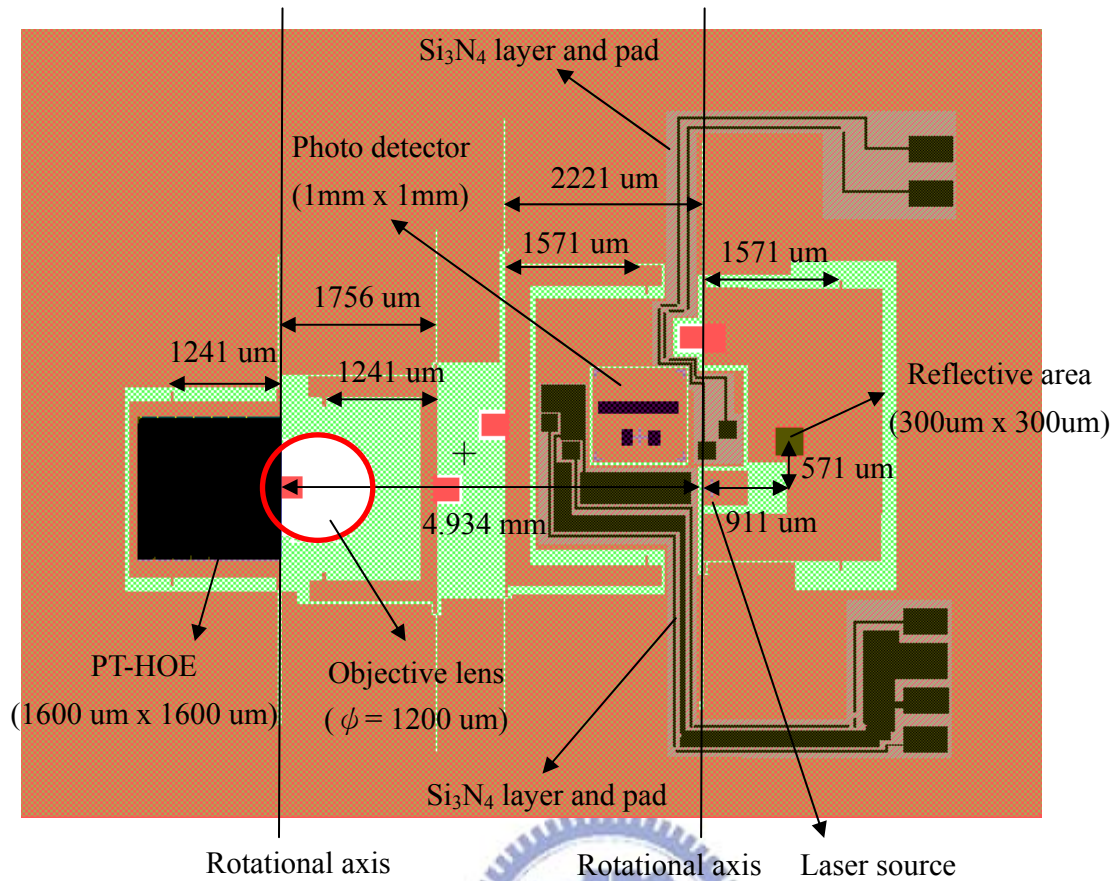


Figure 2-22 Layout of optical bench.

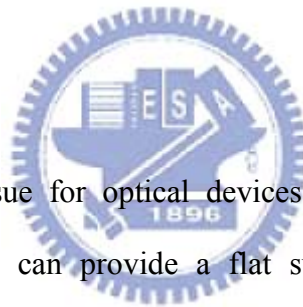
2-4 Summary

Mirrors with four different angles are designed to demonstrate the assembly method for arbitrary angles. Different dimensions of torsional beams and locking mechanism are used to test the angular positioning accuracy. The optical bench is designed to realize the optical pickup head. In Chapter 3, the fabrication is discussed.

Chapter 3 Fabrication Process

The optical pick up head system was fabricated in SOI wafers. It includes holographic-optical-elements (HOE), 135° reflective mirrors, objective lenses, and photodetectors. SOI wafers are used due to the surface flatness. Using SOI wafers also can simplify the process flow. The HOE and 135° reflective mirrors are made in the device layers of the SOI wafers. The objective lens and photodetectors are bonded on the fabricated chip. The fabrication process of the pre-assembly optical bench is discussed in the first part of this chapter. The second part discusses the assembly process of this optical pickup head system. Finally, some phenomena and encountered problems will be discussed.

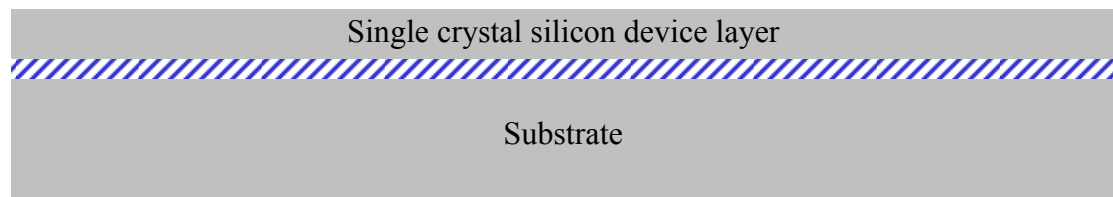
3-1 Fabrication process



Flatness is an important issue for optical devices. Since single-crystal-silicon (SCS) almost has no stress, it can provide a flat surface for optical purposes. Therefore, the basic structures of the optical bench are defined in the device layer of the SOI wafer, including the holographic-optical-element (HOE) and the 135° reflective mirrors. In this process, silicon nitride is an isolation layer for conducting wires; silicon oxide is a sacrificial layer. Gold is used for conductive wires and reflective mirrors. Figure 3-1 is the cross-section of the fabrication process. The detailed process flow and parameters are discussed in the following sections.

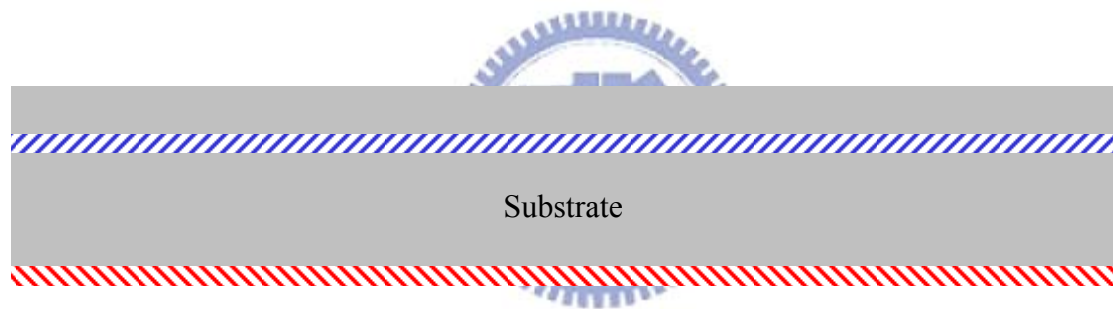
Process flow

The fabrication process of this device is shown in Figure 3-1. The device was mainly fabricated in the Nano Facility Center at National Chiao Tung University. The SOI wafers have a device layer of 5 μm , a buried oxide layer of 2 μm , and a handle layer of 400 μm .



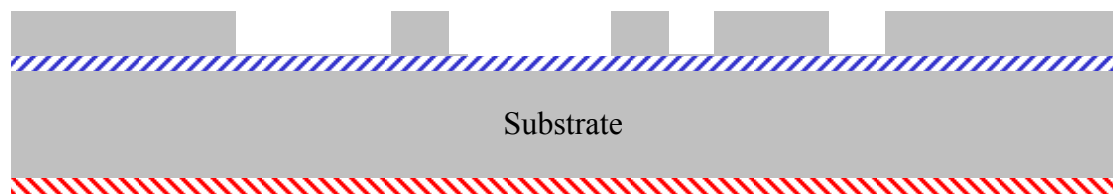
 Buried oxide

(a) RCA cleaning (Step A)



 Buried oxide  PECVD Oxide

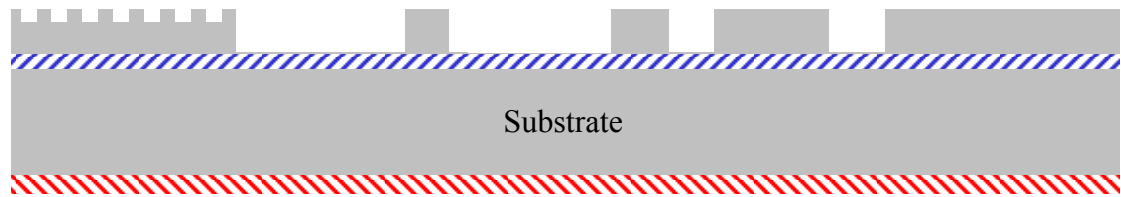
(b) Front side patterning (Step B, Step C)



 Buried oxide  PECVD Oxide

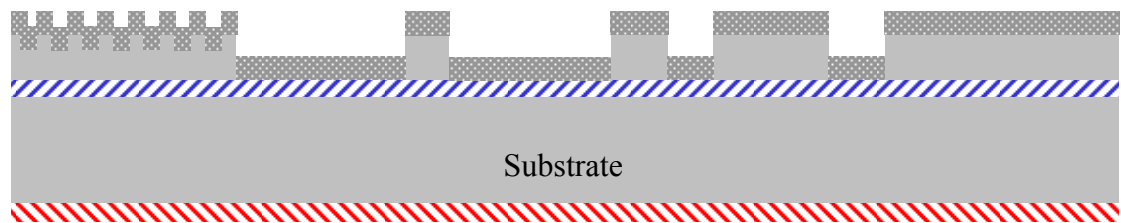
(c) Backside oxide deposition (Step D)

Figure 3-1 Fabrication process.



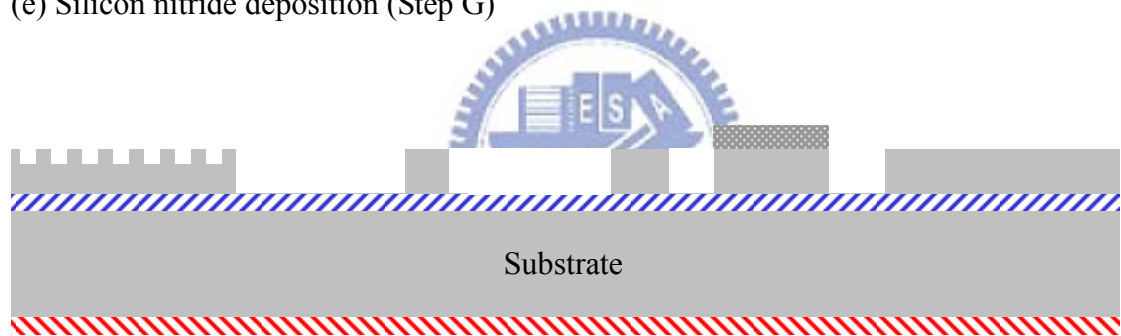
▨ Buried oxide ▨ PECVD Oxide

(d) HOE definition (Step E, Step F)



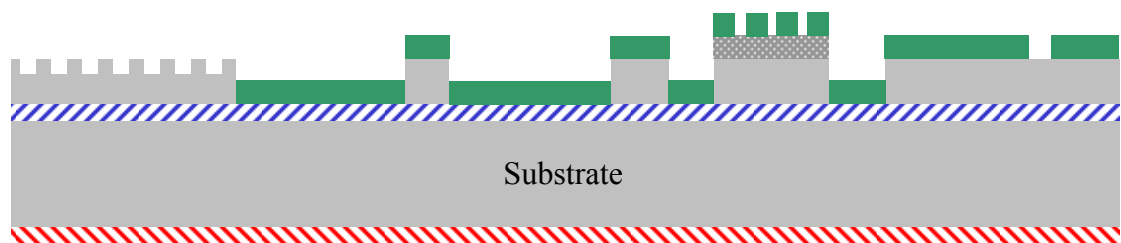
▨ Buried oxide ▨ PECVD Oxide Si_3N_4

(e) Silicon nitride deposition (Step G)



▨ Buried oxide ▨ PECVD Oxide Si_3N_4

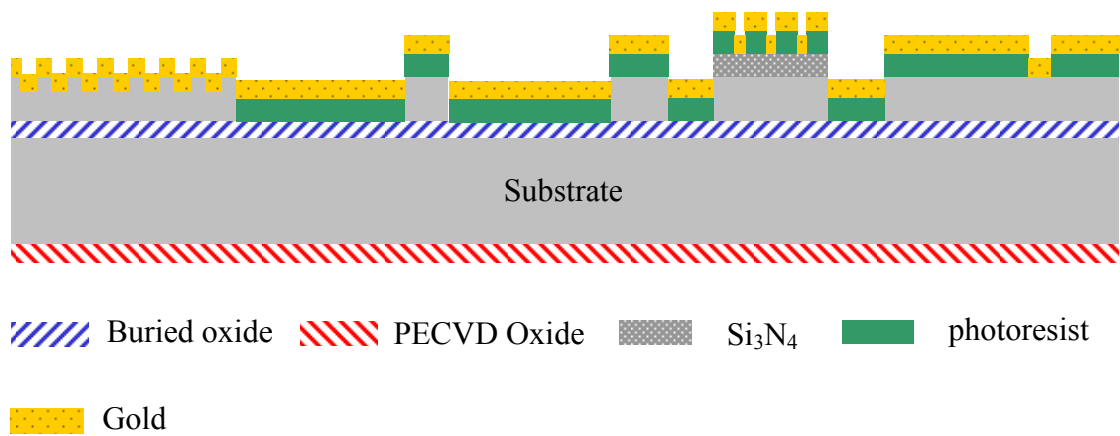
(e) Silicon nitride definition (Step H, Step I)



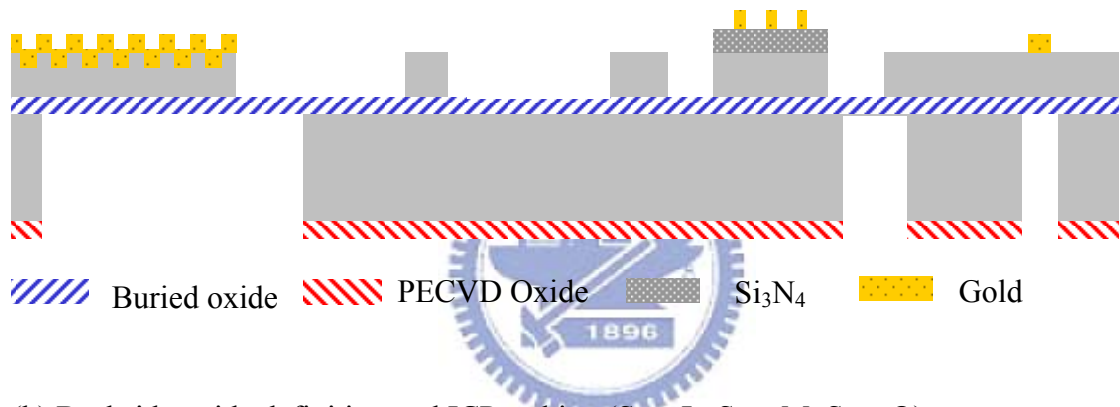
▨ Buried oxide ▨ PECVD Oxide Si_3N_4 photoresist

(f) Gold pattern definition (Step J)

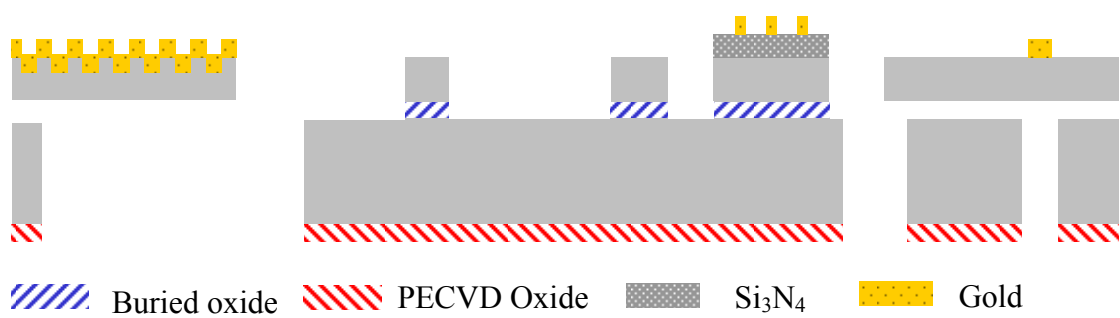
Figure 3-1 Fabrication process (continued).



(g) Gold deposition and lift-off (Step K)



(h) Backside oxide definition and ICP etching (Step L, Step M, Step O)



(i) Oxide release (Step P)

Figure 3-1 Fabrication process (continued).

Step A: RCA cleaning

A standard RCA clean process was first performed to remove organic contaminants, native oxide and ionic contamination on the surface of the wafer. Detailed parameters are shown below. In order to avoid the etching of buried oxide in the SOI wafer, the chemical oxide removal process using HF is reduced to 30s. Between etch step is de-ionized water rinse.

Step	Parameters
0	D. I. water Rinse (5 min)
1	$\text{H}_2\text{SO}_4 : \text{H}_2\text{O}_2 = 3 : 1$ (10~15 min, 75 °C ~85 °C)
2	$\text{HF} : \text{H}_2\text{O} = 1 : 100$ (30 sec, room temperature)
3	$\text{NH}_4\text{OH} : \text{H}_2\text{O}_2 : \text{H}_2\text{O} = 1 : 4 : 20$ (10~15 min, 75 °C ~85 °C)
4	$\text{HCL} : \text{H}_2\text{O}_2 : \text{H}_2\text{O} = 1 : 1 : 6$ (10~15 min 75 °C ~85 °C)
5	$\text{HF} : \text{H}_2\text{O} = 1 : 100$ (30 sec, room temperature)

Step B: Photolithography – Device layer definition (Mask1)

Mask1 defines the main structure of the optical bench in the 5- μm -thick layer. The SCS layer was etched by inductively-coupled plasma (ICP). FH6400 positive photoresist was used as the mask material. The selectivity between silicon and the FH6400 photoresist is about 1:40 in the ICP process.. Detailed parameters are listed as below.

Step	Description	Parameters
0	Photoresist	FH6400
1	HMDS coating	Vapor prime oven
2	Coating (spread cycle)	1000 rpm 10 sec
	Coating (spin cycle)	2000 rpm 35 sec
3	Soft bake	90 °C hotplate 150 sec
4	Exposure	Karl Suss MJB-3 mask aligner (3.2 mW/cm ²) for 90 sec

5	Development	Developer FHD-5 for 90 sec
6	Rinse	D.I. water 1 min
7	Hard bake	120 °C hotplate 30 min

Step C: Inductively-coupled plasma silicon etching

Inductively-coupled plasma (ICP) is used to anisotropically etch the 5- μm -thick silicon device layer of the SOI wafer. The ICP process is performed by the ICP etching service of the Instrument Technology Research Center (ITRC) or National Taiwan University (NTU). The parameters of the ICP etching at NTU are listed below.

Description	Etch phase parameters	Passivation phase parameters
Time per cycle	11.5 seconds	7.0 seconds
SF ₆ flow rate	130 sccm	0 sccm
C ₄ F ₈ flow rate	0 sccm	85 sccm
O ₂ flow rate	13 sccm	0 sccm
Coil RF power	600 W	600 W
Platen RF power	11.5 W	0 W
Process pressure	APC position = 81.2 % Base pressure = 0.3 mtorr	
Helium backside cooling	Helium backside pressure = 10 Torr Maximum helium leak up rate = 20 mTorr/min	
Etch rate	0.6-0.7 μm per cycle depending on pattern	

Step D: Backside silicon oxide deposition

Plasma-enhanced chemical vapor deposition (PECVD) was utilized to deposit a 4- μm -thick silicon oxide layer on the backside of the handle layer. The oxide layer will be used as a hard mask for the backside silicon etching process. The selectivity between the oxide and the silicon in the ICP process is 1:90.

Description	Parameters
SiH ₄ flow rate	5 sccm
N ₂ O flow rate	90 sccm

Process pressure	400 mTorr
Process temperature	350° C
RF power	11 W
Deposition time	Two 35-minute deposition for 2.25 μm each

Step E: Photolithography – holographic optical element (HOE) definition (Mask 2)

Mask2 is used to define the pattern of the holographic optical element (HOE) on the device layer of the SOI wafer. FH6400 photoresist was used as the RIE mask and the selectivity between silicon and FH6400 photoresist is about 1:2 in the RIE process. Therefore, 0.7-μm-thick photoresist is coated on the wafer in this step.

Step	Description	Parameters
0	Photoresist	FH6400
1	HMDS coating	Vapor prime oven
2	Coating (spread cycle)	1000 rpm 10 sec
	Coating (spin cycle)	3000 rpm 30 sec
3	Soft bake	90 °C hotplate 90 sec
4	Exposure	Karl Suss MJB-3 mask aligner (3.2 mW/cm ²) for 60 sec
5	Development	Developer FHD-5 for 60 sec
6	Rinse	D.I. water 1 min
7	Hard bake	120° C hotplate 10 min

Step F: Polysilicon reactive ion etching (Poly-Si RIE) – Silicon etching

The HOE pattern on the device layer in step E is etched by RIE (SAMCO RIE-10N). The etching depth was 253.4 nm according to the theoretical calculation of diffraction efficiency in Chapter 2. Detailed parameters are listed as below.

Description	Parameters
SF ₆ flow rate	20 sccm
CHF ₃ flow rate	8 sccm

Helium backside cooling	about 15 sccm
Process pressure	20 mTorr
RF power	100 W
Etch rate	10 min for 1 μm silicon

Step G: Front side silicon nitride deposition

A 5000 Å silicon nitride layer was deposited as an isolation layer for conducting wires by Low Pressure Chemical Vapor Deposition (LPCVD). Before depositing the low stress silicon nitride, the SOI wafer was dipped in buffered oxide etch (BOE) solution for 10 second to remove the native oxide on the device layer. Detailed parameters of LPCVD nitride deposition are listed as below.

Description	Parameters
NH ₃ flow rate	17 sccm
SiHCl ₂ flow rate	85 sccm
Process pressure	180 mTorr
Process temperature	850 °C
Deposition time	10 minuate deposition for 0.1 μm

Step H: Photolithography – Silicon nitride definition (Mask 3)

The silicon nitride is defined with Mask 3 in FH6400 positive photoresist. The 5000-Å-thick silicon nitride layer on the device layer is then etched using a RIE etcher. The selectivity between silicon and FH6400 photoresist is about 1:2 in the next RIE process. Therefore, 2- μm -thick photoresist is coated in this step.

Step	Description	Parameters
0	Photoresist	FH6400
1	HMDS coating	Vapor prime oven
2	Coating (spread cycle)	1000 rpm 10 sec
	Coating (spin cycle)	2000 rpm 35 sec

3	Soft bake	90 °C hotplate 150 second
4	Exposure	Karl Suss MJB-3 mask aligner (3.2 mW/cm ²) for 90 sec
5	Development	Developer FHD-5 for 90second
6	Rinse	D.I. water 1 min
7	Hard bake	120 °C hotplate 30 min

Step I: Polysilicon reactive ion etching (Poly-Si RIE) – LPCVD nitride etching

The silicon nitride window exposed in step H is etched by RIE (SAMCO RIE-10N). The 5000-Å-thick silicon nitride layer in the area of conducting wires is removed in this step. Detailed parameters of are listed as below.

Description	Parameters
SF ₆ flow rate	20 sccm
O ₂ flow rate	8 sccm
Helium backside cooling	about 15 sccm
Process pressure	20 mTorr
RF power	100 W
Etch rate	1 min for 1000 Å silicon

Step J: Photolithography – Pad and reflective area definition (Mask 4)

This step defines the conducting wires and reflective area for the next lift-off process. The essential factors of the lift-process are the hard bake of the photoresist and the cleanness of the wafer. The photoresist can be hardly lifted off in the next lift-off process if the photoresist is hard baked; the dirty wafer surface will affect the adhesion of the metal deposition.

Step	Description	Parameters
0	Photoresist	AZ4620
1	HMDS coating	Vapor prime oven
2	Coating (spread cycle)	1000 rpm 10 sec

	Coating (spin cycle)	2500 rpm 30 sec
3	Soft bake	90 °C hotplate 10 min
4	Exposure	Karl Suss MJB-3 mask aligner (3.2 mW/cm ²) for 420 sec
5	Development	Developer AZ-300 for 4 min 35 sec
6	Rinse	D.I. water 1 min
7	Hard bake	No require

Step K: Metal deposition and lift-off

The 2000-Å-thick gold is deposited by the E-Gun evaporator. Gold is used to resist HF etch in the release process. Before gold is deposited on the front side of the SOI wafers, a 200-Å-thick chromium is first deposited on the surface as the adhesion layer.

Step L: Photolithography – backside silicon oxide pattern (Mask 5)

This step defines the through-wafer holes under the push-pads and the reflective regions without release holes. The oxide deposited in step D is patterned by AZ4620 photoresist. The patterned oxide is used as the hard mask for the later backside ICP etching process. An EV620 double side aligner at Nation Tsing Hua University (NTHU) is used for the photolithography process. The selectivity between PECVD oxide and the AZ4620 is 1:1.8. About 8-µm-thick photoresist is coated in the step.

Step	Description	Parameters
0	Photoresist	AZ4620
1	HMDS coating	Vapor prime oven
2	Coating (spread cycle)	1000 rpm 10 sec
	Coating (spin cycle)	2000 rpm 40 sec
3	Soft bake	90 °C hotplate 27 min
4	Exposure	EV620 mask aligner (10 mW/cm ²) for 12 sec
5	Development	Developer for 1 min 15 sec

6	Rinse	D.I. water 1 min
7	Hard bake	120 °C hotplate 60 min

Step M: Polysilicon reactive ion etching (Poly-Si RIE) – Backside oxide etching

The patterned oxide in step L is then etched by RIE. The PECVD oxide needs to be completely removed on the backside of the handle wafer. Detailed parameters are listed as below.

Description	Parameters
SF ₆ flow rate	30 sccm
CHF ₃ flow rate	10 sccm
Helium backside cooling	about 15 sccm
Process pressure	50 mtorr
RF power	100 W
Etch rate	18 min for 2 μm PECVD oxide



Step N: Wafer dicing

The wafer is then diced into individual device chips. Since the subsequent ICP etching depth is close to the entire thickness of the whole wafer, only chips are used to reduce the risk of breaking the whole wafer in the ICP chamber.

Step O: Backside inductively-coupled-plasma deep silicon etching

The 400-μm-thick handle layer of the SOI wafer is etched by ICP. Silicon oxide is used as hard mask due to the higher selectivity between silicon and silicon oxide compare to that between silicon and photoresist in the ICP process. The diced chips are bonded to a carrier wafer with thermal grease or photoresist. A 5-μm-thick silicon oxide is deposited on the carrier wafer as the shield for the ICP process. The 400-μm-thick substrate is then etched. The identical etching parameters as in Step C are used in this step.

Step P: Device release

The final step in the fabrication process is to release the microstructure from the sacrificial oxide layer. The step is very important since the large mirror plate can easily stick to the substrate in the conventional releasing process with HF solution. Vapor HF release technique is used as the method to solve the problem of stiction since no subsequent water rinse is needed [29].

Figure 3-2 schematically illustrates the apparatus of the vapor HF process. The apparatus consists of two Teflon dishes, one plastic film, and one light bulb. The chip is placed on the plastic film with holes to ensure the HF vapor can pass through to the chip. The light bulb is used in order to warm up the sample and to control the temperature during this process. When the temperature of the chip is lower than 30 °C, water condensation can occur on the surface of the sample. The water condensation can still cause the stiction problem. When the temperature of the chip is higher than 40 °C, no water condensation occurs but the etching rate is very slow. So the most important experimental parameter is the temperature of the chip and the suitable range is about 30 °C ~ 40 °C.

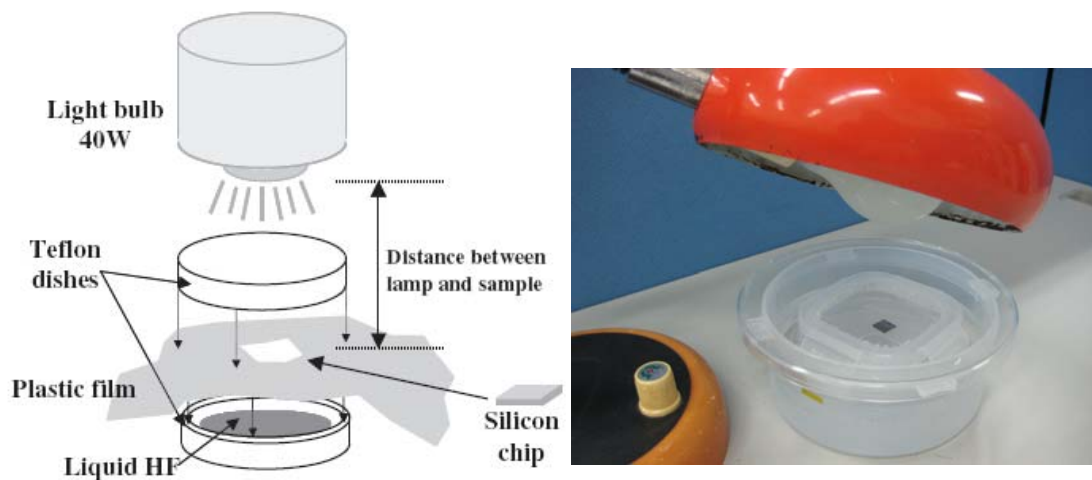


Figure 3-2 Schematic of the vapor HF release setup [29].

3-2 Fabrication issues and solutions

Difficulty in the patterning of silicon nitride and breaking of the large mirror plate after the backside ICP etching occurred in the fabrication. These fabrication problems and their solutions are presented in this section.

3-2-1 Photolithography of Si_3N_4

In step H, the thin Si_3N_4 isolation film was patterned. There were many release holes on the support frames and reflective mirrors. The depth of these release holes was $5\ \mu\text{m}$. When photoresist was spin coated on the wafer, the release holes were filled with photoresist. If a $2\text{-}\mu\text{m}$ -thick FH-6400 photoresist was spin coated on the top surface, the exposure time for the $2\text{-}\mu\text{m}$ -thick photoresist was not enough to expose the photoresist in the release holes. Therefore the Si_3N_4 window at the bottom of the release holes may not be opened after the Si_3N_4 RIE because of the photoresist remaining in the hole, as shown in Figure 3-3. Figures 3-4 (a) and (b) show etching with and without the silicon nitride remaining in the release holes, respectively. It would cause a problem in the following releasing step. Extending the exposure time is a direct solution to remove the residual photoresist in the holes. Negative photoresist can also be used in this photolithography to solve this problem.

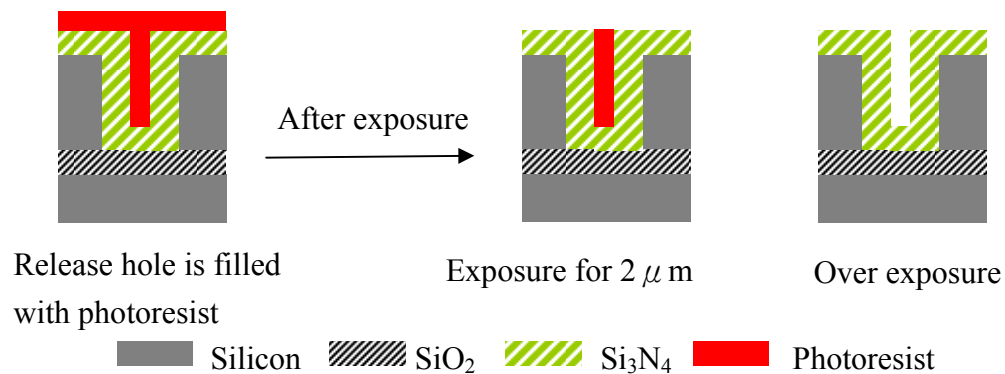


Figure 3-3 Problems in Si_3N_4 photolithography.

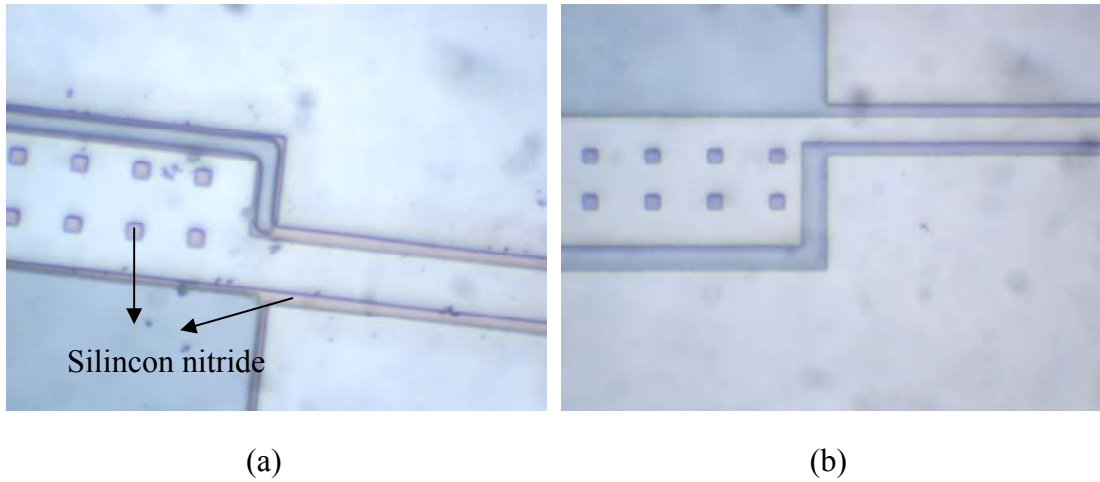


Figure 3-4 After the silicon nitride RIE, (a) silicon nitride remained on the release holes, (b) silicon nitride was etched completely.

3-2-2 Backside ICP etching

Etching from the backside of the substrate was used to eliminate the etch holes on the large mirror plate. However, the large backside hole will cause the silicon device layer and the buried oxide to break due to the residual stress [30]. Figure 3-5 (a) and (b) show the bending and breaking of the large mirror plate after the backside ICP etching. The central area of the mirror plate in Figure 3-5 (a) was measured by WYKO. Figure 3-6 shows WYKO measurement result of the device after backside ICP etching. Figure 3-7 shows the measurement result of the same sample after release. Table 3-1 shows the comparison of radii of curvature of the sample before and after release from the WYKO measurement. As shown in Table 3-1, the radii of curvature of the released samples were much larger than the unreleased samples since the residual stress of the silicon oxide was released.

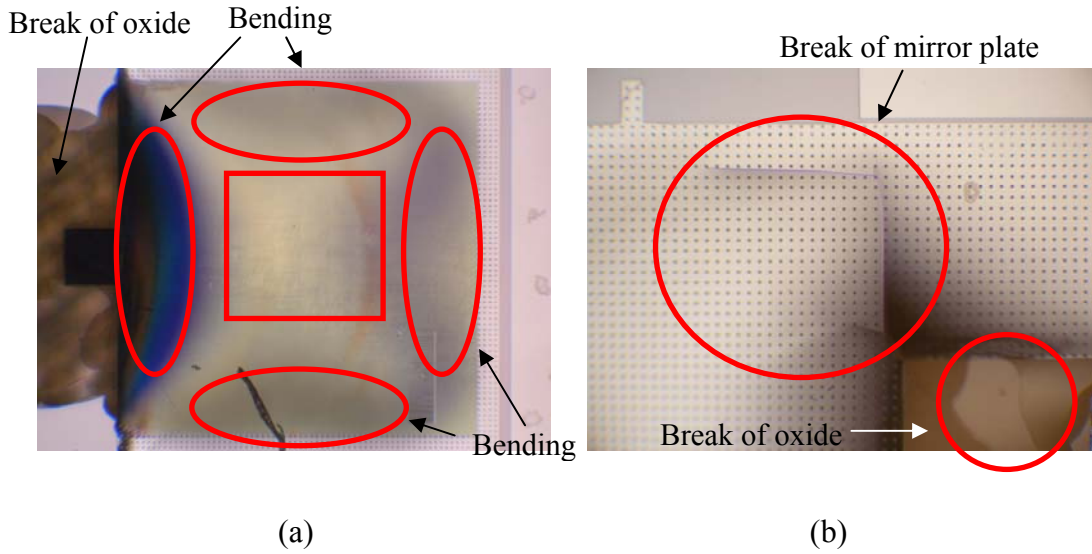


Figure 3-5 (a) Bending of the mirror plate, (b) breaking of the mirror plate after the backside ICP etching.

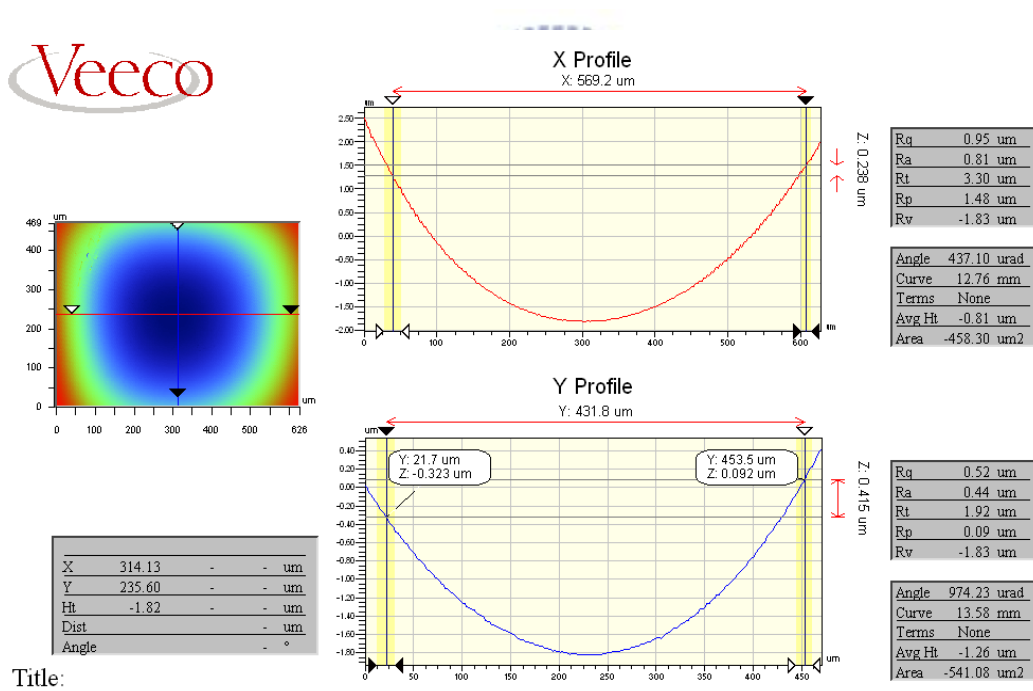
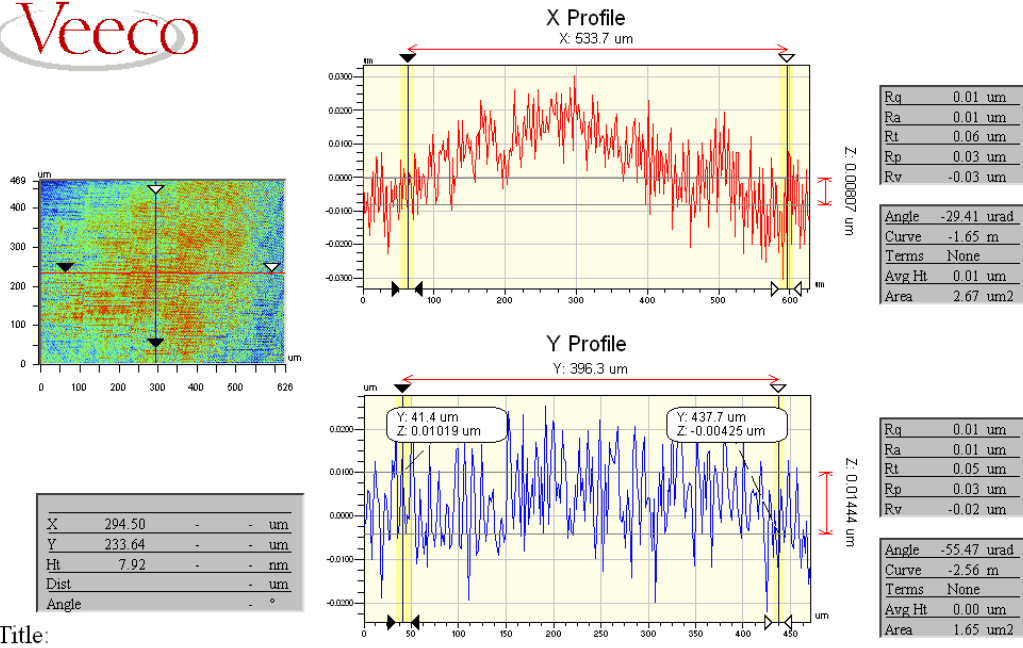


Figure 3-6 Bending of the mirror measured by WYKO before release.



Title:

Figure 3-7 Bending of the mirror measured by WYKO after release.

Table 3-1 Comparison of bending mirror plate.

	Before release	After release
Radius of curvature in <i>x</i> -axis	12.76 mm	-1.65 m
Radius of curvature in <i>y</i> -axis	13.58 mm	-2.56 m

Figure 3-8 shows the front of the mirror plate after the backside ICP process. The 2- μ m-thick buried oxide of the SOI wafers broke during the ICP etching when silicon device layer or substrate are unconnected to the oxide layer. If the etching process continued, the reaction gas would leak through and etch the device layer of the SOI wafer, as shown in Figure 3-9. Figure 3-9 (a) shows the optical micrograph of the front-side mirror plate with HOE after the backside ICP process. The dark area in Figure 3-9 (a) was etched due to the broken buried oxide. The interlock of the locking mechanism was etched seriously in this sample, as shown in Figure 3-9 (b).

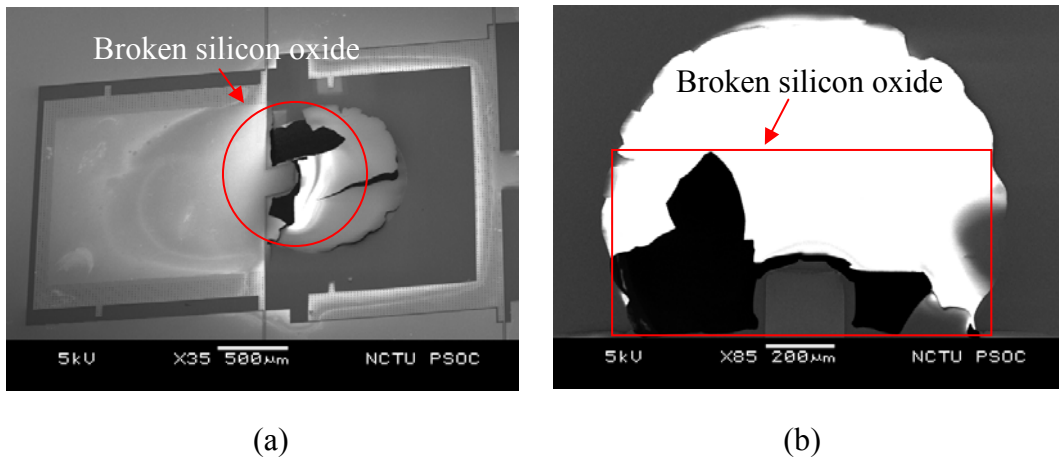


Figure 3-8 Broken silicon oxide at the big through-wafer hole.

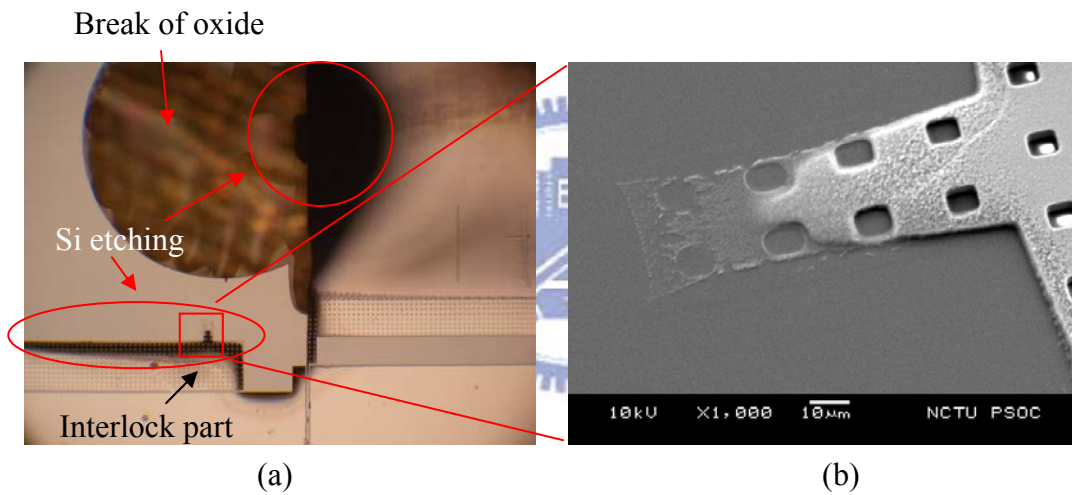


Figure 3-9 Device layer is etched in the backside ICP process.

The problem can be solved by redesigning the backside etching to minimized the area of exposed oxide after ICP, as shown in Figure 3-10. Figure 3-10 (a) shows the released and assembled mirror according to the original mask design. The substrate under the mirror plate is etched completely. So the large mirror plate becomes fragile and susceptible to the stress in the buried oxide layer. Figure 3-10 (b) shows the device after assembly for an improved mask design where a meshed structure is left in the substrate to reinforce the strength of the plate. Another alternative is shown in

Figure 3-10 (c), where the entire substrate is kept unetched and becomes part of the mirror plate. The two improved designs not only reduce the area of etched substrate, but increase the rigidity of the mirror plates by increasing their thickness.

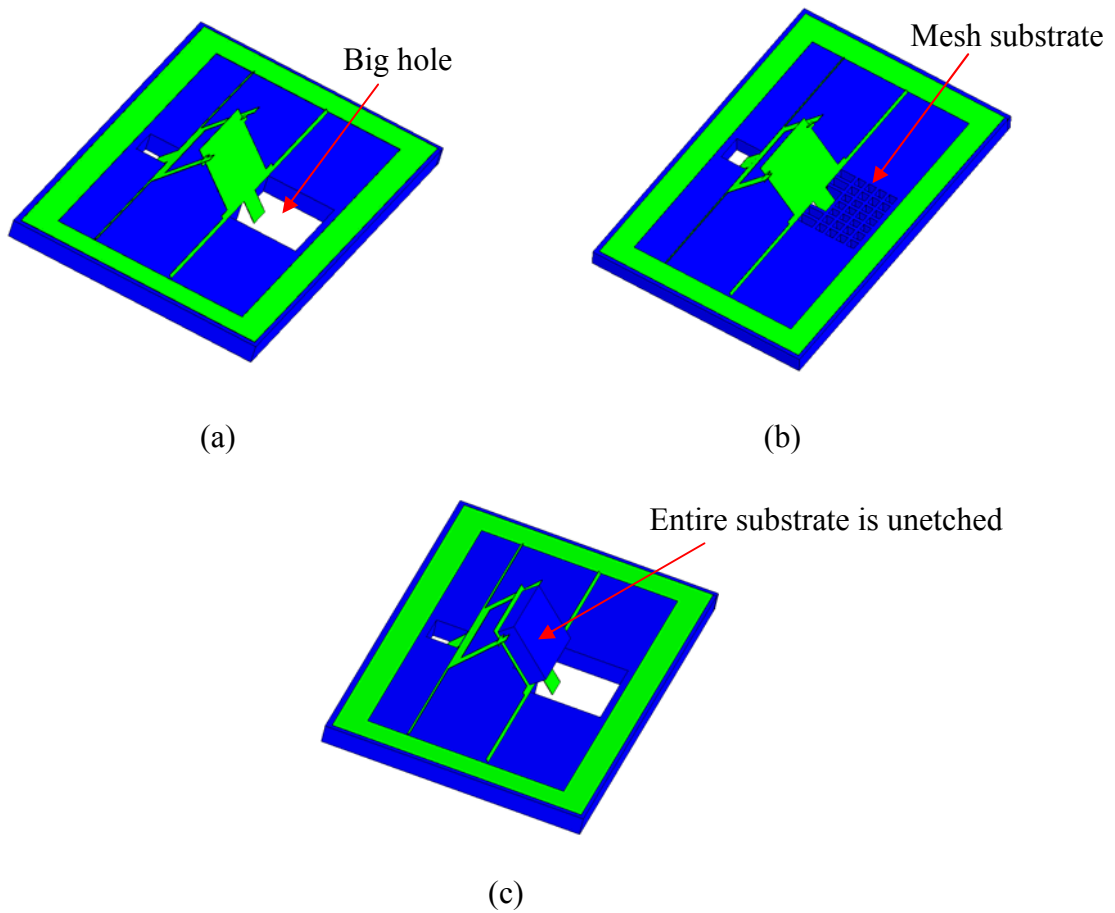


Figure 3-10 Schematic of original and redesigned backside etching under the mirror plate, (a) big hole, (b) meshed structure, (c) entire substrate is unetched.

3-3 Summary

The fabrication process and problems were presented. SEM photographs of fabricated structures are shown in Figure 3-11. Figures 3-11 (a) and (b) show arrays of assembled 45° and 135° mirror. Figure 3-11 (c) shows the side view of the assembled 135° mirror. Figure 3-11 (d) shows the fabricated HOE. In the next chapter, the assembly procedure and assembled devices will be presented.

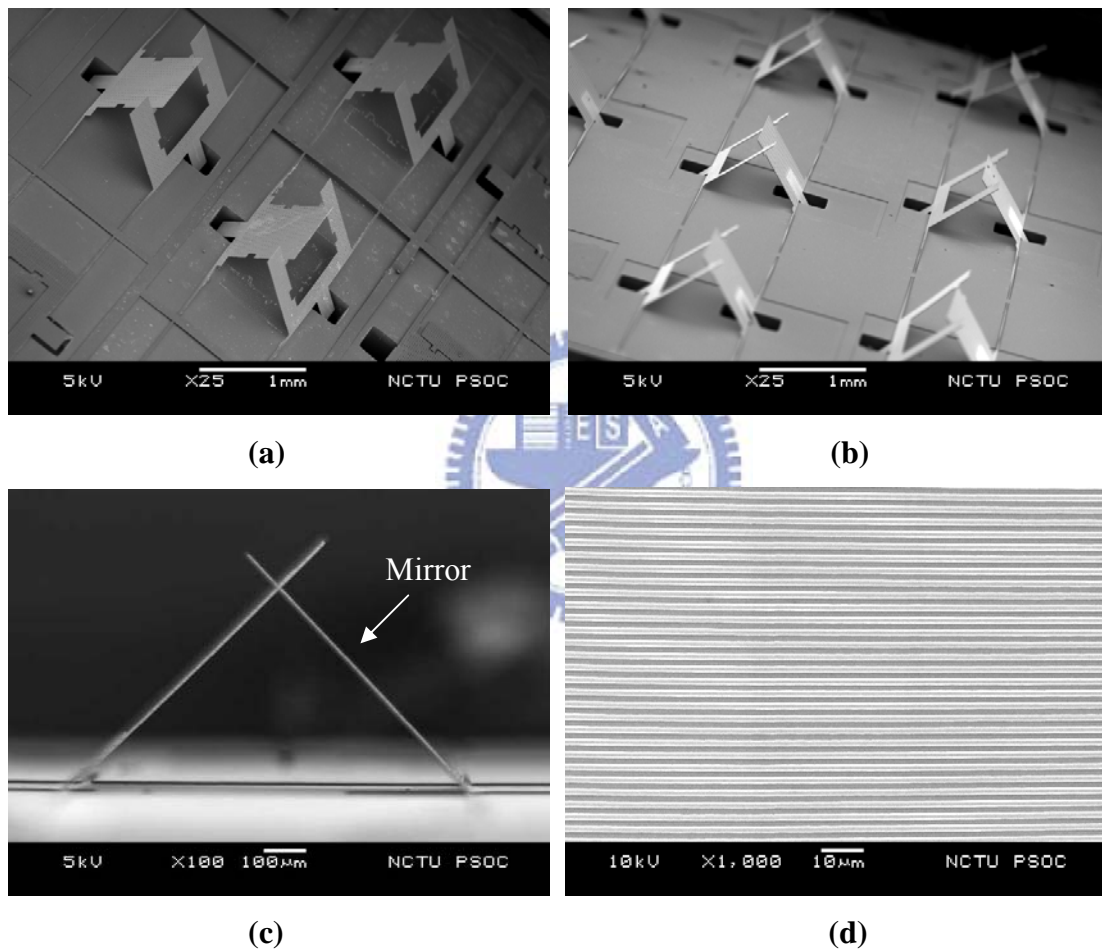


Figure 3-11 Fabricated devices, (a) an array of 45° device, (b) an array of 135° device, (c) side view of an assembled 135° mirror, (d) holographic optical element (HOE).

Chapter 4 Measurement and Results

This chapter presents of experiment and measurement results. The assembly of 3-D microstructures with arbitrary angles is demonstrated. 45° devices with various dimensions of the torsional beams and locking mechanism are used to test the angular accuracy of the assembled devices. 135° devices are fabricated and used in optical benches. Finally, the optical pickup head system is assembled and tested.

4-1 30°, 45°, and 60° structures

Torsional beams instead of hinges were used to assemble micro structures with arbitrary angles. 30°, 45°, and 60° devices were used to demonstrate the feasibility of the assembly method. Figure 4-1 shows the assembly process of a fabricated 45° device. Probe 1 and Probe 2 were aligned with the push pads of the support arms and the mirror plate, respectively (Figure 4-1 (a)). Probe 1 pushed the support arms to over 60° and was held in position (Figure 4-1 (b)). Then Probe 2 pushed the mirror to 40°~50° (Figure 4-1 (c)). As Probe 1 was removed from the support arms, the torque from the torsional beams drove the support arms to lie on the mirror plate (Figure 4-1 (d)). Then Probe 2 was removed so that the support and the mirror were firmly interlocked at the desired angle (Figure 4-1 (e)). Finally, Probe 1 was also removed and the assembly process was completed (Figure 4-1 (f)). The assembly process of the 30° and 60° structures are similar to the process for the 45° device. The SEM micrographs of assembled 30°, 45°, and 60° mirrors are shown in Figure 4-2, Figure 4-3 and Figure 4-4, respectively.

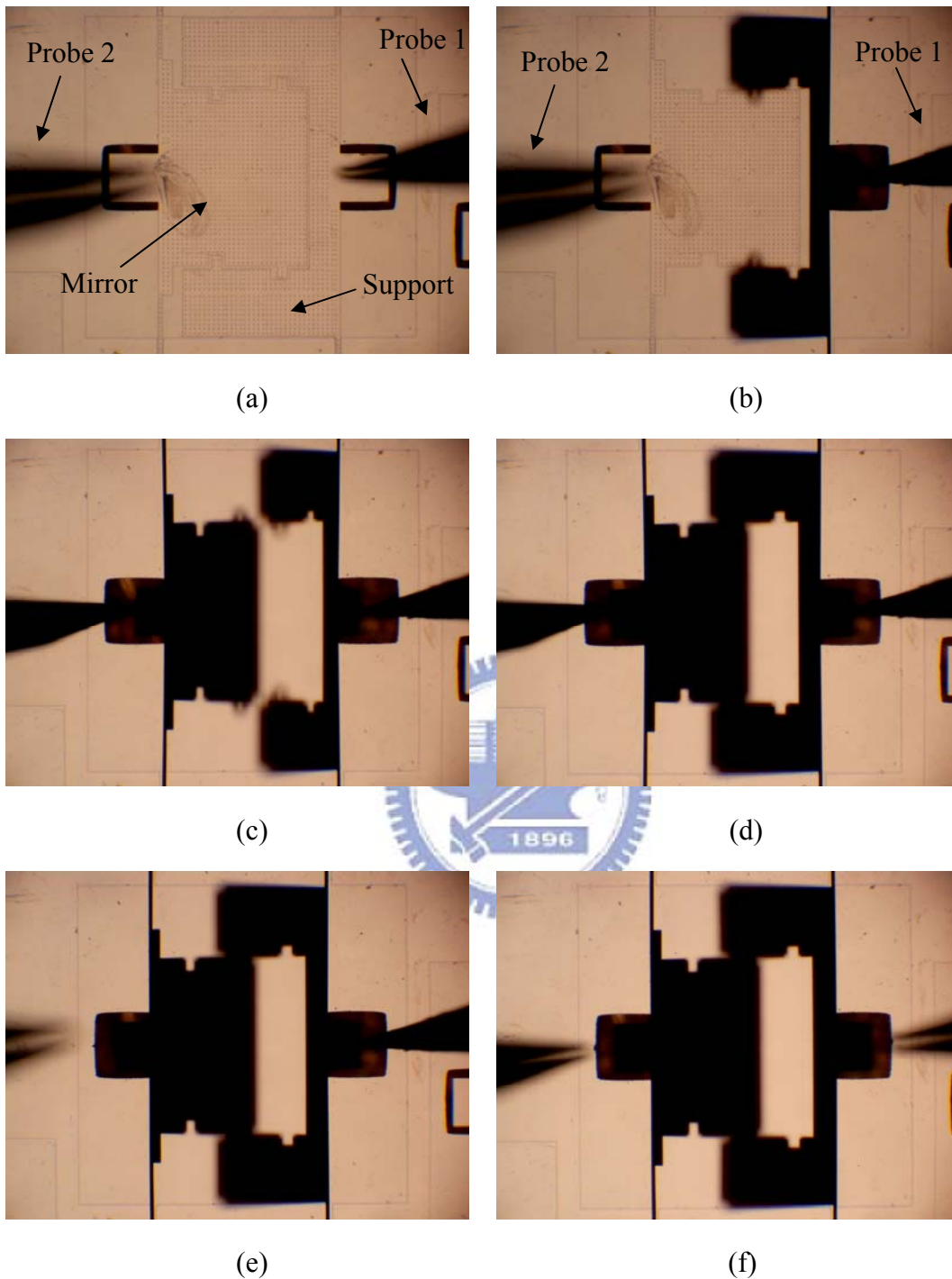


Figure 4-1 Assembly process of a 45° mirror without hinges, (a) two probes were aligned with the push pads before assembly, (b) the support was pushed by Probe 1, (c) the mirror was pushed by Probe 2, (d) remove Probe 1 so that the support lie on the mirror, (e) Probe 2 was removed, (f) Probe 1 was removed.

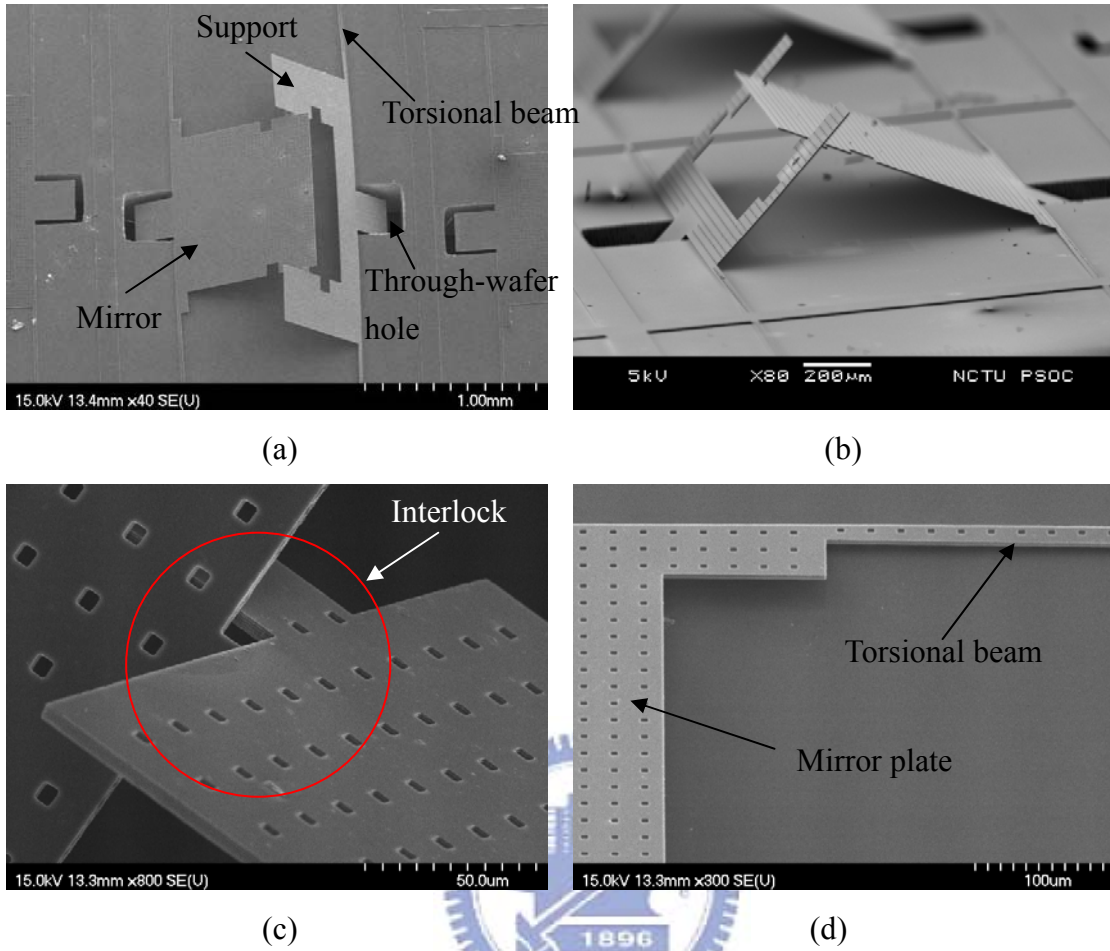


Figure 4-2 An assembled 30° device, (a) top view, (b) side view, (c) interlock, (d) torsional beam connected to the mirror plate.

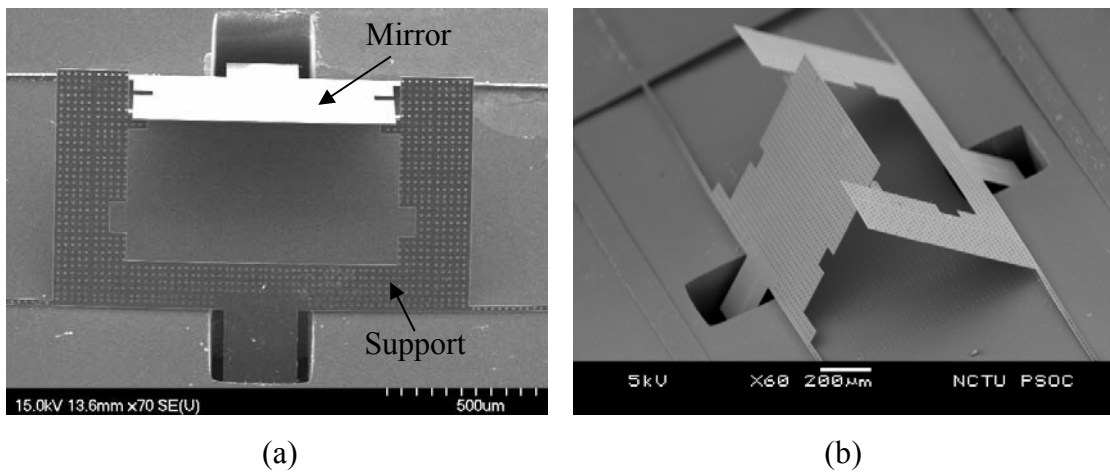
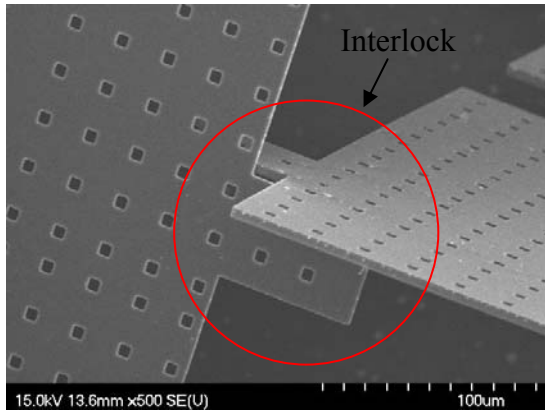
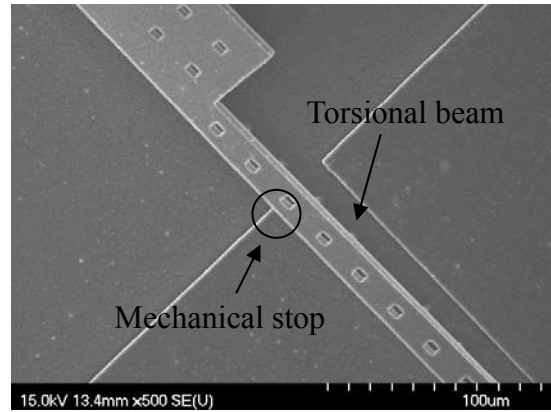


Figure 4-3 An assembled 45° device, (a) top view, (b) side view.

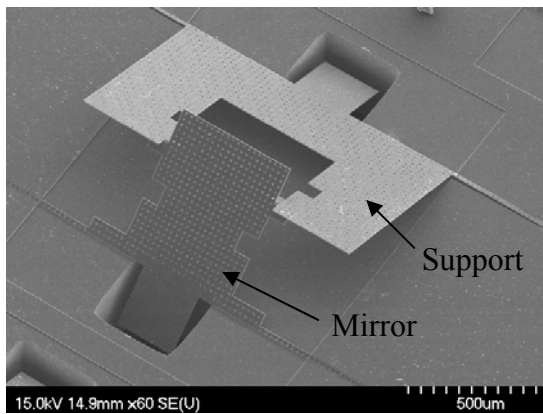


(c)

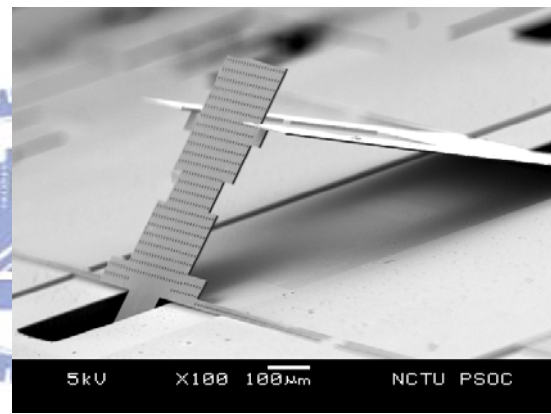


(d)

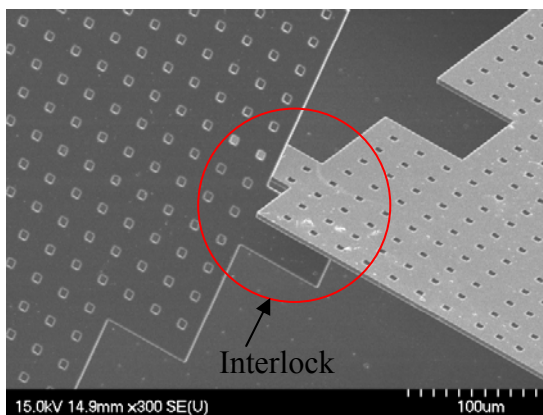
Figure 4-3 An assembled 45° device (continued), (c) interlock (d) torsional beam of the mirror plate with mechanical stop.



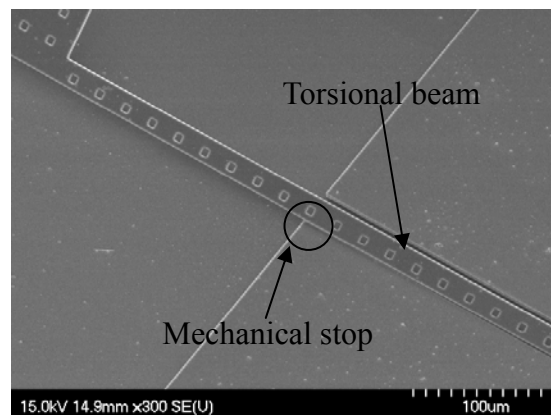
(a)



(b)



(c)



(d)

Figure 4-4 An assembled 60° device, (a) top view, (b) side view, (c) interlock, (d) torsional beam of the mirror plate with mechanical stop.

Angle measurement

The angles of assembled devices are defined by the layout design and measured in the SEM photographs. The resolution of the angular measurement is 0.2° due to the pixel limit of the SEM figures. Figure 4-5, Figure 4-6, and Figure 4-7 show the SEM photographs of assembled 30° , 45° , and 60° devices, respectively, with pixel coordinates marked. The angles are calculated as 30.6° , 45.4° , and 60.7° . Table 4-1, Table 4-2, and Table 4-3 list the angle measurement results of 7 samples randomly selected from the wafer. The average angles are $30.43^\circ \pm 0.2^\circ$, $45.37^\circ \pm 0.2^\circ$, and $60.5^\circ \pm 0.2^\circ$, respectively.

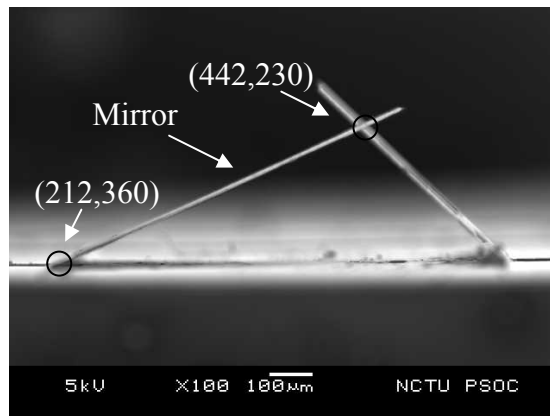


Figure 4-5 An assembled mirror at 30.6° .

Table 4-1 Angle measurement of the 30° device (resolution: 0.2°).

Sample number	Measured angle
1	30.5°
2	30.7°
3	30.3°
4	30.6°
5	30.4°
6	30.3°
7	30.2°
Average angle	$30.43^\circ \pm 0.2^\circ$

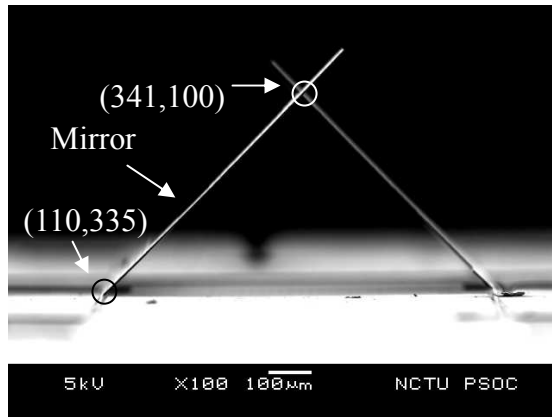


Figure 4-6 An assembled mirror at 45.4°.

Table 4-2 Angle measurement of the 45° device (resolution: 0.2°).

Sample number	Measured angle
1	45.6°
2	45.4°
3	45.1°
4	45.3°
5	45.2°
6	46.5°
7	45.7°
Average angle	45.37° ± 0.2°

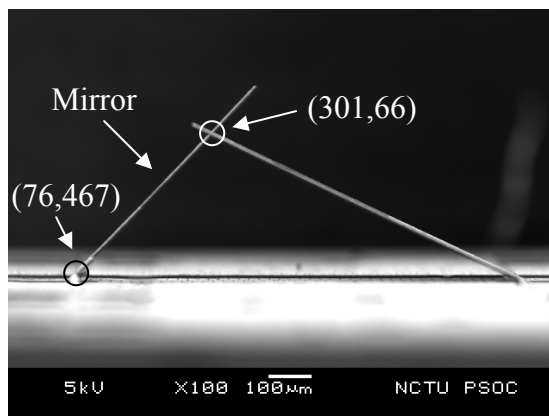


Figure 4-7 An assembled mirror at 60.7°.

Table 4-3 Angle measurement of the 60° device (resolution: 0.2°).

Sample number	Measured angle
1	60.6°
2	60.2°
3	60.5°
4	60.7°
5	60.4°
6	60.6°
7	60.5°
Average angle	60.5°± 0.2°

Bending problems

In our previous demonstration [22], the angular deviation of the assembled device from the desired angle was caused by the bending of the supports, as shown in Figure 4-8. This problem causes large angular inaccuracy after assembly. In our prior design [22], the length and width of the torsional beams were 45 μm and 700 μm, respectively; the width of the support arm was 120 μm. The deformation of the bent support was measured by a WYKO NT1100 interferometer. Figure 4-9 (a) shows the 3-D profile of the bent supports. Figure 4-9 (b) shows the 2-D profiles of the AC cut and the AB cut in Figure 4-9 (a). In the current design, wider support arms (230 μm wide) and thinner torsional beams (25 μm wide) are used to improve the design and reduce the bending problem. Figure 4-10 also shows the 3-D and 2-D profiles of the improved design by WYKO measurements. In the AC profile, the radii of curvature in the prior design and the current design are -34.61 mm and -51.04 mm, respectively. These values are not improved significantly because the stress can not be released due to the torsional beams on the sides of the mirror plate. In the AB profile, the radii of curvature in the prior design and the current design are increased from 4.12 mm to 89.65 mm. From these comparisons, the bending of the support can be improved by increasing the mechanical strength. Table 4-4 shows the comparison of radii of

curvature between the prior design and the current design in the x -direction and y -direction. The theoretical values are calculated by Equation 2-4.

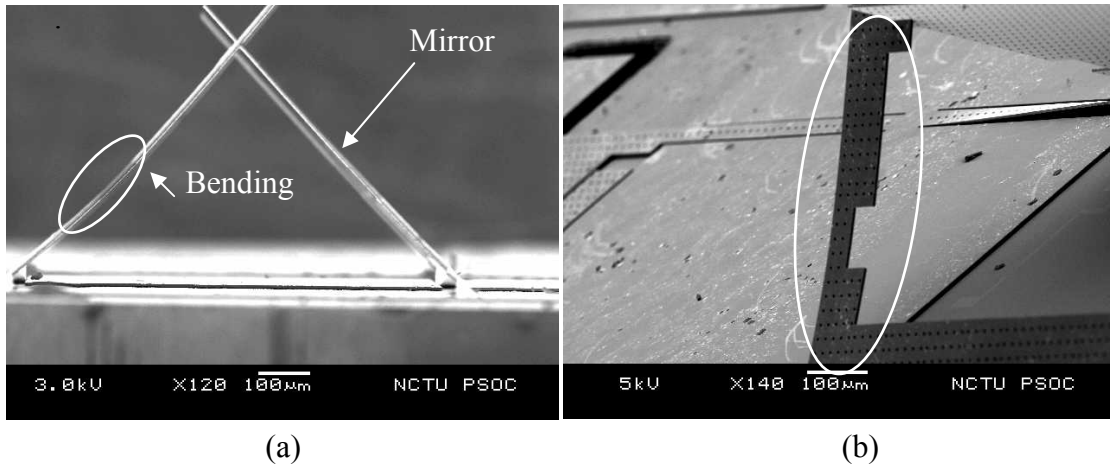


Figure 4-8 Bent supports, (a) side view, (b) perspective view [22].

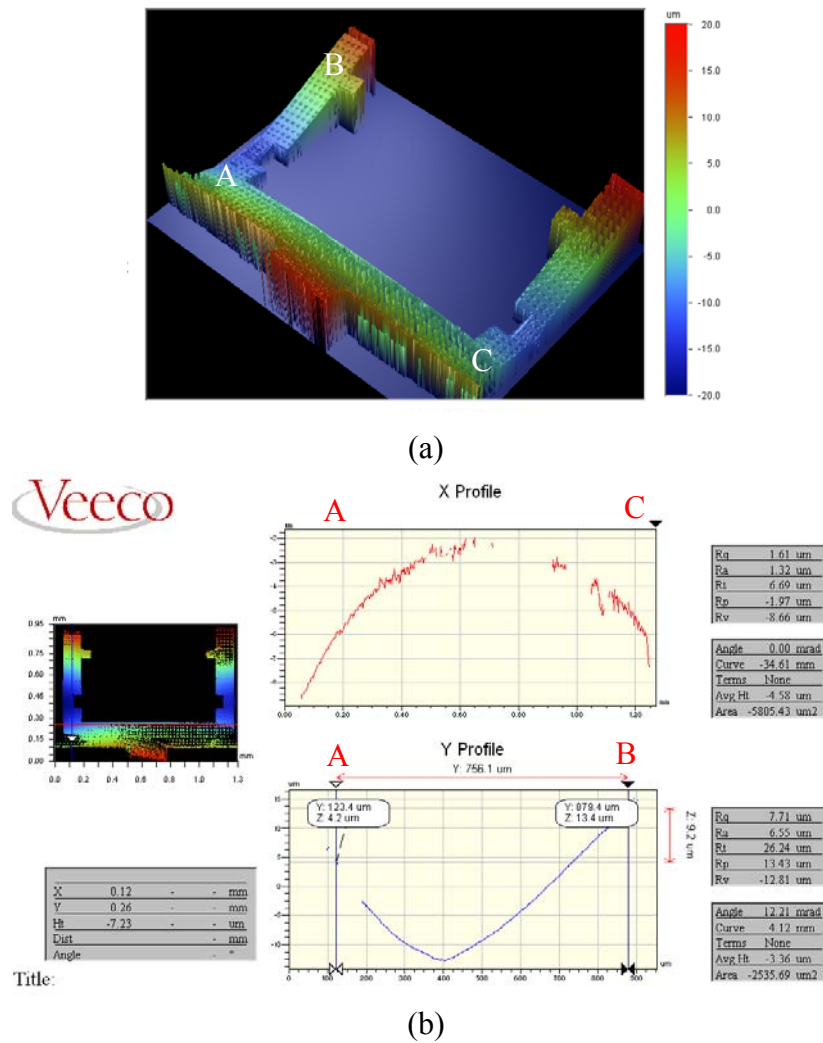
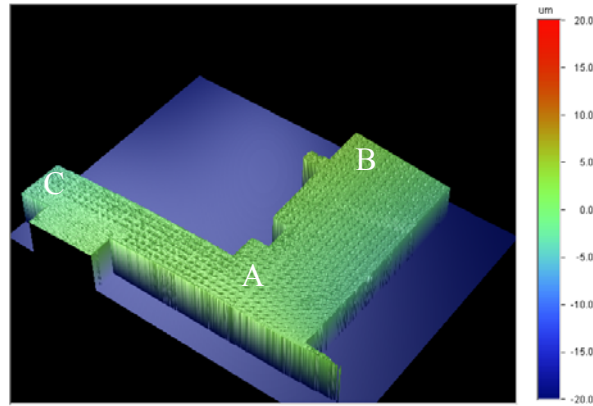
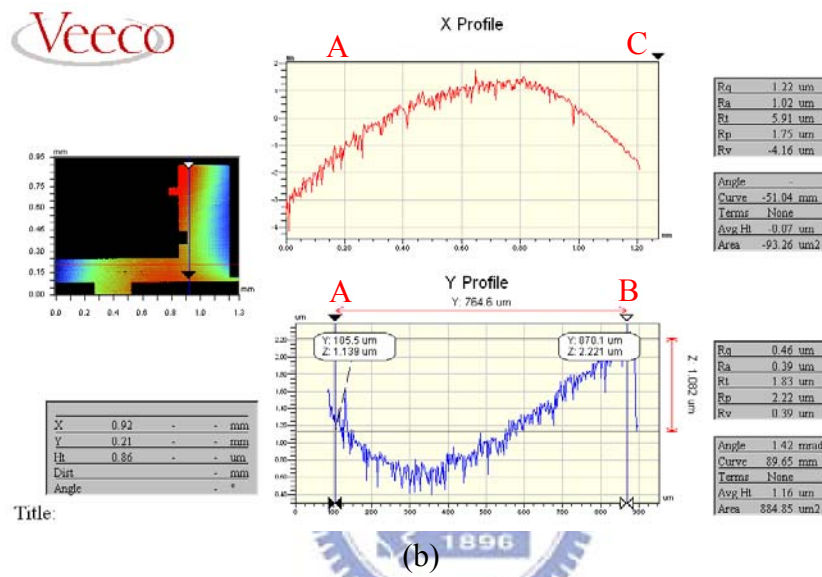


Figure 4-9 Bending of supports in prior design after assembly, (a) 3-D profile, (b) 2-D analysis [22].



(a)



(b)

Figure 4-10 Bending of improved supports in this work after assembly, (a) 3-D profile, (b) 2-D analysis.

Table 4-4 Comparison of support bending with different design, (a) x-axis, (b) y-axis.

(a) x-axis (AC cut)

Width of support	Prior design (120 µm)	Current design (350 µm)
Radius of curvature	-34.61 mm	-51.04 mm

(b) y-axis (AB cut)

Width of support	Prior design (120 µm)	Current design (350 µm)
Radius of curvature	4.12 mm	89.65 mm
Theoretical value	0.9 mm	19.58 mm

4-2 135° structures

The assembly method can be applied for arbitrary angles even if the angles are over 90°. Figure 4-11 shows the assembly process of a fabricated 135° device. Probe 1 was first aligned with the push pad of the mirror plate (Figure 4-11 (a)). Probe 1 then pushed the mirror plate to near 90°. Probe 2 held the mirror plate from the other side (Figure 4-11 (b)) and Probe 1 was removed from the mirror plate. It then pushed the support arms to over 70° (Figure 4-11 (c)) and Probe 2 pushed the mirror plate forward to 140° to 150° (Figure 4-11 (d)). Probe 1 was removed subsequently and the support lay on the mirror by the restoring force from the torsional beams of support (Figure 4-11 (e)). Finally, Probe 2 was removed and the assembly process was completed (Figure 4-11 (f)).

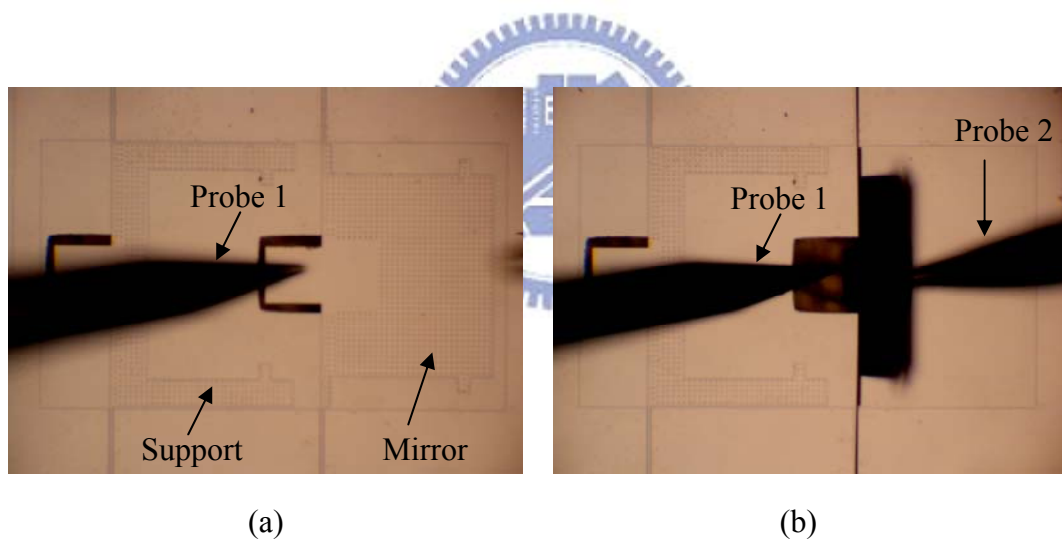


Figure 4-11 Assembly process of a 135° mirror without hinge, (a) two probes aligned before assembly, (b) mirror plate pushed by Probe 1 and held by Probe 2 from the other side.

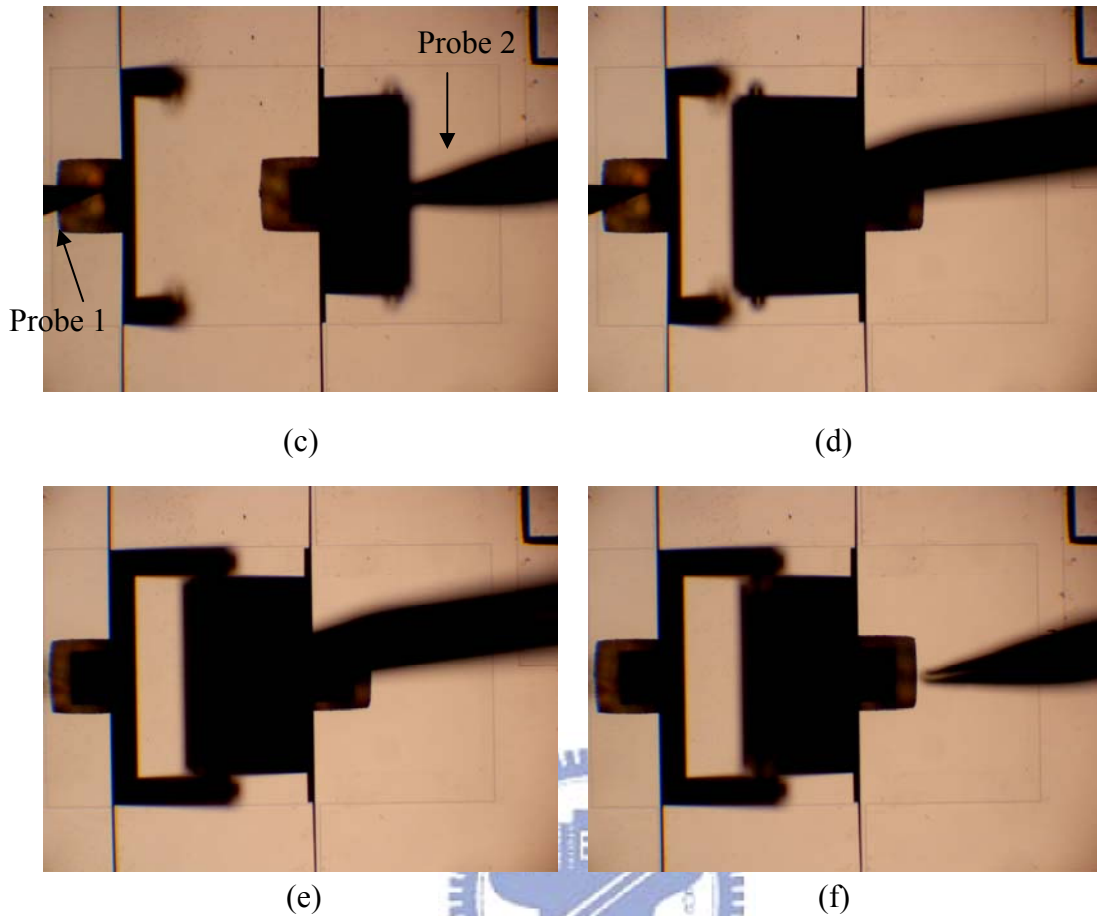


Figure 4-11 Assembly process of a 135° mirror without hinge (continued), (c) Probe1 removed from the mirror plate and support pushed by Probe 1, (d) mirror plate pushed by Probe 2, (e) Probe 1 remove from support, (f) Probe 2 removed.

Figure 4-12 shows the SEM photographs of the 135° device after assembly. Figures 4-12 (a) and 4-12 (b) show the top view and side view. 4-12 (c) and 4-12 (d) show the highlight of the push pad of the mirror plate and the interlock part. Figure 4-12 (e) show the torsional beam of the mirror plate after assembly. Mechanical stops on the sides of the torsional beams were used to limit the lateral displacement of the beam, as shown in Figure 4-12 (f).

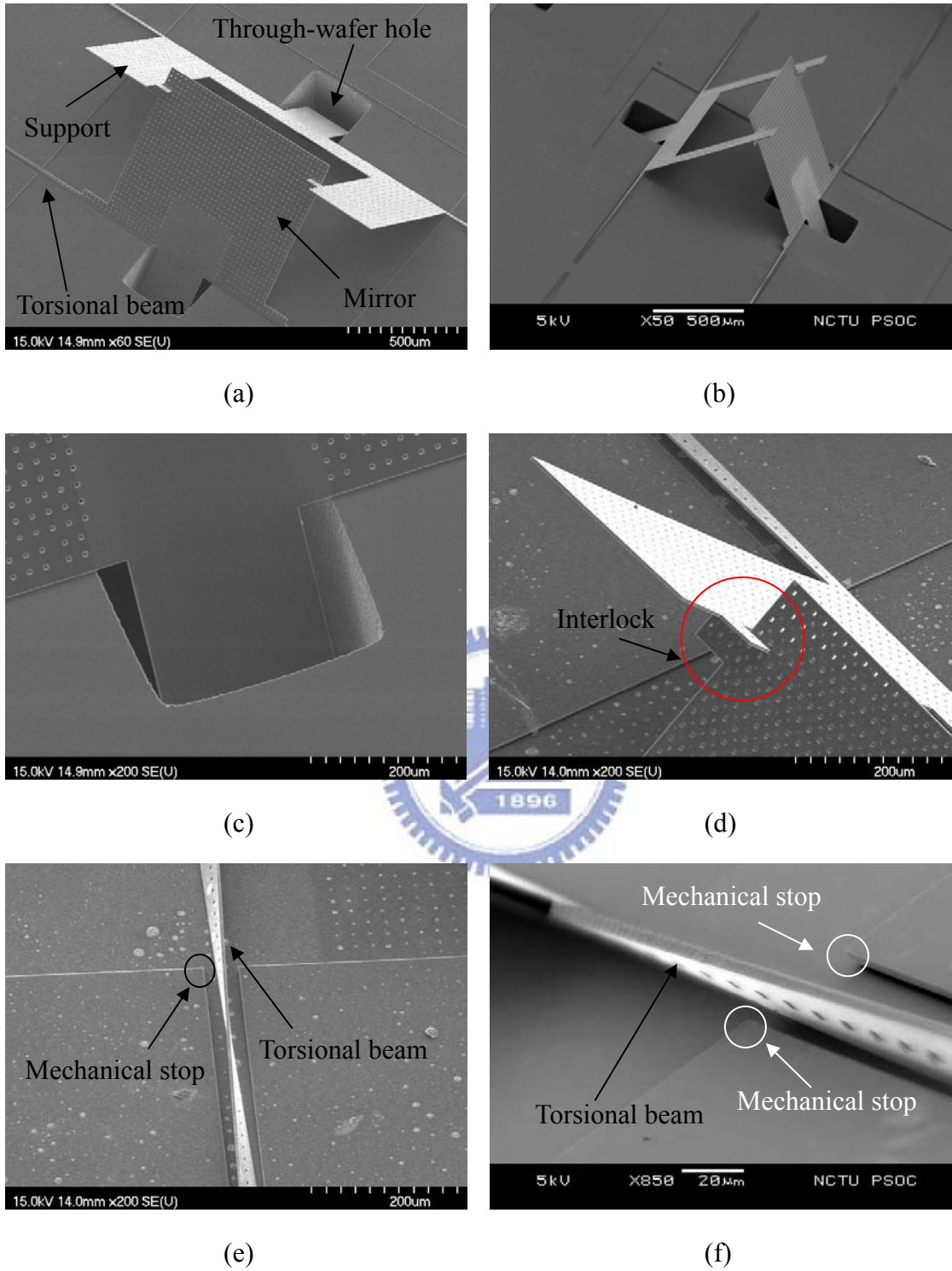


Figure 4-12 An assembled 135° device, (a) top view, (b) side view, (c) push pad of mirror plate, (d) interlock, (e) torsional beams of mirror plate, (f) torsional beams and mechanical stops.

Angle measurement

Figure 4-13 shows the SEM photographs of an assembled 135° devices. The angle was measured as 135.4°. Table 4-5 list the angle measurement results of 7 samples randomly selected from the wafer. The average angle was $135.64^{\circ} \pm 0.2^{\circ}$. The 135° devices must be used in the proposed optical bench. The tolerance of the assembled angle was

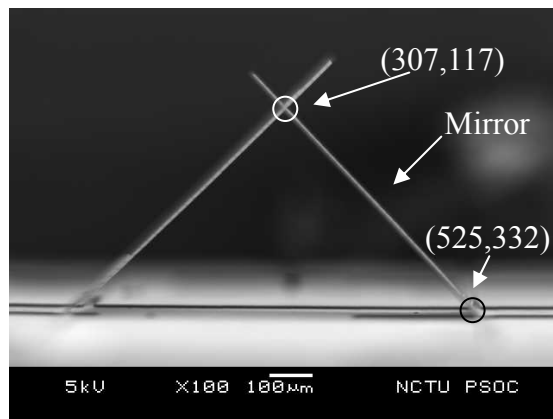


Figure 4-11 An assembled mirror at 135.4°.

Table 4-5 Angle measurement of the 135° device (resolution: 0.2°).

Sample number	Measured angle
1	135.7°
2	135.5°
3	135.9°
4	135.1°
5	135.4°
6	135.5°
7	135.4°
Average angle	$135.64^{\circ} \pm 0.2^{\circ}$

4-3 Holographic optical element (HOE)

The design of the holographic optical element (HOE) was discussed in Chapter 2. The surface profile and the optical properties of the fabricated HOE were measured. The fabricated devices and the measurement results are presented in the following sections.

4-3-1 Surface profile

Figure 4-14 and Figure 4-15 show the optical and SEM micrographs of the fabricated HOE. The linewidth was measured by the SEM micrograph, as shown in Figure 4-15. Figure 4-15 (a) shows the fabricated HOE. Figures 4-15 (b)-(d) show the measurement of the period and linewidth, respectively. The design values of the linewidth and the etching depth are $1.3\ \mu\text{m}$ and $253.4\ \text{nm}$, respectively. The period of the HOE was measured as $2.8\ \mu\text{m}$. The measured width of the etched and the unetched regions were $1.44\ \mu\text{m}$ and $1.36\ \mu\text{m}$, respectively. The inaccuracy of the linewidth and period was caused by the photolithography and RIE processes because the resolution of the mask aligner was only $1\ \mu\text{m}$. The linewidth and etching depth of the HOE were also measured by an Atomic Force Microscope (AFM), as shown in Figure 4-16. The measured linewidth and depth were $1.395\ \mu\text{m}$ and $254.5\ \text{nm}$, respectively. Table 4-6 shows the comparison between the design values and the measurement results. The etching depth is related to diffraction efficiency, as will be discussed in the next section.

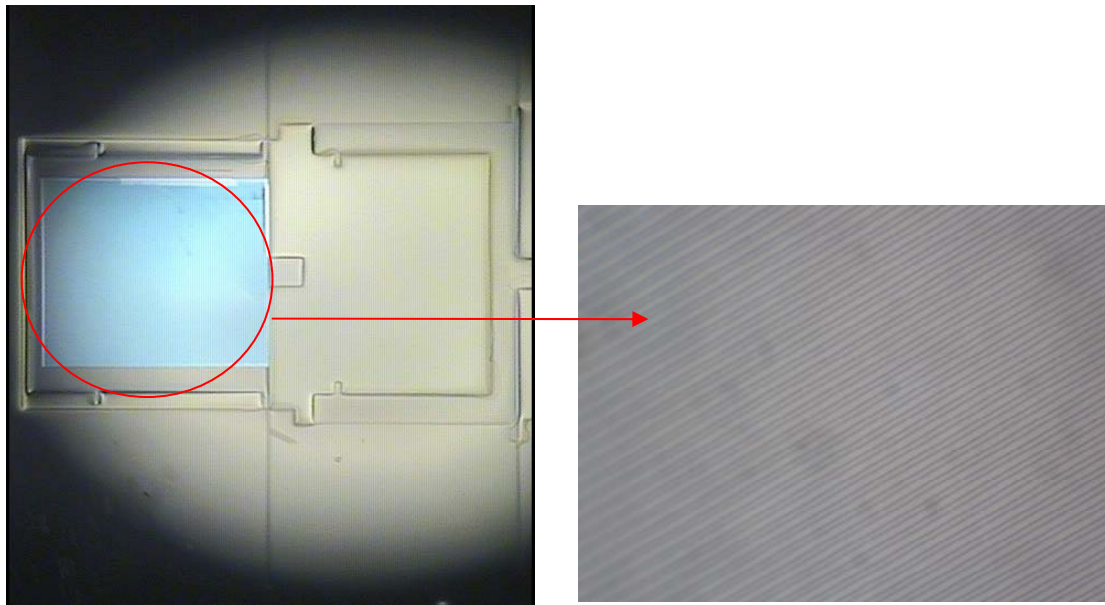


Figure 4-14 Optical micrographs of the fabricated HOE.

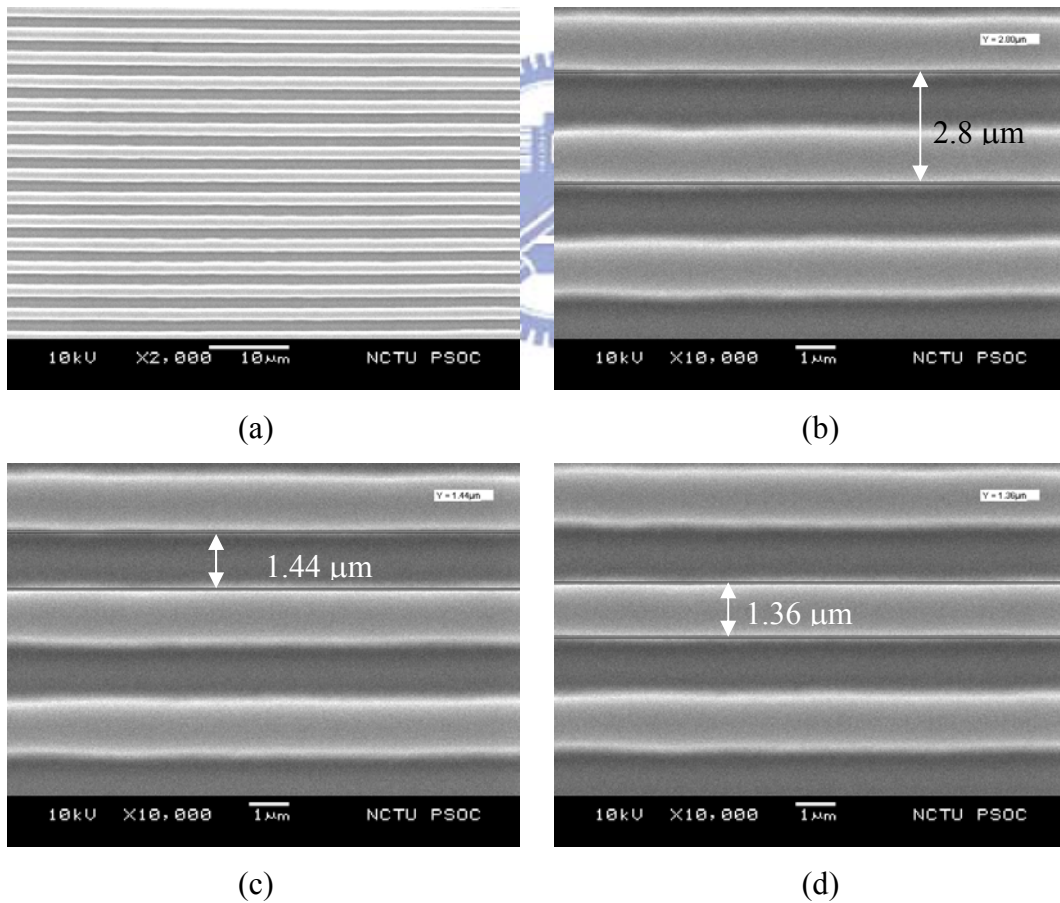


Figure 4-15 SEM micrographs of the HOE, (a) fabricated HOE, (b) period of HOE, (c) linewidth of the etching area, (d) linewidth of the unetching area.

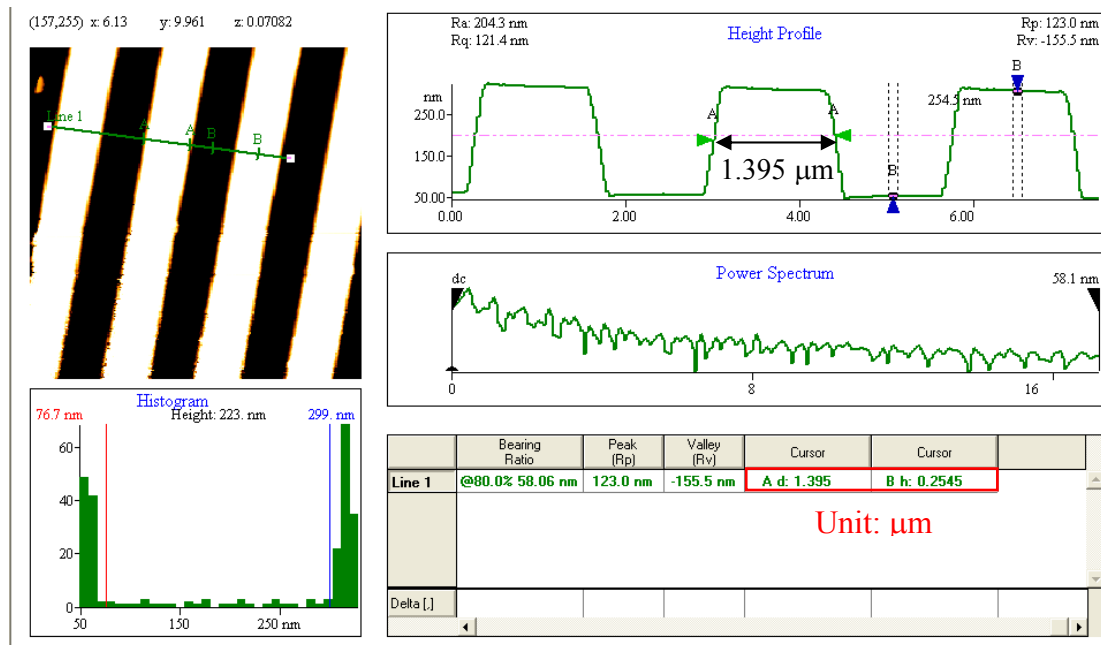


Figure 4-16 AFM measurement results.

Table 4-6 Comparison of design values and AFM measurement results of the HOE.

	Design value	Measurement result
Linewidth	1.3 μm	1.395 μm
Etching depth	253.4 nm	254.5 nm

4-3-2 Optical measurement

The diffracted optical spots and the diffraction efficiency of the HOE were measured optically as shown in Figure 4-17. The laser beam was first weakly focused on the HOE by a lens with a focus length of 10 cm. The incident angle of the laser beam was adjusted to 45° by a rotation stage. The experimental setup is shown in Figure 4-18.

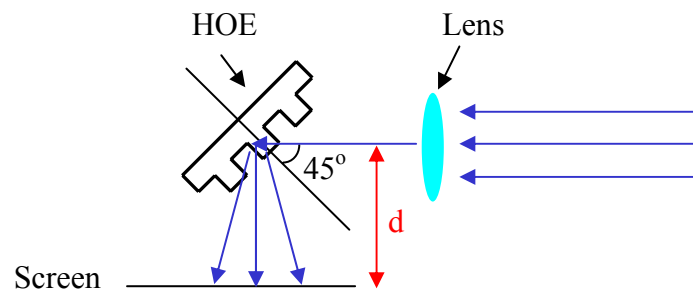


Figure 4-17 Illustration of the optical measurement.

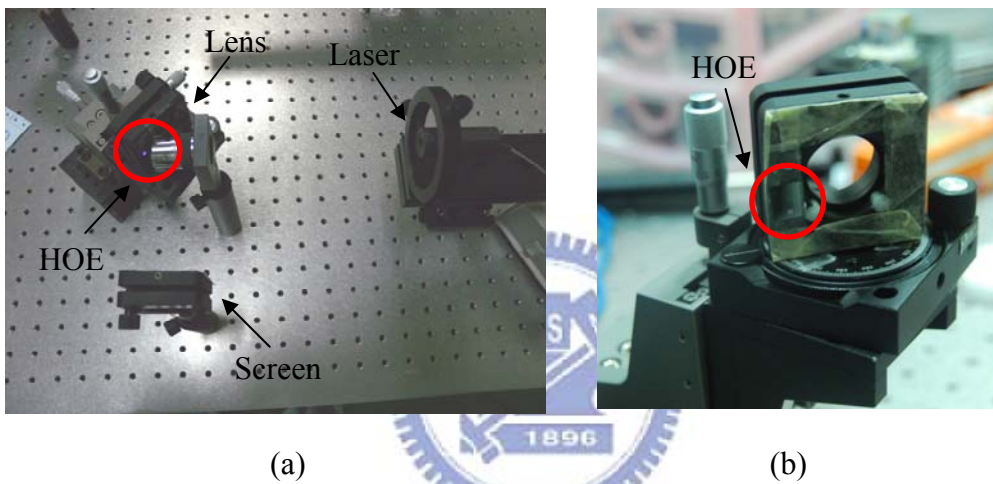


Figure 4-18 (a) Experimental setup, (b) highlight of the HOE.

Figure 4-19 shows the diffracted optical spots on the screen at $d = 100$ mm. The power of the zeroth-order and the first-order diffraction optical spots were measured by an optical power meter. Table 4-7 shows the measured diffraction efficiency and etching depth of 8 samples. The design value of power ratio of the zeroth-order and first-order beams and etching depth are 2.5 and 253.4 nm, respectively.

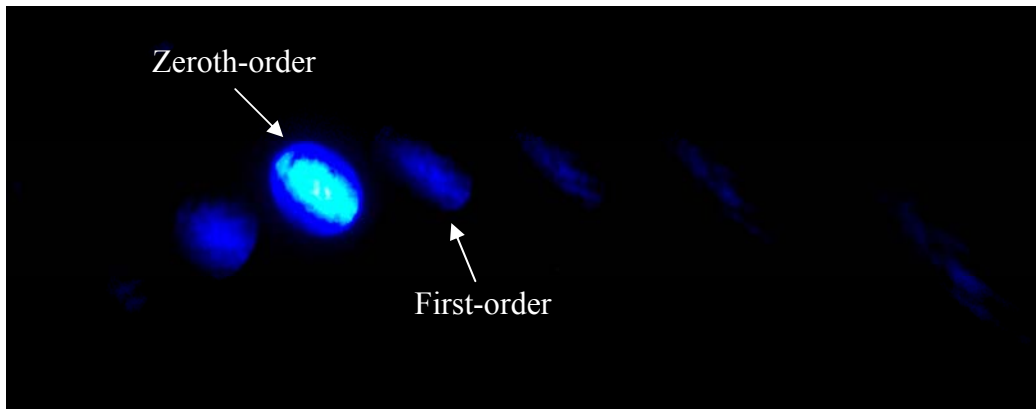


Figure 4-19 Diffraction optical spots projected on the screen.

Table 4-7 Measurement results of diffraction optical intensity and etching depth.

	Zeroth order	First order	Zeroth order / First order	Measured etching depth by AFM
Sample 1	18.04 mW	3.68 mW	4.9	256.9 nm
Sample 2	13.1 mW	3.3 mW	3.97	255 nm
Sample 3	16.8 mW	3.5 mW	4.8	257.3 nm
Sample 4	14.5 mW	3.4 mW	4.26	257.1 nm
Sample 5	15.6 mW	4.2 mW	3.71	249 nm
Sample 6	17.2 mW	2.8 mW	6.14	253.7 nm
Sample 7	16.4 mW	3.2 mW	5.12	261 nm
Sample 8	13.9 mW	4.9 mW	2.84	238.1 nm

4-3-3 Discussion

Figure 4-20 shows the comparison of measured and calculated power ratio of 8 samples. The x-axis is the etching depth from 225 nm to 275 nm ($250 \text{ nm} \pm 10\%$), the y-axis is the ratio of the zeroth-order to the first-order power. The curve represents

the theoretical calculation from Equation 2-7. The measured data do not agreed with the calculated curve exactly. This is because the diffraction efficiency was calculated by assuming the HOE was a linear phase grating. But the pattern of HOE has asymmetrical shape and variable linewidth which should be considered in the theoretical calculation. So the calculation should be extended to a more complex two dimensional Fourier transform.

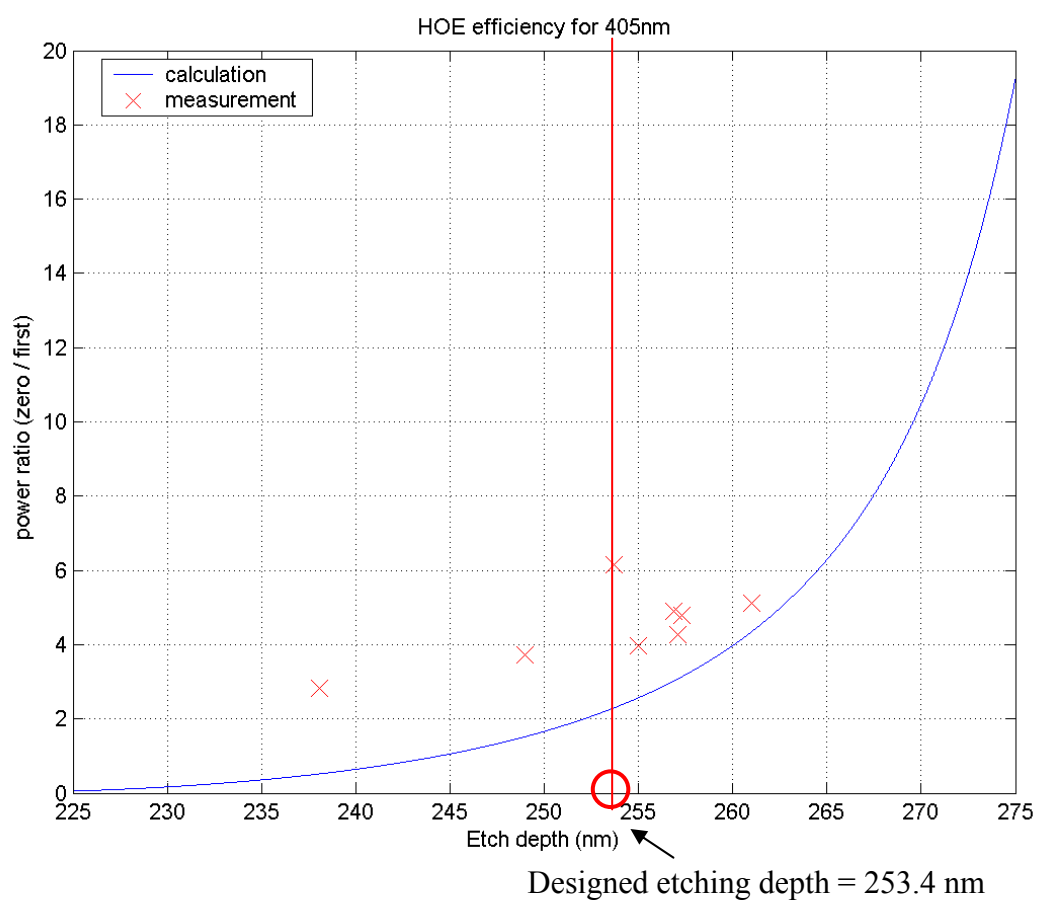


Figure 4-20 Comparison of diffraction efficiency between the measurement and theoretical curve.

4-4 Optical bench

The fabrication process of the optical bench is in progress, as shown in Figure 4-21. Fig. 4-21 (a) shows the optical micrographs of a fabricated optical bench. Fig. 4-21 (b) is the 135° MEMS mirror with HOE. The backside ICP etching is in progress, we are currently releasing the sample and complete the assembly process of the optical pickup head. Detail assembly process of the optical pickup unit is discussed in the next Chapter.

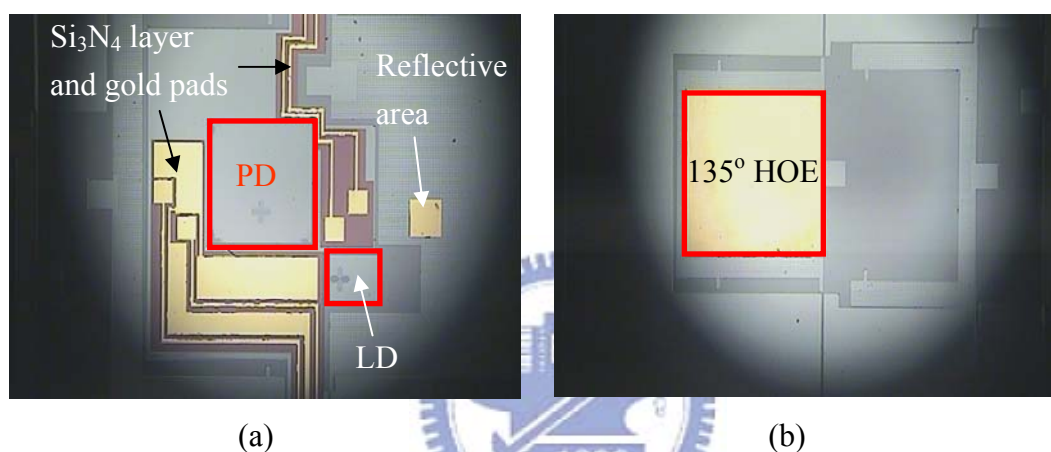


Figure 4-21 Fabricated optical bench.

4-5 Summary

Assembly of micromirror with arbitrary angles was demonstrated even if the angles were over 90°. The 45° device was improved to average $45.4 \pm 0.2^\circ$, compared to our previous study, $45.9 \pm 0.2^\circ$ [22]. The 135° devices were assembled at average $135.6 \pm 0.2^\circ$. The surface profile and the optical properties of the fabricated holographic optical element (HOE) were measured. The power ratio of the zeroth-order and first-order beams was measured to be 2.8, closed to the desired value of 2.5.

Chapter 5 Conclusion and Future work

5-1 Conclusion

Nonvertical mirrors with arbitrary angles were realized in this thesis. It can be used in various optical systems. Furthermore, the problems of angular deviation of 45° devices were discussed and the angular accuracy were improved to $45.4 \pm 0.2^\circ$. The assembly of the 135° structures was verified and demonstrated. A holographic optical element was fabricated and measured optically. The fabrication process of the optical bench was completed. We are currently releasing the sample and complete the assembly process of the optical pickup head.

5-2 Future Work

Some of the problems encountered in this thesis need to be considered more carefully in the future. Nonvertical micromirrors and optical bench are discussed below.



5-2-1 Nonvertical devices

The thickness of the SOI device layer should be increase to prevent the mirror plate from breaking after the backside ICP etching. The dimension of the torsional beams and release holes should be resigned if the thickness of the device layer is increased. The geometry for the torsional beam needs to be redesigned to decrease the bending of the support arms in the x -axis. The maximum shear stress in the torsional beam should be reduced to 2 GPa in the design because shear stress of manufactured silicon can be smaller than the ideal 7 GPa. The devices were assembled individually using microprobes in this thesis. The concept and assembly process can be extended to batch assembly by probe arrays with precise positioning equipments. Furthermore,

we can test the dynamic response of assembled 135° structures to ensure the mirror plate is rigid when subject to a suddenly disturbance.

5-2-2 Optical bench

The proposed optical pickup system with 135° micromirrors in this thesis can be assembled by the demonstrated assembly method. The fabrication of the optical bench is in progress. The assembly process of the released optical bench is shown in Figure 5-1. The released structures is bond on a print circuit board (PCB) (Figure 5-1 (a)). Alternatively, the PCB can be replaced by extending the length of the optical bench, but the pads must be redesigned. After the photodetector (PD) is bonded on the device layer of the optical bench, it is wire bonded to the pads and PCB (Figure 5-1 (b)). Then the mirror is assembled by the push method (Figure 5-1 (c)). A spacer is bonded on the optical bench (Figure 5-1 (d)) since the optical pickup head system must be reversed to assemble the objective lens on the substrate (Figure 5-1 (e)). Figure 5-2 shows the fabricated PCB and holder. The PCB has an opening for the objective lens. The thickness of the PCB is only about $250\ \mu\text{m}$, smaller than the working distance of the objective lens. Figure 5-3 (a) shows the 3-D schematic of the assembled optical pickup unit. A test experiment was conducted to bond the PCB, holder, and objective lens on the big through-wafer hole, as shown in Figure 5-3 (b).

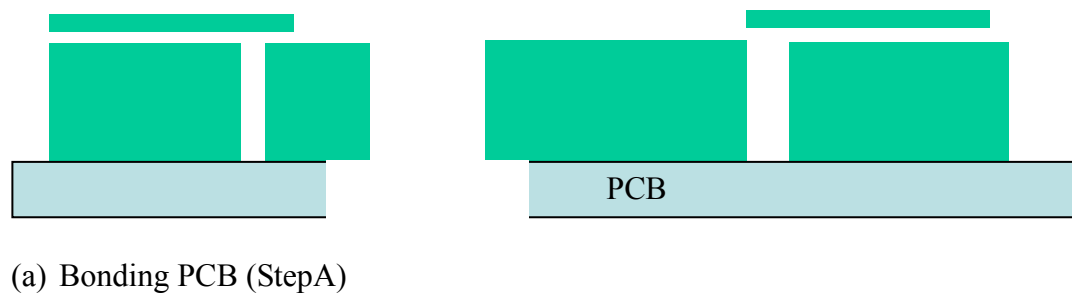
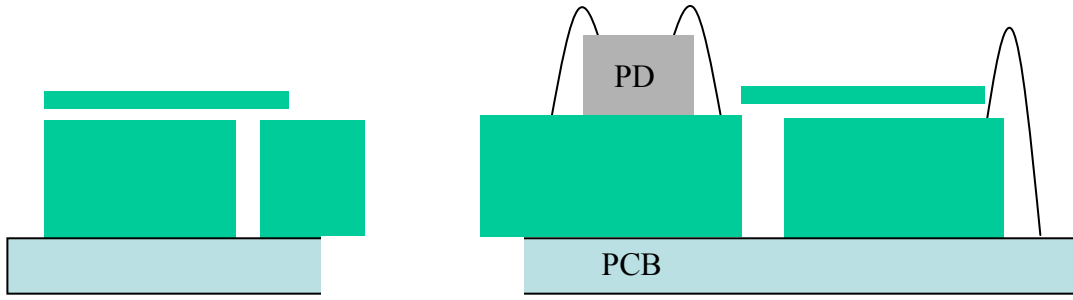
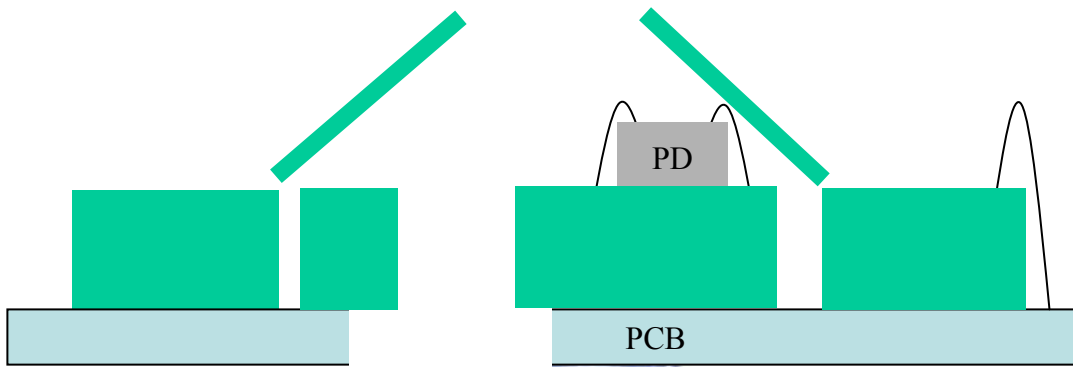


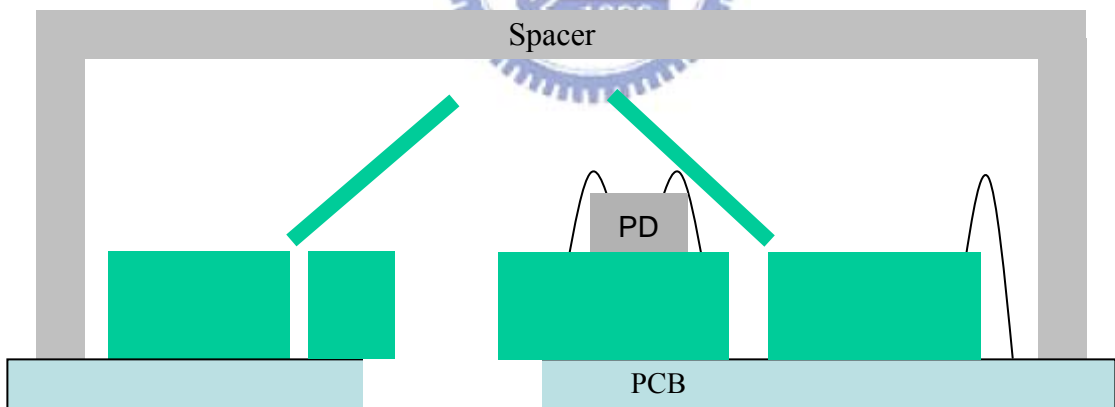
Figure 5-1 Assembly process of optical pickup unit.



(b) Bonding photodetector and wire bond (Step B)

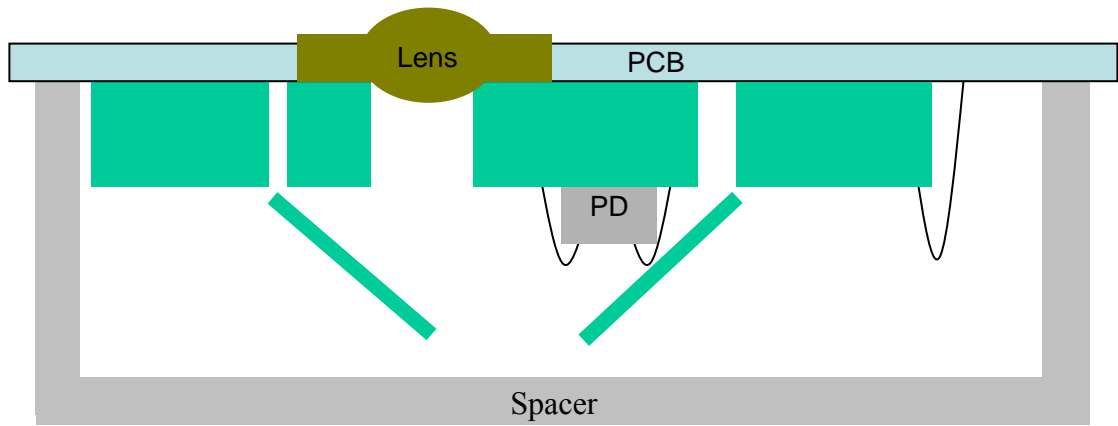


(c) Assembling 135° mirrors (Step C)



(d) Bonding spacer (Step D)

Figure 5-1 Assembly process of optical pickup unit (continued).



(e) Reversing sample and bonding objective lens (Step E)

Figure 5-1 Assembly process of optical pickup unit (continued).

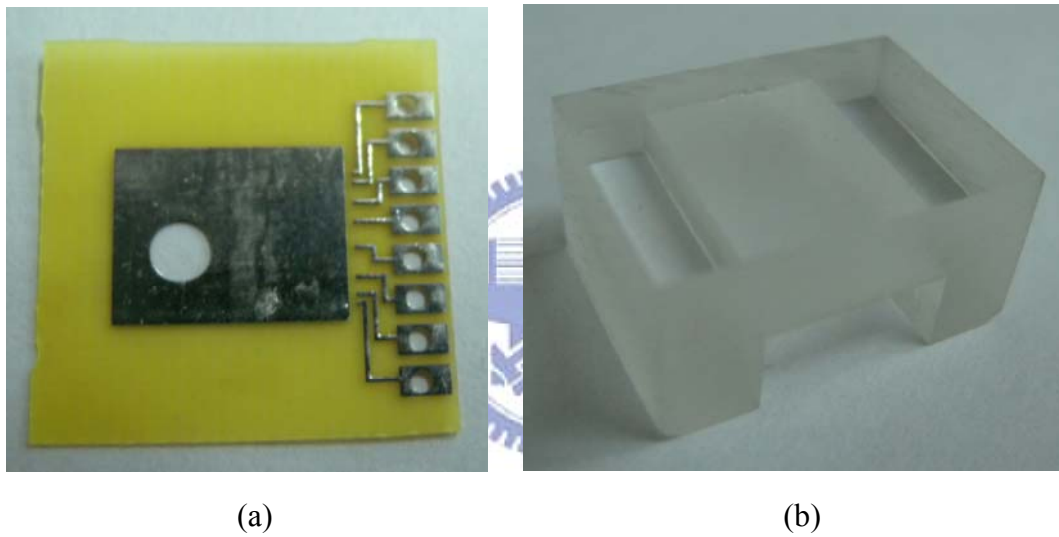


Figure 5-2 Fabricated (a) PCB, (b) holder.

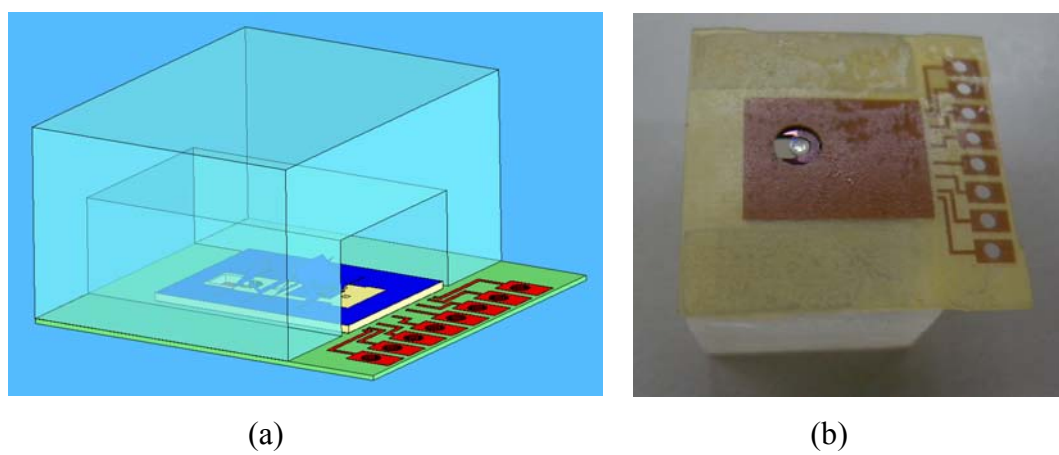


Figure 5-3 (a) Schematic of assembled optical pickup unit, (b) test experiment showing PCB, holder and objective lens.

Another test experiment was conducted to bond the laser diode on the released sample and then assemble the micromirrors by the simple push operation. Figure 5-4 shows the bonding process of the test experiment. Figure 5-4 (a) shows the 90° devices after release. Figure 5-4 (b) shows the overlaid image of the laser diode in the flip-chip bonder. And we applied thermal cure adhesive on the position of the laser diode, as shown in Figure 5-4 (c). Then we bonded the laser diode by controlling the arm of flip-chip bonder and heating the thermal cure adhesive, as shown in Figure 5-4 (d). Finally, we assembled the 90° micromirror by one-push operation and test the laser diode, as shown in Figure 5-4 (e) and (f).

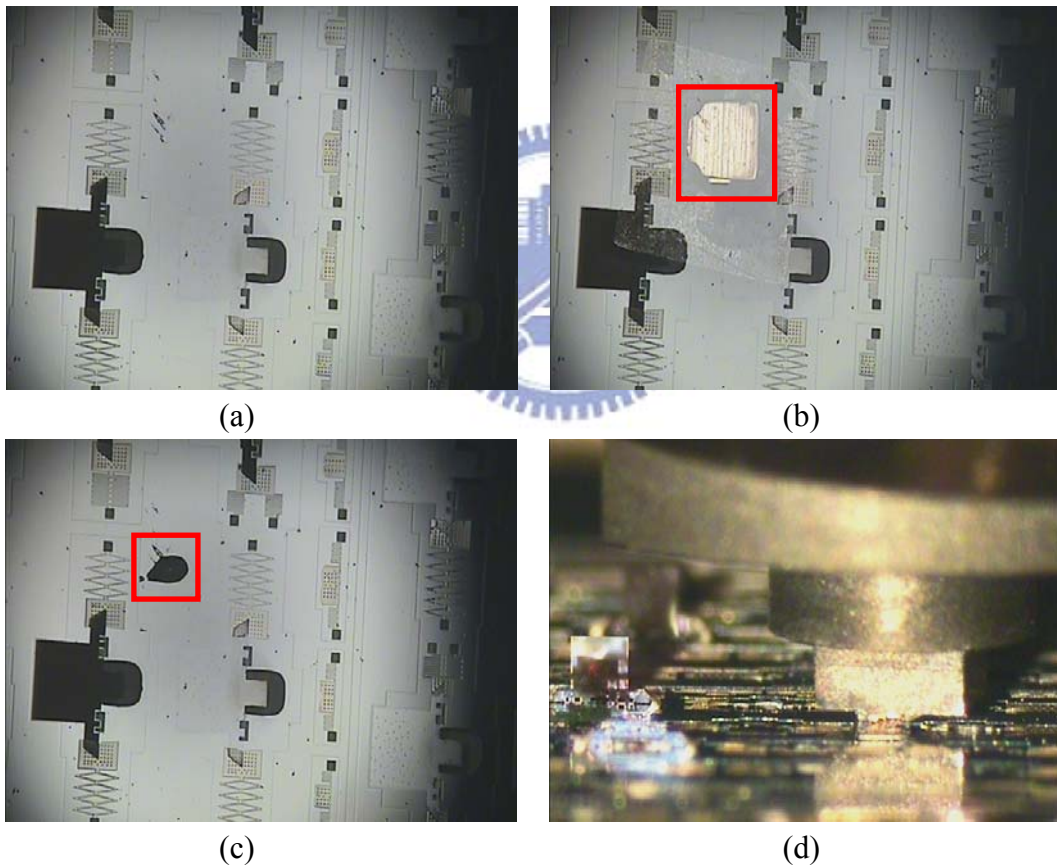
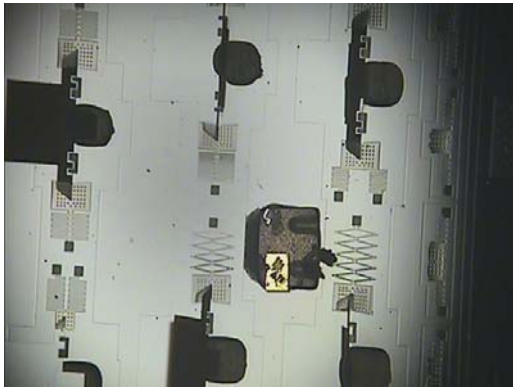
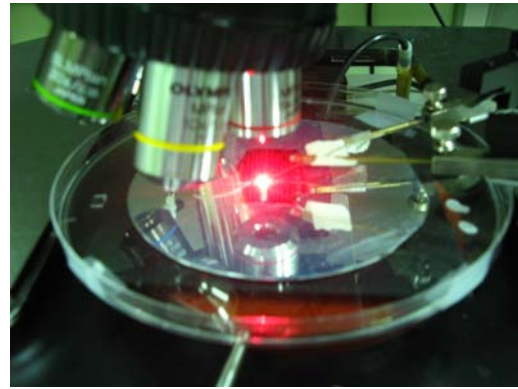


Figure 5-4 Bonding process of laser diode, (a) a release sample and a mirror plate before assembly, (b) overlaid image of the laser diode, (c) apply thermal cure adhesive on the laser diode position, (d) bond the laser diode by controlling the arm of flip-chip bonder.



(e)



(f)

Figure 5-4 Bonding process of laser diode (continued), (e) assemble the 90° micromirror by one-push operation, (f) test the laser diode.



Reference

- [1] L. Y. Lin, J. L. Shen, S. S. Lee, and M. C. Wu, "Realization of novel monolithic free-space optical disk pickup heads by surface micromachining," *Optics Letters*, vol. 21, no. 2, pp. 155-157, 1996.
- [2] S. Ura, T. Suhara, H. Nishihara, J. Koyama, and J. Koyama, "An integrated-optic disk pickup device," *Journal of Lightwave Technology*, vol. 4, no. 7, pp. 913-918, 1986.
- [3] T. Shiono and H. Ogawa, "Planar-optic-disk Pickup with diffractive micro-optics," *Applied Optics*, vol. 33, no. 31, pp. 7350-7355, 1994.
- [4] J. Y. Chang, C. M. Wang, C. C. Lee, H. F. Shih, M. L. Wu, "Realization of free-space optical pickup head with stacked Si-based phase elements," *IEEE Photonics Technology Letters*, vol. 17, no. 1, pp. 214-216, 2005.
- [5] J. S. Sohn, E. H. Cho, M. Lee, H. S. Kim, S. D. Suh, S. M. Kang, N. C. Park, and Y. Park, "Development of integrated optical pickup for small form factor optical disk drive," *Optical Data Storage Topical Meeting*, pp. 18-20, 2006.
- [6] J. M. Bustillo, R. T. Howe, and R. S. Muller, "Surface micromachining for microelectromechanical systems," *Proceedings of the IEEE*, vol. 86, no. 8, pp. 1552-1574, 1998.
- [7] K. S. J. Pister, M. W. Judy, S. R. Burgett, and R. S. Fearing, "Microfabricated hinges," *Sensors and Actuators A: Physical*, vol. 33, no. 3, pp. 249-256, 1992.
- [8] T. Akiyama and K. Shono, "Controlled stepwise motion in polysilicon microstructures," *Journal of Microelectromechanical Systems*, vol. 2, no. 3, pp. 106-110, 1993.

- [9] L. Y. Lin, E. L. Goldstein, and R. W. Tkach, "On the expandability of free-space micromachined optical cross connects," *Journal of Lightwave Technology*, vol. 18, no. 4, pp. 482-489, 2000.
- [10] J. R. Reid, V. M. Bright and J. T. Butler, "Automated assembly of flip-up micromirrors," *Sensors and Actuators A: Physical*, vol. 66, no. 1, pp. 292-8, 1998.
- [11] Y. W. Yi and C. Liu, "Magnetic actuation of hinged microstructures," *Journal of Microelectromechanical Systems*, vol. 8, no. 1, pp. 10-17, 1999.
- [12] E. Iwase and I. Shimoyama, "A design method for out-of-plane structures by multi-step magnetic self-assembly," *Sensors and Actuators A: Physical*, vol. 127, no. 2, pp. 310-315, 2006.
- [13] A. P. Hui, and W. J. Li, "Non-contact batch micro-assembly by centrifugal force," *The Fifteenth IEEE International Conference of Microelectromechanical Systems*, pp. 184-187, 2002.
- [14] V. Kaajakari and A. Lal, "Thermokinetic actuation for batch assembly of microscale hinged structures," *Journal of Microelectromechanical Systems*, vol. 12, no. 4, pp. 425-32, 2003.
- [15] R. W. Johnstone, D. Sameoto and M. Parameswaran, "Non-uniform residual stresses for parallel assembly of out-of-plane surface-micromachined structures," *Journal of Micromechanics and Microengineering*, vol. 16, no. 11, N17-22, 2006.
- [16] R. R. A. Syms, C. Gormley and S. Blackstone, "Improving yield, accuracy and complexity in surface tension self-assembled MOEMS," *Sensors and Actuators A: Physical*, vol. 88, no. 3, pp. 273-283, 2001.
- [17] K. Harsh and Y. C. Lee, "Modeling for solder self-assembled MEMS," *Proceedings of the SPIE*, vol. 3289, pp. 177-184, 1998.

- [18] N. Dechev, W. L. Cleghorn, and J. K. Mills, "Microassembly of 3-D microstructures using a compliant, passive microgripper," *Journal of Microelectromechanical Systems*, vol. 13, no. 2, pp. 176-189, 2004.
- [19] K. Tsui, A. A. Geisberger, M. Ellis and G. H. Skidmore, "Micromachined end-effector and techniques for directed MEMS assembly," *Journal of Micromechanics and Microengineering*, vol. 14, no. 4, pp. 542-9, 2004.
- [20] S. H. Tsang, D. Sameoto, I. G. Foulds, R. W. Johnstone, and M. Parameswaran, "Automated assembly of hingeless 90° out-of-plane microstructures," *Journal of Micromechanics and Microengineering*, vol. 17, no. 7, pp. 1314-1325, 2007.
- [21] Y. Chiu, C. S. Wu, W. Z. Huang, and J. W. Wu, "Assembly of micro-3-D components on SOI wafers using novel SU-8 locking mechanisms and vertical one-push operation," *IEEE Journal of Selected Topics in Quantum Electronics*, vol. 15, no. 5, pp. 1338-1343, 2009.
- [22] C. S. Wu, "Assembly of Three Dimensional Microstructures with Multiple Angles by One-Push Method on SOI Wafers," Master Thesis, Department of Electrical and Computer Engineering, National Chiao Tung University, Taiwan, 2008.
- [23] R. Raymond and J. Raymond, "Torsion", in *Roark's formulas for stress and strain*, 6th edition: McGraw-Hill, 1989.
- [24] J. J. Wortman and R. A. Evans, "Young's Modulus, Shear Modulus, and Poisson's Ratio in Silicon and Germanium," *Journal of Applied Physics*, vol. 36, no. 1, pp. 153-156, 1965.
- [25] S. H. Tsang and M. Parameswaran, "Self-locking vertical operation single crystal silicon micromirrors using silicon-on-insulator technology," in *Canadian Conference on Electrical and Computer Engineering*, pp. 429-432,

2005.

- [26] H. F. Shih, C. L. Chang, K. J. Lee, and C. S. Chang, "Design of optical head with holographic optical element for small form factor drive systems," *IEEE Transactions on Magnetics*, vol. 41, no. 2, pp. 1058-1060, 2005.
- [27] J. W. Goodman, "Introduction to Fourier Optics," rev. 3, Roberts & Co., 2005.
- [28] C. S. Lu, "Small-Form-Factor Optical Pickup Head Design Using Prism-Type Holographic Optical Element," Master Thesis, Department of Mechanical Engineering, National Chung Hsing University, Taiwan, 2009.
- [29] Y. Fukuta, H. Fujita, and H. Toshiyoshi, "Vapor hydrofluoric acid sacrificial release technique for micro electro mechanical systems using labware," *Japanese Journal of Applied Physics*, vol. 42, pp. 3690–3694, 2003.
- [30] N. Belov and N. Khe, "Using deep RIE for micromachining SOI wafers," *Proceedings Electronic Components and Technology Conference 2002. IEEE*, pp. 1163-1166, 2002.

